# Numerical modeling of multiscale wave propagation phenomena in fluid–rock systems

Marcel Frehner

2009
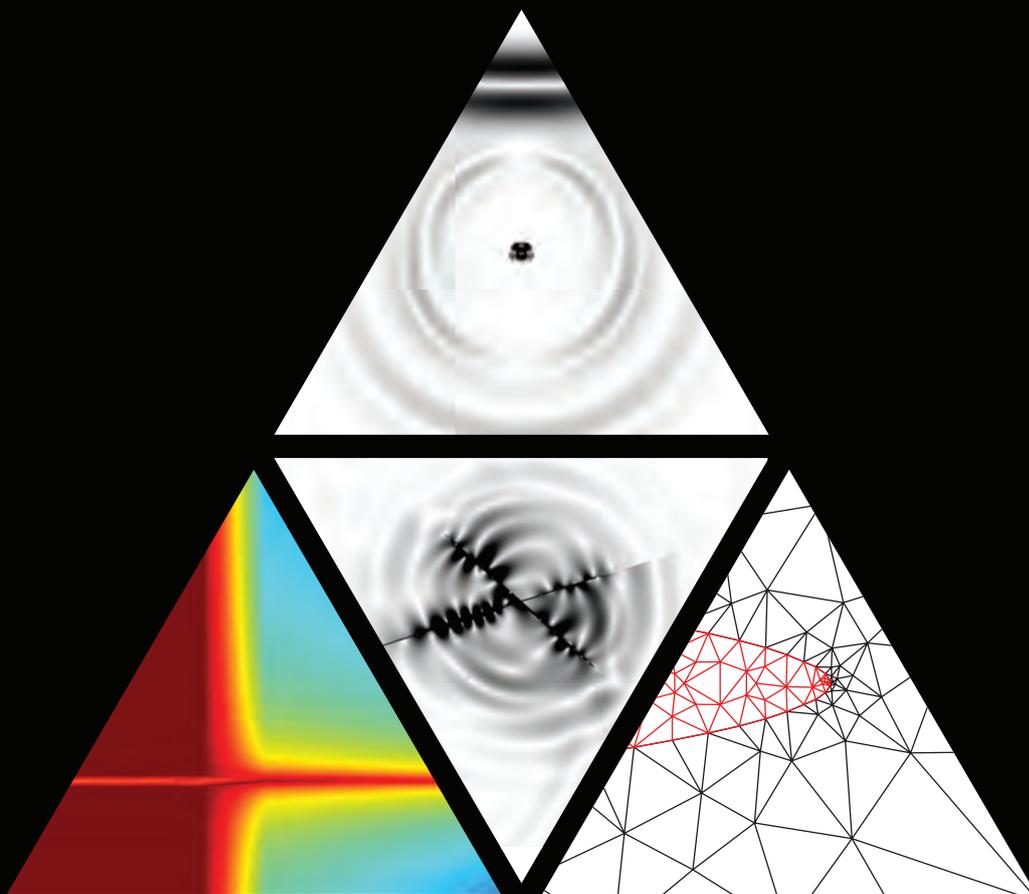
Numerical modeling of multiscale wave propagation phenomena in fluid−rock systems

A dissertation submitted to

ETH Zurich

for the degree of
Doctor of Sciences

presented by

Marcel Frehner

Dipl. Natw. ETH Zurich

born 30.11.1979

citizen of
Urnäsch (AR)

Accepted on the recommendation of

Prof. Dr. Jean–Pierre Burg	ETH Zurich	Examiner
PD Dr. Stefan M. Schmalholz	ETH Zurich	Co-examiner
Dr. ir. David M. J. Smeulders	Delft University of Technology	Co-examiner
Prof. Dr.-Ing. Holger Steeb	Ruhr-University Bochum	Co-examiner

2009

I know we are going down a road that we may not know where we end,
but that is exactly what science is all about.

Dream Theater – The Great Debate

Table of Contents

Summary

Many seismic surveys are carried out in areas with porous or fractured rocks containing fluids, e.g. volcanic areas or hydrocarbon reservoirs. Therefore, the effects of fluids in porous or fractured rocks on the propagation of seismic waves are important to understand. In this thesis three such phenomena are investigated numerically, namely

- scattering at heterogeneities,
- Stoneley guided waves reflected and scattered at crack tips and
- oscillations on the pore–level due to surface tension effects.

The presented phenomena exhibit a multiscale character because seismic wavelengths can be orders of magnitude different from the objects that cause the phenomena, i.e. pores or cracks. Numerical modeling of such multiscale problems can be approached in different ways. On one hand, effective medium and mixture models can be used that approximate the small scale processes with effective material parameters and incorporate them into larger scale wave propagation models. On the other hand, direct numerical simulations can be used that fully resolve the small scale processes. Both approaches are followed in this thesis.

- Scattering of a plane P–wave at a circular object of a similar size as the P–wave's wavelength is modeled in two dimensions with different numerical techniques. The circular object is numerically fully resolved and the results are compared with an analytical solution. The goal is to compare numerical accuracies of the different methods for later use in direct numerical simulations. It is found that the finite element method is most suitable for spatial discretization of such problems due to the unstructured numerical mesh.
- The reflection of Stoneley guided waves at the tip of a crack is investigated with direct numerical simulations in two dimensions using the finite element method. The reflection coefficient lies between 43 % and almost 100 % and depends on the fluid filling the crack and on the crack geometry. The part of the Stoneley guided wave that is not reflected is scattered at the crack tip and P– and S–waves are

emitted into the surrounding rock. The radiation pattern of these elastic body waves is described in detail for different model setups.

- Microscale oscillations within a rock can arise from non–wetting fluid blobs in partially saturated pores and cracks. When such fluid blobs are out of equilibrium, surface tension forces act as the restoring forces for the oscillations. Other explanations for internal oscillations in a rock can be given, e.g. Stoneley guided waves propagating back and forth along a finite crack. Such microscale oscillations are approximated and coupled to the macroscale wave equation. The resulting equations are solved in one dimension with the finite difference method. Results show that internal oscillations introduce a strong velocity dispersion around the resonance frequency and temporarily modify the frequency content of a propagating wave. Energy is transferred between the internal oscillations and the wave.

This thesis covers a few aspects of fluid–rock interaction relevant for seismic wave propagation. For this, no existing models, such as the Biot model, are applied but direct numerical simulations and a newly developed continuum model are used. The thesis ends by discussing the applicability of the results to natural situations. Tremor–signals are observed for example around volcanic conduits or above hydcrocarbon reservoirs. The narrow frequency band of these signals may be explained, among other explanations, by oscillatory effects in the subsurface due to Stoneley guided waves that fall into resonance or due to surface tension–induced resonances of non–wetting fluids.

Zusammenfassung

Seismische Untersuchungen werden oft in Gebieten mit porösen oder zerklüfteten Gesteinen, die Fluide enthalten, durchgeführt, wie zum Beispiel in vulkanischen Gebieten oder über Kohlenwasserstofflagerstätten. Deshalb ist es wichtig die Effekte dieser Fluide auf die seismische Wellenausbreitung zu verstehen. Drei solche Phänomene werden in der vorliegenden Dissertation numerisch untersucht, nämlich

- die Streuung an Heterogenitäten,
- die Reflexion und Steuung von geleiteten Stoneley–Wellen (Englisch: *Stoneley guided Waves*) an der Spitze von Klüften und
- durch Oberflächenspannungs–Effekte hervorgerufene Oszillationen im Porenraum.

All diese Phänomene umfassen mehrere Grössenordnungen. Übliche seismische Wellenlängen sind in der Regel um Grössenordnungen unterschiedlich im Vergleich zu den Objekten, die diese Phänomene hervorrufen, wie zum Beispiel Poren oder Klüfte im Gestein. Für die numerische Modellierung solcher Phänomene stehen verschiedene Ansätze zur Auswahl. Einerseits gibt es Effektiv–Medium– und Mischungs–Modelle, welche die kleinräumigen Prozesse mit effektiven Materialparametern vereinfachen und in grossräumige Wellenausbreitungs–Modelle einbinden. Andererseits können direkte numerische Simulationen verwendet werden, welche die kleinräumigen Prozesse detailiert auflösen. In der vorliegenden Dissertation werden beide Ansätze verwendet.

- Die Streuung einer ebenen P–Welle an einem runden Objekt wird mit verschiedenen numerischen Methoden in zwei Dimensionen modelliert. Dabei hat das runde Objekt eine vergleichbare Grösse wie die Wellenlänge der P–Welle und das numerische Gitter löst das Objekt vollständig auf. Das Ziel dieser Studie ist ein Vergleich der numerischen Genauigkeiten der verschiedenen Methoden für spätere direkte numerische Simulationen. Zum Vergleich wird eine exakte analytische Lösung heran gezogen. Es stellt sich heraus, dass für die räumliche Auflösung dieser Art von Problemstellungen die Finite Elemente Methode am geeignetsten ist, da sie ein unstrukturiertes numerisches Gitter verwendet.

- Die Reflexion von geleiteten Stoneley–Wellen an der Spitze von Klüften wird mit direkten numerischen Simulationen unter Verwendung der Finite Elemente Methode in zwei Dimensionen untersucht. Der Reflexionskoeffizient liegt zwischen 43 % und nahezu 100 %. Dieser Wert hängt vom Fluid in der Kluft und von der Geometrie der Kluft ab. Ein Teil der geleiteten Stoneley–Welle wird jedoch nicht reflektiert sondern an der Spitze der Kluft gestreut. Die Abstrahlcharakteristik der dabei ins imliegende Gestein ausgestrahlten P– und S–Wellen wird für verschiedene Modellkonfigurationen im Detail beschrieben.

- Oszillationen im Porenraum können durch nichtnetzende Flüssigkeiten in teilgesättigten Poren oder Klüften hervorgerufen werden. Beim Auslenken solcher Flüssigkeiten aus dem Gleichgewicht, wirkt die Oberflächenspannungskraft als die rücktreibende Kraft. Es sind auch andere Ursachen für Gesteins–interne Oszillationen denkbar, wie zum Beispiel eine geleitete Stoneley–Welle, die entlang einer Kluft hin und her läuft. Eine vereinfachte Formulierung solcher kleinräumiger Oszillationen werden mit der grössräumigen Wellengleichung gekoppelt. Die resultierenden Gleichungen werden mit der Finite Differenzen Methode im eindimensionalen Raum gelöst. Die Simulationen zeigen, dass die Gesteins–internen Oszillationen den Frequenzgehalt von seismischen Wellen vorübergehend verändern können. Ebenfalls rufen die Oscillationen eine starke Geschwindigkeitsdispersion um die Resonanzfrequenz hervor. Es findet ein Energieaustausch zwischen den Gesteins–internen Oszillationen und den sich ausbreitenden Wellen statt.

Die vorliegende Dissertation behandelt einige Aspekte der Interaktion zwischen Fluiden und Gesteinen, welche für die Ausbreitung von seismischen Wellen relevant sind. Dabei kommen keine existierenden Modelle (wie z.B. die Biot Theorie) zur Anwendung. Viel mehr werden direkte numerische Simulationen und ein neu entwickeltes Kontinuum–Modell verwendet. Zum Schluss der Dissertation folgt eine Diskussion über die Anwendbarkeit der Resultate auf natürliche Situationen. Zum Beispiel werden in vulkanischen Gegenden und über Kohlenwasserstofflagerstätten oft Tremorsignale beobachtet. Das enge Frequenzband dieser Signale könnte unter anderem mit Oszillations–Effekten im Erdinneren erklärt werden, wie zum Beispiel geleitete Stoneley–Wellen, die in Resonanz geraten wenn sie einer Kluft entlang hin und her laufen oder aber Oszillationen im Porenraum aufgrund von Oberflächenspannung, die auf nichtnetzende Flüssigkeiten wirkt.

MAIN PART OF THESIS

1 Introduction

Many near–surface rocks contain fluids in the pore space or in fractures, for example in volcanic areas, below hydrothermal fields or in hydrocarbon reservoirs. Such geological settings are of particular interest because of either commercial potential or natural hazard assessment. Accordingly, seismic surveys are often carried out in areas where rocks contain fluids. Therefore, understanding the effects of fluids on the propagation of seismic waves is of great importance for the interpretation of seismic data. A number of phenomena are known to arise from the presence of fluid–filled cavities in the rock. The phenomena relevant for wave propagation include but are not limited to

- wave–induced fluid flow due to pressure–differences between adjacent pores (Bourbie *et al.*, 1987; Carcione, 2001),
- occurence of a second compressional wave when the fluid and the rock move out of phase (Bourbie *et al.*, 1987; Carcione, 2001),
- Stoneley guided waves propagating along fractures (Ferrazzini and Aki, 1987; Korneev, 2008),
- oscillations due to interfacial tension forces acting on non–wetting fluid blobs trapped in cavities (Hilpert *et al.*, 2000),
- scattering of body waves at cavities (Sanchez-Sesma and Iturraran-Viveros, 2001; Krüger *et al.*, 2005) and
- attenuation of body waves due to viscous damping (Bourbie *et al.*, 1987; Carcione, 2001).

Depending on the frequencies used in a seismic survey and on the size of the cavities under study (from the pore scale to fracture length to the size of magma chambers), wavelengths can be orders of magnitude different from these cavities. In other words, the fluid–rock interaction is a multiscale problem, which makes it difficult to study. When the wavelenths are of the same order as the size of the cavities analytical expressions for some of the listed phenomena can be derived, but only for simple geometries. For example, Korneev (2008) derived analytical expressions for Stoneley guided waves that propagate along an infinitely long crack with constant thickness filled with a viscous fluid

or Liu *et al.* (2000) derived analytical expressions for scattering of waves at a circular heterogeneity. However, for real pore or fracture geometries analytical solutions become too complicated or even impossible to derive.

For wavelengths much larger than the cavities continuum models can be used. They approximate microscale processes with effective parameters and incorporate them into wave propagation models. For example, Korneev *et al.* (2004) added a diffusion–term to the wave equation to model dissipation "bearing in mind that the true physical attenuation mechanisms are still unclear". A more elaborate continuum model is for example the Biot model (Biot, 1962) that uses a Darcy–type term to model fluid flow between adjacent pores. However, common to all continuum models is the averaging of material behavior of the fluid (or multiple fluids) and the rock in a representative volume. This averaging leads to effective material parameters that are then used to approximately describe the microscale process. However, the averaging also lets the interfaces between the fluid (or multiple fluids) and the rock disappear and a number of phenomena related to interfaces are not considered, e.g. microscale scattering at heterogeneities, Stoneley guided waves or interfacial tension between different fluids.

Exactly these phenomena are adressed in this thesis. This is mainly done with numerical simulations using self–developed codes. Two different approaches for investigating fluid–rock interaction are followed:

- Direct numerical simulations resolve the small scale cavities and therefore include phenomena related to interfaces. This approach is choosen for the study of scattering and of Stoneley guided waves. Numerical accuracy is ensured by comparing the numerical results with analytical solutions for simple geometries. Then, more complex geometries are studied, for which no analytical solutions are available and numerical simulations are indispensable.
- A continuum model is newly developed that include microscale oscillations due to interfacial tension acting on non–wetting fluid blobs trapped in cavities. The model is used for analytical studies and for numerical simulations of rocks exhibiting internal oscillations.

Because of the multiscale character of the investigated problems, numerical simulation "presents a major computational challenge (Korneev, 2008)". Therefore, numerical as-

pects are a major aspect of this thesis. For both direct numerical simulations and simulations using an effective continuum model different numerical methods are available (Kelly and Marfurt, 1990; Carcione *et al.*, 2002; Cohen, 2002), for example the finite difference method (Smith, 1985; Moczo *et al.*, 2007) or the finite element method (Bathe, 1996; Zienkiewicz and Taylor, 2000). In the course of this thesis it will be shown that the different numerical methods have advantages and disadvantages depending on the particular problem under study.

1.1. Thesis Organization

Chapters 2 – 4 of this thesis are written as individual papers to be published in peer–reviewed journals. Therefore, they are somewhat independent from each other. Each of these chapters contain the sequence of subchapters commonly used in papers, i.e. introduction, methods, results, discussion and conclusions. References are also given at the end of each chapter. The different chapters are organized in the following way:

Chapter 2 presents a numerical accuracy study. A two–dimensional scatteing problem is solved numerically with different methods and the results are compared with an exact analytical solution. This is done to identify the most suitable method for direct numerical simulations performed later in Chapter 3. The focus lies much more on the numerical aspect than on the physical aspect of scattering. This chapter was published in Physics of the Earth and Planetary Interiors 171 (2008).

Chapter 3 presents a study of Stoneley guided waves that are reflected and scattered at the tip of a crack. Reflection coefficients are evaluated and radiation patterns of the scattered part of the Stoneley guided waves are described in detail. This is done by highly resolving the crack using the finite element method and directly simulate the propagation, reflection and scattering of the Stoneley guided wave. This chapter is submitted to Geophysics.

Chapter 4 presents a one–dimensional continuum model that couples microscale oscillations with the macroscale wave equation. The resulting equations are analyzed analytically and solved numerically using the finite difference method to investigate the effect

of internal oscillations within a rock on the propagation of waves. This chapter was published in Geophysical Journal International 176 (2009).

Chapter 5 is a discussion of the over–all thesis results. It brings together and discusses the interrelation of the results of the individual Chapters 2 – 4. It also discusses possible applications of the results.

Chapter 6 presents the general conclusions of this thesis.

Appendix A explains in detail the governing equations for elastic and visco–acoustic media in two dimensions. These two material behaviors are used in Chapters 2 and 3 for the solid rock and for the fluid filling the circular inclusion (Chapter 2) and the crack (Chapter 3), respectively.

Appendix B explains the finite difference method and the corresponding self–developed numerical code used in Chapter 2 in more detail. The governing equations for elastic media and inviscid fluids (acoustic media) are solved with the finite difference method.

Appendix C explains the finite element method and the corresponding self–developed numerical code used in Chapters 2 and 3 in more detail. The governing equations for elastic media and viscous fluids (visco–acoustic media) are solved with the finite element method.

Appendix D shows the resonant behavior of a circular object when a wave is scattered at the object. This phenomenon is known as resonant scattering and is not explained in Chapter 2 because the focus of Chapter 2 lies on the numerical aspects of the scattering problem.

1.2. Related work

This thesis is a part of a bigger research project, out of which a number of publications emerged. The project was motivated by observations of low–frequency tremor–like signals above hydrocarbon reservoirs, often referred to as hydrocarbon microtremor, reported by Dangel *et al.* (2003), Holzner *et al.* (2005), Bloch and Akrawi (2006), Suntsov *et al.*

(2006), Graf *et al.* (2007) and Walker (2008). The frequency content of the ever–present seismic wavefield seemed to be different above hydrocarbon reservoirs compared to areas withouth hydrocarbons. However, more systematic measurements and data analysis and especially a better understanding of the potential underlying physical mechanisms was necessary.

On the data analysis side, Lambert *et al.* (2008) developed attributes of passive seismic surface measurements. For a survey in Austria some of these attributes correlated with assumed reservoir outlines projected to the surface. However, it remained unclear if this correlation is due to signals from the reservoir or due to other, e.g. surface influences.

Steiner *et al.* (2008) showed the possibility of numerically back–propagating very similar surface measurements into the subsurface. This method was called Time Reverse Modeling (TRM) and the application to a survey in Austria showed some good localizations of reservoir areas in depth.

On the theoretical side, Quintal *et al.* (2009) derived an approximate formula for the minimum value of the quality factor in heterogeneously saturated porous rocks and showed that the reflection coefficient due to attenuation contrast between a reservoir and the surrounding rocks can be strongly frequency dependent.

Holzner *et al.* (2009) presented a numerical study of microscale oscillations of non–wetting fluid blobs due to surface tension. The surface of the fluid blob was tracked numerically and surface tension forces were calculated. It was shown that the motion of the fully resolved fluid blob can be approximated with a linear harmonic oscillator equation.

Finally, Saenger *et al.* (2009) presented an extensive hydrocarbon microtremor survey in Mexico. The survey design, the data processing steps and the data analysis are explained in detail. The final results are presented as maps of the calculated seismic attributes, which correlated quite well with known reservoir outlines projected to the surface.

References

Bathe K.-J., 1996: **Finite element procedures**, 2nd Edition, Prentice Hall, Englewood Cliffs, ISBN 0-1330-1458-4

Biot M. A., 1962: **Mechanics of deformation and acoustic propagation in porous media**, Journal of Applied Physics 33, 1482–1498

Bloch G. and Akrawi K., 2006: **Application of low frequency passive seismic surveys in ADCO, UAE**, in EAGE Workshop Passive Seismic, Dubai, United Arab Emirates

Bourbie T., Coussy O. and Zinszner B., 1987: **Acoustics of porous media**, Editions Technip, Paris, ISBN 2-7108-0516-2

Carcione J. M., 2001: **Wave fields in real media: Wave propagation in anisotropic, anelastic and porous media**, Volume 31 of Handbook of Geophysical Exploration, Elsevier Science Ltd., Amsterdam, ISBN 0-0804-3929-2

Carcione J. M., Herman G. C. and ten Kroode A. P. E., 2002: **Seismic modeling**, Geophysics 67, 1304–1325, doi:10.1190/1.1500393

Cohen G. C., 2002: **Higher-order numerical methods for transient wave equations**, Series in scientific computation, Springer Verlag, Berlin, ISBN 3-5404-1598-X

Dangel S., Schaepman M. E., Stoll E. P., Carniel R., Barzandji O., Rode E. D. and Singer J. M., 2003: **Phenomenology of tremor-like signals observed over hydrocarbon reservoirs**, Journal of Volcanology and Geothermal Research 128, 135–158, doi:10.1016/S0377-0273(03)00251-8

Ferrazzini V. and Aki K., 1987: **Slow waves trapped in a fluid-filled infinite crack: Implication for volcanic tremor**, Journal of Geophysical Research 92, 9215–9223

Frehner M. and Schmalholz S. M., 2009: **Finite element simulations of Stoneley guided wave reflection and scattering at the tips of fluid-filled fractures**, Geophysics Submitted

Frehner M., Schmalholz S. M., Saenger E. H. and Steeb H., 2008: **Comparison of finite difference and finite element methods for simulating two-dimensional scattering of elastic waves**, Physics of the Earth and Planetary Interiors 171, 112–121, doi:10.1016/j.pepi.2008.07.003

Frehner M., Schmalholz S. M. and Podlachikov Y., 2009: **Spectral modification of seismic waves propagating through solids exhibiting a resonance frequency: A 1-D coupled wave propagation-oscillation model**, Geophysical Journal International 176, 589–600, doi:10.1111/j.1365-246X.2008.04001.x

Graf R., Schmalholz S. M., Podladchikov Y. and Saenger E. H., 2007: **Passive low frequency spectral analysis: Exploring a new field in geophysics**, World Oil January, 47–52

Hilpert M., Jirka G. H. and Plate E. J., 2000: **Capillarity-induced resonance of oil blobs in capillary tubes and porous media**, Geophysics 65, 874–883

Holzner R., Eschle P., Zürcher H., Lambert M., Graf R., Dangel S. and Meier P. F., 2005: **Applying microtremor analysis to identify hydrocarbon reservoirs**, First Break 23, 41–46

Holzner R., Eschle P., Dangel S., Frehner M., Narayanan C. and Lakehal D., 2009: **Hydrocarbon microtremors interpreted as nonlinear oscillations driven by oceanic background waves**, Communications in nonlinear science and numerical simulation 14, 160–173, doi:10.1016/j.cnsns.2007.06.013

Kelly K. R. and Marfurt K. J., 1990: **Numerical modeling of seismic wave propagation**, Volume 13 of Geophysics reprint series, Society of Exploration Geophysicists, Tulsa, ISBN 1-5608-0011-9

Korneev V., 2008: **Slow waves in fractures filled with viscous fluid**, Geophysics 73, N1–N7, doi:10.1190/1.2802174

Korneev V. A., Goloshubin G. M., Daley T. M. and Silin D. B., 2004: **Seismic low-frequency effects in monitoring fluid-saturated reservoirs**, Geophysics 69, 522–532, doi:10.1190/1.1707072

Krüger O. S., Saenger E. H. and Shapiro S. A., 2005: **Scattering and diffraction by a single crack: An accuracy analysis of the rotated staggered grid**, Geophysical Journal International 162, 25–31, doi:10.1111/j.1365-246X.2005.02647.x

Lambert M.-A., Schmalholz S. M., Saenger E. H. and Steiner B., 2008: **Low-frequency microtremor anomalies at an oil and gas field in Voitsdorf, Austria**, Geophysical Prospecting In Press, doi:10.1111/j.1365-2478.2008.00734.x

Liu Y. B., Wu R.-S. and Ying C. F., 2000: **Scattering of elastic waves by an elastic or viscoelastic cylinder**, Geophysical Journal International 142, 439–460

Moczo P., Robertsson J. O. A. and Eisner L., 2007: **The finite-difference time-domain method for modeling of seismic wave propagation**, in Advances in Geophysics, Volume 48, Elsevier Academic Press Inc., San Diego, pages 421–516, doi: 10.1016/S0065-2687(06)48008-0

Quintal B., Schmalholz S. M. and Podladchikov Y. Y., 2009: **Low-frequency reflections from a thin layer with high attenuation caused by interlayer flow**, Geophysics 74, N15–N23, doi:10.1190/1.3026620

Saenger E. H., Schmalholz S. M., Lambert M., Nguyen T. T., Torres A., Metzger S., Habiger R., Rentsch S. and Mendez-Hernandez E., 2009: **A passive seismic survey over a gas field: Analysis of low-frequency anomalies**, Geophysics 74, doi: 10.1190/1.3078402

Sanchez-Sesma F. J. and Iturraran-Viveros U., 2001: **Scattering and diffraction of SH waves by a finite crack: An analytical solution**, Geophysical Journal International 145, 749–758

Smith G. D., 1985: **Numerical solutions of partial differential equations: Finite difference methods**, 3rd Edition, Oxford applied mathematics and computing science series, Oxford University Press, Oxford, ISBN 0-1985-9650-2

Steiner B., Saenger E. H. and Schmalholz S. M., 2008: **Time reverse modeling of passive seismic measurements**, Geophysical Research Letters 35, L03307, doi:10.1029/2007GL032097

Suntsov A. E., Aroutunov S. L., Mekhnin A. M. and Meltchouk B. Y., 2006: **Passive infra-frequency microseismic technology - Experience and problems of practical use**, in EAGE Workshop Passive Seismic, Dubai, United Arab Emirates

Walker D., 2008: **Recent developments in low frequency spectral analysis of passive seismic data**, First Break 26, 65–72

Zienkiewicz O. C. and Taylor R. L., 2000: **The finite element method: The Basis**, Volume 1, 5th Edition, Butterworth-Heinemann, Oxford, ISBN 0-7506-5049-4

2 Comparison of finite difference and finite element methods for simulating two–dimensional scattering of elastic waves

Abstract

Two–dimensional scattering of elastic waves in a medium containing a circular heterogeneity is investigated with an analytical solution and numerical wave propagation simulations. Different combinations of finite difference methods (FDM) and finite element methods (FEM) are used to numerically solve the elastodynamic wave equations. Finite difference and finite element techniques are applied to approximate both the time and space derivatives and are combined in various ways to provide different numerical algorithms for modeling elastic wave propagation. The results of the different numerical algorithms are compared for simulations of an incident plane P–wave that is scattered by a mechanically weak circular inclusion whereby the diameter of the inclusion is of the same order than the P–wave's wavelength. For this scattering problem an analytical solution is available and used as the reference solution in the comparison of the different numerical algorithms. Staircase–like spatial discretization of the inclusion's circular shape with the finite difference method using a rectangular grid provides accurate velocity and displacement fields close to the inclusion boundary only for very high spatial resolutions. Implicit time integration based on either finite differences or finite elements does not provide computational advantages compared to explicit schemes. The best numerical algorithm in terms of accuracy and computation time for the investigated scattering problem consists of a finite element method in space using an unstructured mesh combined with an explicit finite difference method in time. The computational advantages and disadvantages of the different numerical algorithms are discussed.

2.1. Introduction

Propagation of seismic waves can be described analytically for some specific geometrical setups (Love, 1944; Achenbach, 1973; Aki and Richards, 2002; Ben-Menahem and Jit Singh, 1981). For more complex geometries, ray–tracing methods (Moser and Pajchel, 1997; Cerveny, 2001) are able to approximate propagation of high–frequency seismic waves when the wavelength is significantly smaller than the characteristic size of heterogeneities. For seismic waves having a significantly larger wavelength than the characteristic size of heterogeneities, effective medium theories can be used (Mavko *et al.*, 2003). However, if the wavelengths of the propagating waves and the characteristic size of heterogeneities are of the same order, numerical methods are essential. Particular numerical challenges are for example scattering phenomena in complex geometries (Korneev and Johnson, 1996), wave attenuation due to wave–induced fluid flow (Carcione *et al.*, 2003; Masson and Pride, 2007), wave propagation in three–phase media (Carcione *et al.*, 2004; Santos *et al.*, 2005) or microscale modeling of wave propagation in poroelastic rocks (Saenger *et al.*, 2007). Although on different scales, all these challenges comprise wave scattering at heterogeneities.

For numerical modeling of seismic wave propagation different methods are available (Kelly and Marfurt, 1990; Carcione *et al.*, 2002; Cohen, 2002), which can have advantages and disadvantages depending on the particular problem under study. Methods used in this paper are the finite difference method (FDM) (Smith, 1985; Ames, 1992; Moczo *et al.*, 2007) and the finite element method (FEM) (Hughes, 1987; Bathe, 1996; Zienkiewicz and Taylor, 2000). Both methods can be used to discretize spatial as well as time derivatives. Different combinations of spatial and temporal discretization methods using FDM and FEM are compared in this study. The different algorithms are described and applied to a two–dimensional (2D) elastic scattering problem for comparison. Analytical solutions for scattered wave fields are available for different cases (Ying and Truell, 1956; White, 1958; Liu *et al.*, 2000; Sanchez-Sesma and Iturraran-Viveros, 2001). Liu *et al.* (2000) provide an analytical solution to the particular 2D scattering problem considered in this study. It is used as the reference solution for the comparison of the numerical results.

The main aim of this study is to compare results of numerical wave propagation simulations based on different numerical algorithms and to discuss accuracy and computational

performance of the different algorithms for a particular scattering problem. The investigated 2D scattering problem consists of a mechanically weak circular inclusion embedded in a stiffer elastic medium whereby a plane P–wave is scattered by the inclusion having a diameter similar to the P–wave's wavelength.
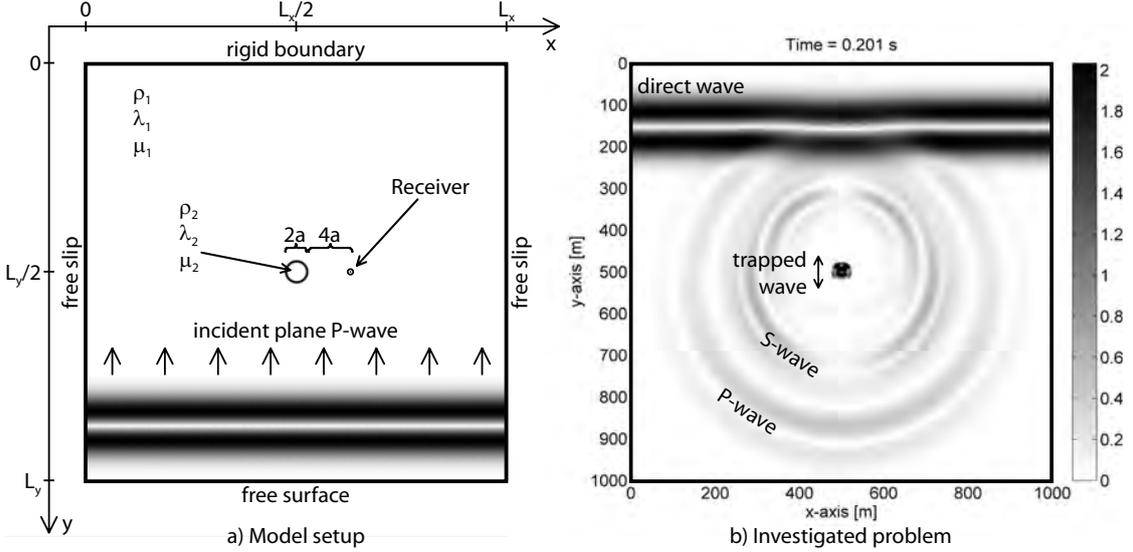
Figure 2.1: Two representative snapshots of the wavefield to illustrate the numerical setup. The particular method used to generate this figure is the spatial FEM with the implicit FDM in time. Plotted is the normalized absolute value of the displacement field $10^{12}\sqrt{u_x^2 + u_y^2}$. a) Early snapshot of the simulation to show the model setup used for all simulations. A plane P–wave travels from bottom to top of the model. Values for indicated physical parameters are given in Table 2.1. Black dot to the right of the inclusion is a synthetic receiver used for further analysis and has a distance to the center of the inclusion of five times the radius a. b) Snapshot after 0.201 s to show the wavefield under study. Values higher than 2 (maximal amplitude of incident wave) are reduced to 2 and colored in black. Amplitudes inside circular inclusion are higher than the gray scale indicates.

2.2. Model Setup

Figure 2.1a) displays a snapshot of a numerical wave propagation simulation showing the 2D model used in this study. The model consists of a mechanically weak circular inclusion with radius $a = 25$ m embedded in a homogeneous elastic medium. A synthetic receiver placed outside the inclusion records the particle displacement in both x– and y–directions.

Boundary conditions are free surface at $y = L_y$ (all stresses $\boldsymbol{\sigma} = 0$), rigid boundary at $y = 0$ (all displacements $\mathbf{u} = 0$) and free slip at $x = 0$ and $x = L_x$ (displacement in x–direction $u_x = 0$ and shear stress $\sigma_{xy} = 0$). All physical parameters are given in Table 2.1. The surrounding material represents an average sedimentary rock with the two Lamé constants λ_1 and μ_1 equal to each other. The inclusion represents a hole filled with gas that is approximated with a shear modulus $\mu_2 = 0$ and Lamé constant λ_2 1000 times smaller compared to the surrounding rock.

Instead of applying an external force (i.e. force term in the elastodynamic wave equation) an initial perturbation in the particle velocity field in y–direction is prescribed at $y = L_y$. The resulting plane P–wave is a Ricker wavelet with a dominant wavelength of λ_{dom} = 157.1 m (dominant frequency f_{dom} = 26.8 Hz). Figure 2.1b) shows a snapshot of the resulting plane P–wave travelling from the bottom of the model towards the top, and being scattered at the inclusion. Clearly visible is the direct plane P–wave that stays relatively undisturbed behind the heterogeneity, and the primary scattered P–wave and S–wave (P–to–S–converted) that are emitted in all directions from the circular inclusion. In addition, a part of the wave is trapped inside the inclusion.

Parameter	Value
Model size in x–direction	$L_x = 1000$ m
Model size in y–direction	$L_y = 1000$ m
Radius of inclusion	$a = 25$ m
Density of surrounding media	$\rho_1 = 2700$ kg/m^3
Density of inclusion	$\rho_2 = \rho_1/100$
Lamé constant λ of surrounding media	$\lambda_1 = 16$ GPa
Lamé constant λ of inclusion	$\lambda_2 = \lambda_1/1000$
Lamé constant μ of surrounding media	$\mu_1 = 16$ GPa
Lamé constant μ of inclusion	$\mu_2 = 0$ Pa
P–wave velocity of surrounding medium	$V_{P1} = 4216$ m/s
P–wave velocity of inclusion	$V_{P2} = 770$ m/s
S–wave velocity of surrounding medium	$V_{S1} = 2434$ m/s
S–wave velocity of inclusion	$V_{S2} = 0$ m/s

Table 2.1: Geometrical and physical properties used for the scattering modeling

2.3. Methods

All numerical methods applied here discretize the linear elastodynamic wave equations in 2D (Love, 1944; Lindsay, 1960; Achenbach, 1973) given by

$$\left\{ \begin{array}{l} \rho\dfrac{\partial^2 u_x}{\partial t^2} \\[2mm] \rho\dfrac{\partial^2 u_y}{\partial t^2} \end{array} \right\} = \left\{ \begin{array}{l} \dfrac{\partial}{\partial x}\left((\lambda + 2\mu)\dfrac{\partial u_x}{\partial x} + \lambda\dfrac{\partial u_y}{\partial y} \right) + \dfrac{\partial}{\partial y}\left(\mu\left(\dfrac{\partial u_x}{\partial y} + \dfrac{\partial u_y}{\partial x} \right) \right) \\[3mm] \dfrac{\partial}{\partial y}\left(\lambda\dfrac{\partial u_x}{\partial x} + (\lambda + 2\mu)\dfrac{\partial u_y}{\partial y} \right) + \dfrac{\partial}{\partial x}\left(\mu\left(\dfrac{\partial u_x}{\partial y} + \dfrac{\partial u_y}{\partial x} \right) \right) \end{array} \right\}. \qquad (2.1)$$

Variable ρ is density, t is time, x and y are the spatial coordinates and λ and μ are the two Lamé constants, where μ is commonly referred to as the shear modulus. The applied numerical algorithms are based on the FDM and the FEM but use different combinations of the two methods for discretizing space and time derivatives. Three basically different algorithms are applied:

1. Explicit FDM in time, FDM in space.
2. Explicit or implicit FDM in time, FEM in space.
3. FEM in time, FEM in space.

2.3.1. Explicit FDM in time and FDM in space

For the FDM in space Eqation 2.1 is split into five first–order differential equations using the velocity–stress formulation. The numerical method commonly used to model wave propagation is the FDM on a staggered grid (Virieux, 1986) using the explicit FDM for time discretization. For this method the two components of the 2D velocity field are defined at different discrete positions within the grid. Components of the stress tensor are also defined at different positions. This implies that both density and shear modulus have to be defined at more than one position in an elementary cell (Virieux, 1986). For modeling high material contrasts special averaging methods of these parameters (Moczo *et al.*, 2002) are necessary to avoid numerical stability problems. Saenger *et al.* (2000) proposed a modified staggered grid method, i.e. the rotated staggered grid (RSG), for which all components of one physical property are defined at the same position in the

grid. No averaging of elastic moduli is necessary. Bohlen and Saenger (2006) presented a stability and accuracy study and demonstrated that the RSG method is more accurate compared to the standard staggered grid method.

The FDM used in this paper is equivalent to the RSG–FDM. Figure 2.2 shows the elementary cell of the grid. Crosses indicate positions where spatial derivatives of the five unknowns (v_x, v_y, σ_{xx}, σ_{yy} and σ_{xy}) are calculated. The spatial derivatives are averaged to nodal points (for spatial derivatives of stress components) or to center points (for spatial derivatives of velocity components), respectively, to multiply them with the appropriate material parameter.
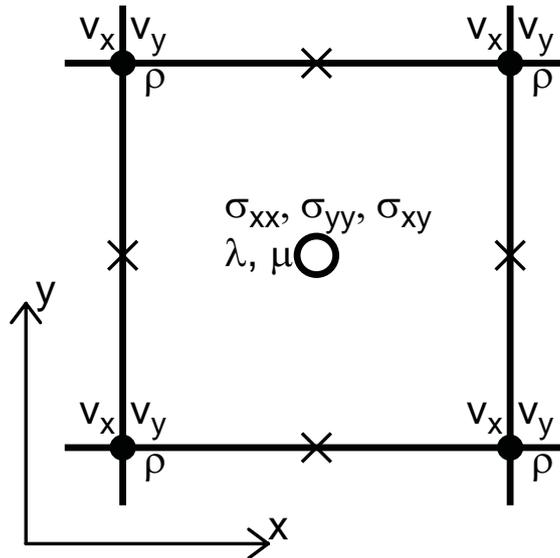
Figure 2.2: Elementary cell for the applied staggered grid FDM. All components of one physical property are defined at the same position in the elementary cell. Spatial derivatives of all unknowns are defined at positions marked with a cross and have to be arithmetically averaged to nodal or center points.

Figure 2.3 sketches the discretization of properties in an inhomogeneous medium. Each elementary cell belongs to one of the two media. In other words, the boundary between different media is discretized along boundaries between elementary cells. According to Krüger *et al.* (2005), elastic moduli are defined at the center of each elementary cell and can only have the value of either of the two media. Therefore, no averaging of elastic moduli is necessary. Density is defined at nodal points of the grid and has to

be arithmetically averaged at nodal points where the four surrounding elementary cells do not belong to the same medium (Krüger *et al.*, 2005). This spatial discretization method is not restricted to equally spaced grids but allows changes in spatial resolution, e.g. higher resolution towards the inclusion. However, the grid is always rectangular, which leads to a staircase–like discretization of the circular inclusion. First–order time derivatives are discretized using the explicit FDM together with a staggered method in time. The von Neumann stability criterion (Higham, 1996; Saenger *et al.*, 2000) is used to define the maximum time increment for stable solutions.
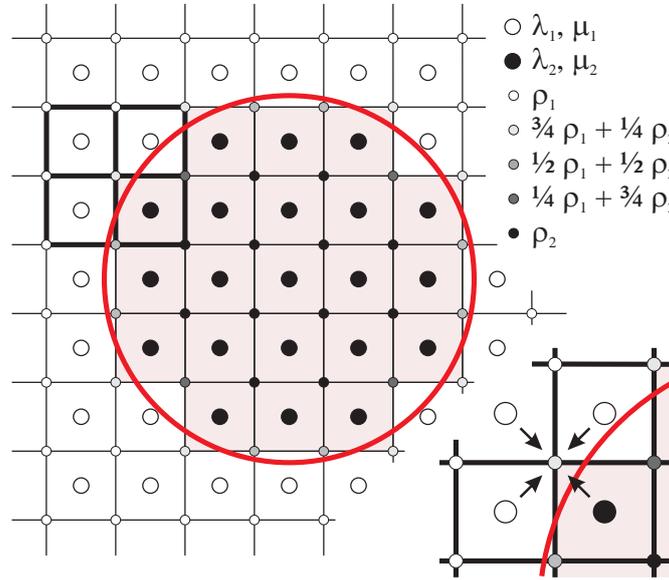
Figure 2.3: Sketch of discretization of material properties with the applied staggered grid FDM. Big red circle is the inclusion with different material properties than the surrounding medium. Red shaded area represents the numerical discretization of the same inclusion. Discretization runs along boundaries between elementary cells. Elastic moduli are defined on big dots (center points) and density is defined on small dots (nodal points). Four elementary cells are blown up to illustrate the arithmetic averaging of the density.

2.3.2. Implicit and explicit FDM in time and FEM in space

The FEM for spatial discretization used in this study (Hughes, 1987; Bathe, 1996; Zienkiewicz and Taylor, 2000) employs 7–node isoparametric triangular elements with biquadratic continuous interpolation functions (Zienkiewicz and Taylor, 2000). Numer-

ical grids are generated by the software Triangle (Shewchuk, 1996, 2002) that produces Delaunay–type meshes. Figure 2.4 sketches the spatial discretization of the circular inclusion with an unstructured triangular grid. Such grids allow strong spatial resolution changes over relatively short distances, e.g. higher resolution close to the inclusion boundary. Numerical implementation comprises the Galerkin weighted residual method (Zienkiewicz and Taylor, 2000), lumped mass matrix (Bathe, 1996; Cohen, 2002) and Gauss–Legendre quadrature with seven integration points (Zienkiewicz and Taylor, 2000). Compared to the FDM described above, material properties are defined for each element and not on individual nodal points. Therefore, no interpolation and averaging of these properties is necessary because the numerical mesh is generated in such a way that boundaries between different media coincide with element boundaries.
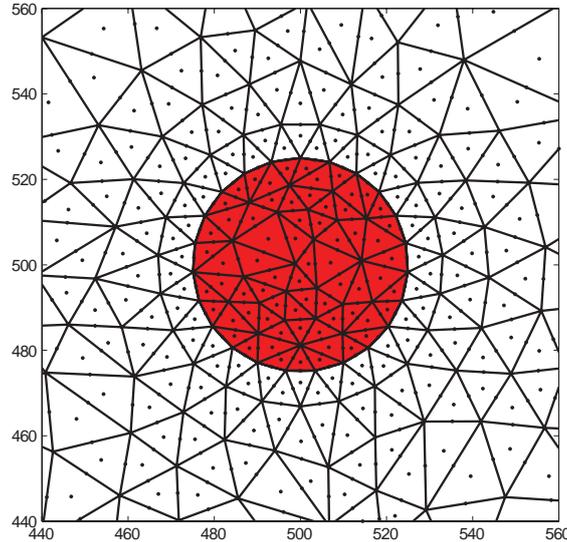
Figure 2.4: Sketch of discretization of inhomogeneity using an unstructured triangular FEM–mesh. Each triangle consists of seven nodal points on which the displacement is calculated. Spatial resolution can increase towards the inclusion boundary that leads to a very accurate discretization of the boundary without the need of a high resolution away from the boundary.

Different methods are available to discretize the second–order time derivative in Equation 2.1, both explicit and implicit, e.g. the leapfrog–method (Bathe, 1996), the Wilson cycle (Zienkiewicz and Taylor, 2000) or the Newmark–algorithm (Newmark, 1959; Hughes, 1987). In this study a variation of the implicit Newmark algorithm is applied (Zienkiewicz and Taylor, 2000). It uses a predictor–corrector scheme and calculates the displacement

20

field $\mathbf{u}$ as the primary unknown, unlike the classical Newmark–algorithm that calculates
the acceleration $\mathbf{a}$ as the first unknown.

- Predictor:

$$
\begin{aligned}
\mathbf{a}_{i+1}^{\text{prediction}} &= -\frac{1}{\beta \Delta t^2}\mathbf{u}_i - \frac{1}{\beta \Delta t}\mathbf{v}_i - \frac{1-2\beta}{2\beta}\mathbf{a}_i \\
\mathbf{v}_{i+1}^{\text{prediction}} &= -\frac{\gamma}{\beta \Delta t}\mathbf{u}_i + \left(1-\frac{\gamma}{\beta}\right)\mathbf{v}_i + \left(1-\frac{\gamma}{2\beta}\right)\Delta t \mathbf{a}_i
\end{aligned}
\tag{2.2}
$$

- Solution:

$$
\mathbf{u}_{i+1} = -\left(\frac{1}{\beta \Delta t^2}\mathbf{M} + \mathbf{K}\right)^{-1}\left(\mathbf{M}\mathbf{a}_{i+1}^{\text{prediction}}\right)
\tag{2.3}
$$

- Corrector:

$$
\begin{aligned}
\mathbf{a}_{i+1} &= \mathbf{a}_{i+1}^{\text{prediction}} + \frac{1}{\beta \Delta t^2}\mathbf{u}_{i+1} \\
\mathbf{v}_{i+1} &= \mathbf{v}_{i+1}^{\text{prediction}} + \frac{\gamma}{\beta \Delta t}\mathbf{u}_{i+1}
\end{aligned}
\tag{2.4}
$$

In Equations 2.2 – 2.4 i is the index of any discrete time interval, Δt is the time increment, $\mathbf{u}$, $\mathbf{v}$ and $\mathbf{a}$ are the two–dimensional displacement, velocity and acceleration fields, respectively, $\mathbf{M}$ is the lumped mass matrix and $\mathbf{K}$ is the stiffness matrix. For β and γ the optimal values of $1/4$ and $1/2$ are chosen (Newmark, 1959; Bathe, 1996). For explicit time integration the classical Newmark algorithm (Newmark, 1959; Hughes, 1987) is used. It is also a predictor–corrector method but calculates the acceleration field $\mathbf{a}$ as the first unknown. To make this algorithm explicit β is set to zero.

2.3.3. FEM in both time and space

Applying the FEM in the temporal domain can be traced back to the seminal work of Argyris and Scharpf (1969) and of Fried (1969). Here, a time–discontinuous Galerkin method (DGT) is applied (Chen *et al.*, 2006). The DGT method is based on classical C_0–continuous interpolation and test functions in the spatial domain, and discontinuous interpolation and test functions in the temporal domain, respectively (Figure 2.5). The actual elements used were 6–node triangular elements with biquadratic continuous interpolation functions in space and linear discontinuous interpolation functions in time.

FEM–meshes are created by a Delaunay–type mesh generator (GIDCIMNE). Furthermore, the hybrid velocity integration (HVI) method is applied, which is based on a pure velocity formulation of the governing first–order equations in time. According to the applied discontinuous interpolation functions in the temporal domain, the inherent displacement field can be calculated in a subsequent, i.e. post–processing step. Thus, a classical solution technique based on the numerical investigation of a set of first–order equations in time can be circumvented. Technical details and further numerical comparisons between classical FEM schemes and DGT or HVI techniques are explained by Chen *et al.* (2008). According to the classical Bubnov–Galerkin scheme, interpolation and test functions belong to the same function space leading to an algebraic system of equations with symmetric matrices. In the present numerical scheme, the temporal inter–element continuity is enforced by a special flux treatment technique (Chen *et al.*, 2006). Thus, stable and efficient numerical results with a low amount of numerical dispersion and dissipation are obtained with rather large time steps.
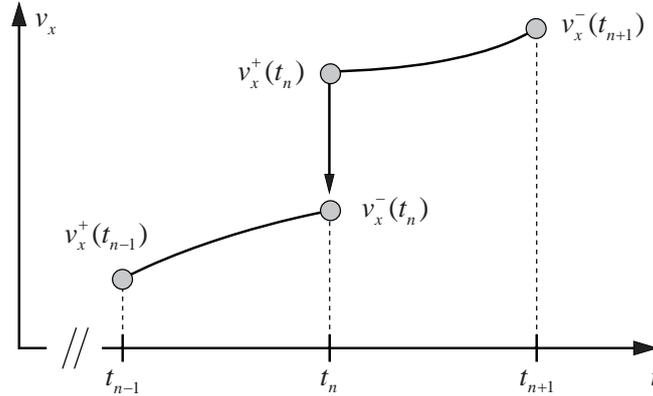
Figure 2.5: Discontinuous interpolation functions of the time–discontinuous Galerkin method (DGT) in the time domain. At time t_n two degrees of freedom for v_x are necessary, one for the time–element $[t_{n-1} \ \ t_n]$ and one for the time–element $[t_n \ \ t_{n+1}]$.

2.3.4. Analytical solution

The analytical solution of the scattering problem displayed in Figure 2.1a) is described by Liu *et al.* (2000). It provides the full seismogram at any synthetic receiver in the model domain. Such a synthetic receiver is defined in terms of cylindrical coordinates

r and θ for a coordinate system centred at the inclusion center. The solution in terms of displacement potentials takes the following form for synthetic receivers outside the inclusion:

$$\varphi\left(t, r, \theta\right) \;=\; \int\limits_{-\infty}^{+\infty} G\left(\omega\right) \left(\sum_{m=0}^{+\infty} A_m H_m^{(1)}\left(k_P r\right) \cos\left(m\theta\right)\right) e^{-i\omega t} d\omega, \tag{2.5}$$

$$\psi\left(t, r, \theta\right) \;=\; \int\limits_{-\infty}^{+\infty} G\left(\omega\right) \left(\sum_{m=1}^{+\infty} B_m H_m^{(1)}\left(k_S r\right) \sin\left(m\theta\right)\right) e^{-i\omega t} d\omega. \tag{2.6}$$

In Equations 2.5 and 2.6 φ and ψ are the displacement potentials of the P– and the S–wave, respectively, $G\left(\omega\right)$ is the complex–valued frequency spectrum of the displacement potential of the incident wave, ω is angular frequency, $H_m^{(1)}$ is the Hankel function of the first kind of order m and k_P and k_S are the wave numbers of the P– and the S–wave, respectively. The two rather complicated coefficients A_m and B_m are given in the Appendix of Liu *et al.* (2000) and are determined from the boundary condition at the inclusion interface. To get the final solution the integrals from $-\infty$ to $+\infty$ and the summations over m have to be calculated numerically. Both the number of summands and the finite integration and summation boundaries are chosen in a way that the summation converges to a constant value. From Equations 2.5 and 2.6 the displacement field of the scattered wave can be separated into P– and S–wave fields ($\mathbf{u}^P$ and $\mathbf{u}^S$), each separated into x– and y–components (u_x^i and u_y^i) using

$$u_x^P\left(t, x, y\right) \;=\; \frac{\partial \varphi\left(t, r, \theta\right)}{\partial r} \cos\theta - \frac{1}{r} \frac{\partial \varphi\left(t, r, \theta\right)}{\partial \theta} \sin\theta, \tag{2.7}$$

$$u_y^P\left(t, x, y\right) \;=\; \frac{\partial \varphi\left(t, r, \theta\right)}{\partial r} \sin\theta + \frac{1}{r} \frac{\partial \varphi\left(t, r, \theta\right)}{\partial \theta} \cos\theta, \tag{2.8}$$

$$u_x^S\left(t, x, y\right) \;=\; \frac{1}{r} \frac{\partial \psi\left(t, r, \theta\right)}{\partial \theta} \sin\theta - \frac{\partial \psi\left(t, r, \theta\right)}{\partial r} \cos\theta, \tag{2.9}$$

$$u_y^S\left(t, x, y\right) \;=\; \frac{1}{r} \frac{\partial \psi\left(t, r, \theta\right)}{\partial \theta} \cos\theta + \frac{\partial \psi\left(t, r, \theta\right)}{\partial r} \sin\theta. \tag{2.10}$$

2.4. Results

In Figure 2.6 the synthetic seismograms at the receiver location indicated in Figure 2.1a) are plotted as gray lines for all different numerical methods and for different spatial and temporal resolutions. In Table 2.2 numerical parameters of all performed simulations are given. The red lines in Figure 2.6 are calculated using the analytical solution of Liu *et al.* (2000). In y–direction (Figure 2.6a) the first event recorded is the incident plane P–wave. Later events are the scattered P–wave and the scattered S–wave (P–to–S–converted) that are overlapping and, therefore, not distinguishable. In x–direction (Figure 2.6b) the incident wave is not present and only the scattered wavefield is recorded. The lowest–resolution numerical simulations differ significantly from the analytical solution, especially towards the end of the seismogram. However, the majority of the simulations fit the analytical solution very well. This applies for the shape of the seismogram, amplitudes and arrival times. The seismograms in Figure 2.6 are used to calculate the L2 error norm in both x– and y–directions,

$$L2_{x,y} = \sqrt{\frac{\sum\limits_{i=1}^{nt} \left(u_{x,y}^{\mathrm{num}}(t_i) - u_{x,y}^{\mathrm{ana}}(t_i)\right)^2}{\sum\limits_{i=1}^{nt} \left(u_{x,y}^{\mathrm{ana}}(t_i)\right)^2}}, \tag{2.11}$$

where u_i^{num} is the particle displacement obtained from a numerical simulation and u_i^{ana} is the particle displacement obtained analytically. Figure 2.7 compares the L2 error norm for displacements in x– and y–direction for the different numerical methods. The errors in the two directions follow approximately a linear trend with increasing resolution whereas the error for displacement in y–direction is consistently smaller than in x–direction. This is already visible in Figure 2.6. For further analysis only the y–component of the displacement (Figure 2.6a) is considered. Due to the linear trend of the errors in the two directions (Figure 2.7), results of the error analysis for displacements in x–direction are comparable.
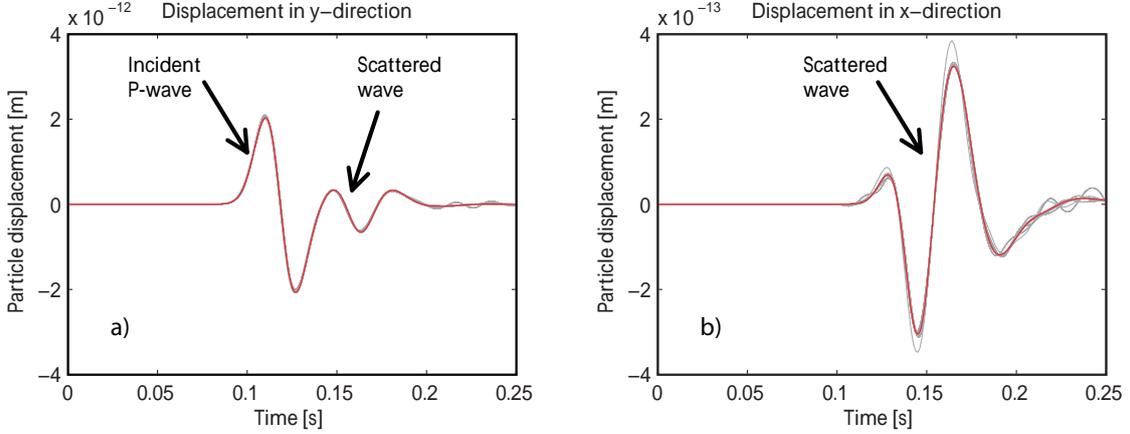
Figure 2.6: Synthetic seismograms (displacement–time–signal) at the receiver shown in Figure 2.1a). Gray lines show seismograms obtained from numerical simulations for all different numerical methods. Red lines are the synthetic seismograms obtained analytically. a) Particle displacement in y–direction and b) x–direction. Note the different scales in the two subfigures.
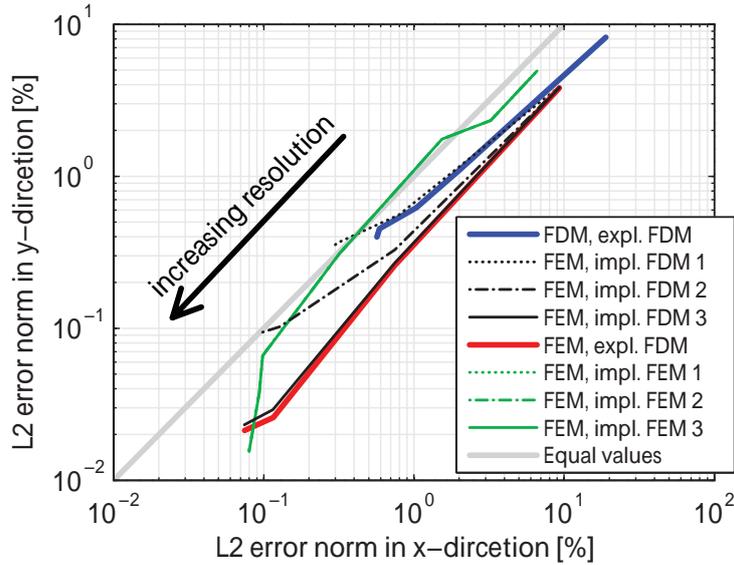
Figure 2.7: L2 error norm for particle displacement in y–direction plotted versus L2 error norm for particle displacement in x–direction. Different lines correspond to different numerical methods and/or different implicit time increments. First abbreviations in the legend before the comma (FDM or FEM) stands for the spatial discretization method, second abbreviation stands for the time discretization whereas expl. refers to explicit time integration and impl. refers to implicit time integration. Implicit time increments for both temporal FDM and temporal FEM are: 1: $\Delta t = 2.37 \times 10^{-4}$ s; 2: $\Delta t = 1.19 \times 10^{-4}$ s; 3: $\Delta t = 2.69 \times 10^{-5}$ s.

25

FDM in space and explicit FDM in time

# Nodes total	1'490'841	1'002'001	549'081	212'521	40'401
# Nodes incl.	10'108	15'380	7'860	1'976	80
Δt [10^{-5} s]	7.04	8.05	11.3	22.5	110

FEM in space and implicit FDM in time

# Nodes total	216'705	112'409	40'049	10'349
# Nodes incl.	21'392	5'516	826	210

FEM in space and explicit FDM in time

# Nodes total	216'705	112'409	40'049	10'349
# Nodes incl.	21'392	5'516	826	210
Δt [10^{-5} s]	0.64	1.43	5.38	13.8

FEM in space and implicit FEM in time

# Nodes total	287'725	128'369	72'821	33'405
# Nodes incl.	4'144	3'528	3'528	3'528
# Nodes total	13'249	9'089	7'005	
# Nodes incl.	3'528	3'528	3'528	

Table 2.2: Numerical parameters for all simulations performed in this study. # Nodes total is the total number of numerical nodes in the domain, # Nodes incl. is the number of numerical nodes that belong to the inclusion, Δt is the time increment in 10^{-5} s. Explicit time increments are calculated using the von Neumann stability criterion and are directly given in the table. Three implicit time increments are chosen freely and not given in the table: 1: $\Delta t = 2.37 \times 10^{-4}$ s; 2: $\Delta t = 1.19 \times 10^{-4}$ s; 3: $\Delta t = 2.69 \times 10^{-5}$ s. Each geometrical setup that is solved implicitly is solved with each of the three time increments.

In the following sections the accuracy of the different numerical methods is analyzed as a function of spatial and temporal resolution (Table 2.2). For explicit methods spatial and temporal resolutions are not independent from each other because the time increment is calculated with the von Neumann stability criterion, which is a function of the spatial resolution. Therefore, effects of spatial and temporal resolutions cannot be separated completely for explicit methods.

2.4.1. Effect of spatial resolution

With each numerical method a series of simulations with changing spatial resolution was performed (Table 2.2). Figure 2.8 shows the L2 error norm for the particle displacement in y–direction as a function of the number of degrees of freedom for the different methods. Figure 2.8a) considers the total number of degrees of freedom in the whole numerical domain and Figure 2.8b) considers only the degrees of freedom inside the inclusion. All methods become more accurate with increasing spatial resolution. However, for the same number of degrees of freedom (Figure 2.8a) the spatial FEM is more than one order of magnitude more accurate than the spatial FDM. Also, the method using the FEM in space and the implicit FDM in time clearly shows an effect of the chosen time increment. Larger time increments give less accurate results and the difference in accuracy increases with increasing spatial resolution. At the same time the method using the FEM in both space and time does not show this effect and the lines for the two different time increments lie virtually on top of each other.

The results change considerably when only the number of degrees of freedom inside the heterogeneity (Figure 2.8b) is considered. Methods using the FEM in space are still more accurate than the FDM in space but the difference is much smaller. This is largely due to the fact that the numerical FEM–mesh can vary significantly while the spatial variation of the FDM–mesh is limited. The method using the FEM in space and the FDM in time makes use of this advantage. The spatial resolution is increased inside and at the boundary of the inclusion while the resolution outside the inclusion is considerably lower. The meshgenerator used by the method using the FEM in space and the FEM in time keeps the resolution inside and at the boundary of the inclusion constant while the resolution in the surrounding media is increased (Table 2.2). This leads to the almost vertical line in Figure 2.8b).
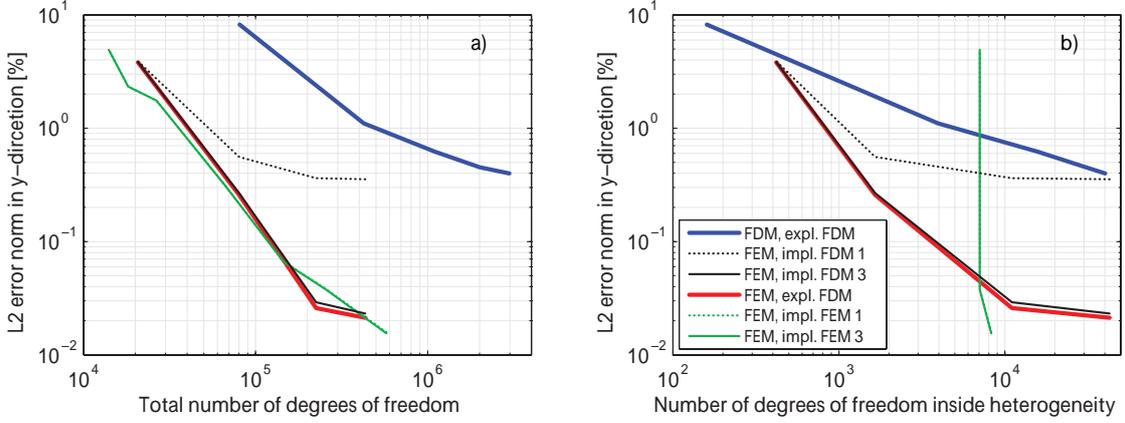
Figure 2.8: L2 error norm for particle displacement in y–direction plotted versus a) total number of degrees of freedom in the numerical domain and b) number of degrees of freedom inside the circular inclusion. The legend is valid for both subfigures and is explained in detail in Figure 2.7.
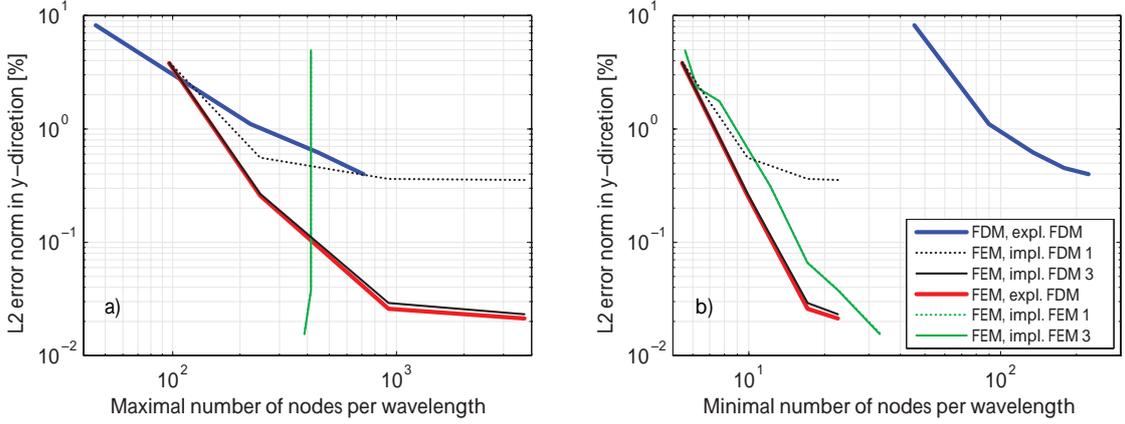
Figure 2.9: L2 error norm for particle displacement in y–direction plotted versus number of numerical nodes per dominant wavelength. To calculate the number of nodes per dominant wavelength the shortest distance between two nodes in the whole numerical domain is used in a). In b) the longest distance between two nodes in the whole numerical domain is used. The legend is valid for both subfigures and is explained in detail in Figure 2.7.

Figure 2.9 is similar to Figure 2.8 but uses as a measure for spatial resolution the number of numerical nodes per dominant wavelength (157.1 m). Because the spatial resolution can vary within the numerical domain (for both the spatial FEM and the spatial FDM) two measures are considered. Figure 2.9a) considers the minimal and Figure 2.9b) con-

siders the maximal distance between two neighboring nodal points within the whole numerical domain. The minimal distance between two nodal points (i.e. highest spatial resolution) is on the boundary of the inclusion for all methods. Therefore, Figures 2.8b) and 2.9a) look very similar. However, the line representing the spatial FDM is shifted even more to the left relative to the lines representing spatial FEM compared to Figure 2.8a) and b). Again, this is an effect of the varying grid spacing of the spatial FEM–mesh. Also the discrepancy between Figure 2.9a) and b) can be explained with the unstructured FEM–mesh. While the grid spacing for the spatial FDM does not vary significantly, the FEM–mesh can have larger spacing away from the inclusion. This shifts all lines representing the spatial FEM to the left relative to the spatial FDM in Figure 2.9b) compared to Figure 2.9a).

2.4.2. Effect of temporal resolution

While for explicit schemes the time increment decreases with increasing spatial resolution according to the von Neumann stability criterion, no such criterion exists for implicit schemes and the time increment can be chosen freely. To test the effect of temporal resolution implicit simulations were performed with three different time increments (Table 2.2). Figure 2.10 shows the L2 error norm for the particle displacement in y–direction as a function of the time increment used in the simulations. Considering only the two explicit schemes, Figure 2.10 resembles Figure 2.9a). The difference is a result of the two slightly different stability criteria for the explicit time increments that were applied to the spatial FDM and spatial FEM. The spatial FEM results in a smaller explicit time increment because the numerical mesh can be locally very fine whereas the FDM–mesh is more uniform. However, the two explicit schemes follow a common trend of increasing accuracy with decreasing time increment.

For implicit schemes the different lines in Figure 2.10 represent simulations with the same spatial resolution but different time increments. For low spatial resolution there is no effect of the time increment. This means that the accuracy is limited by the spatial resolution. Thus, the time increment of the coupled space–time FEM could be even enlarged. However, for comparison reasons, this was not done in the present investigation, but was studied in detail in Chen *et al.* (2008). For higher spatial resolution the method

using the FEM in space and the FDM in time clearly shows higher accuracy for smaller time increments. The accuracy for a given spatial resolution is limited by the applied time increments. The same accuracy can be achieved by using either a smaller time increment or a higher spatial resolution. At the same time the method using the FEM in both space and time is unaffected by the changing time increment for all spatial resolutions. The accuracy is limited by the spatial resolution.
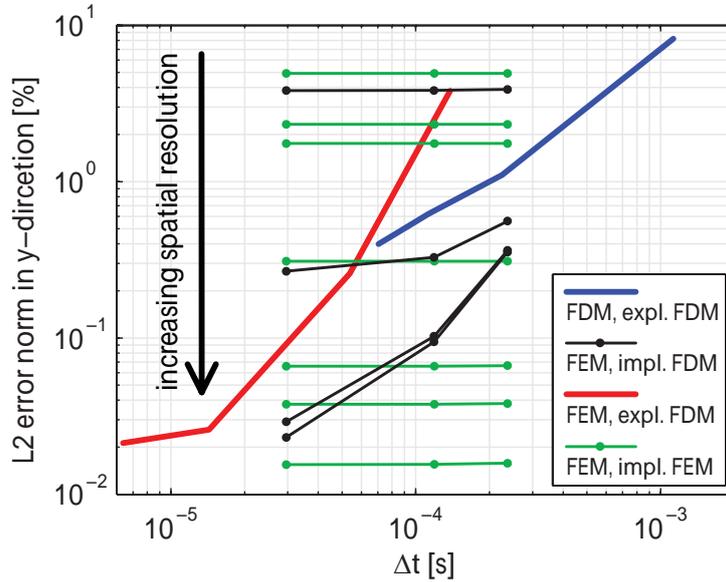
Figure 2.10: L2 error norm for particle displacement in y–direction plotted versus the applied time increment. Abbreviations in the legend are explained in detail in Figure 2.7. For implicit schemes the different lines represent the same spatial resolution but different time increments.

2.4.3. Effect of computation time

The two numerical algorithms using the FDM in time are implemented in MATLAB while the algorithm using the FEM in time is implemented in C. Also, the different simulations were not all performed on the same computer. Therefore, it is difficult to compare all the simulations. However, Figure 2.11 shows the L2 error norm for the particle displacement

in y–direction as a function of computation time per time increment (Figure 2.11a) and as a function of total computation time (Figure 2.11b) for all performed simulations. For increasing resolution (i.e. higher accuracy) implicit calculations in C perform faster than in MATLAB.
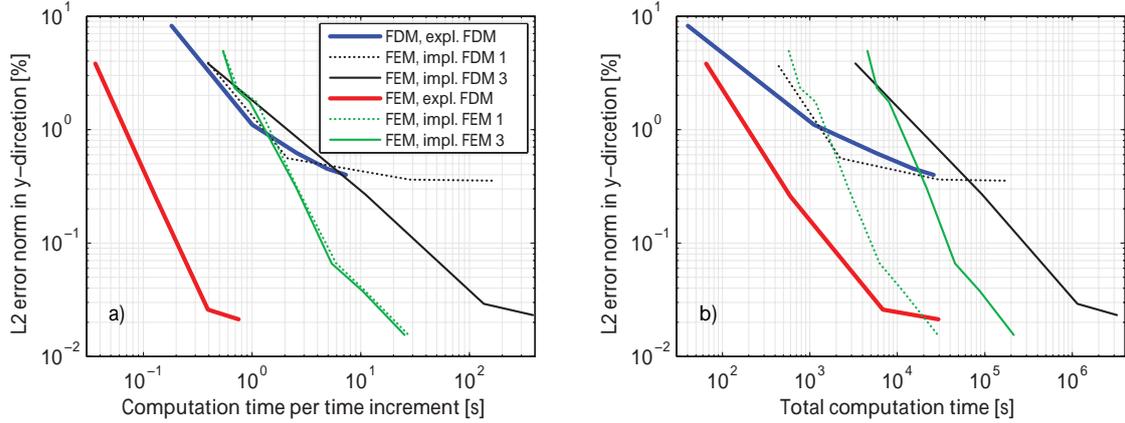
Figure 2.11: L2 error norm for particle displacement in y–direction plotted versus a) computation time (CPU time) per time increment and b) total computation time (CPU time) for the whole simulation. The legend is valid for both subfigures and is explained in detail in Figure 2.7.

To achieve a given accuracy the method using the FEM in space and the explicit FDM in time performs fastest. This is especially true when only one time increment is considered (Figure 2.11a). Then the method using the FEM in space and the explicit FDM in time performs more than an order of magnitude faster than all other methods for a given accuracy. The unstructured FEM–mesh allows having a high spatial resolution at the inclusion boundary without the need of a high resolution away from the inclusion. This leads to accurate solutions with amuch smaller number of total grid points compared to the spatial FDM and therefore also to faster performance. However, high resolution at the inclusion boundary also results in a small explicit time increment (von Neumann stability criterion) and therefore to a high number of time steps. Considering total computation time (Figure 2.11b) the difference between the method using the FEM in space and the explicit FDM in time and all other methods is therefore smaller. However, it still performs a factor two (or more) faster than the other methods for a given accuracy.

Considering only one time increment (Figure 2.11a) the implicit methods using the FEM in space perform as fast as the method using the FDM in both space and time, although this is an explicit method. The slower performance that is expected with implicit methods is compensated by the fact that the unstructured FEM–mesh needs much less numerical nodes for the same accuracy compared to spatial FDM (Figure 2.8a). Due to the different numbers of time steps for the different methods the lines representing the different methods in Figure 2.11b) are much further apart from each other compared to Figure 2.11a).

2.5. Discussion

The spatial FEM generally gives better results compared to the spatial FDM for the presented geometrical setup. The unstructured FEM–mesh allows a very accurate spatial approximation of the circular inclusion, or any other heterogeneity, without introducing a staircase–like material boundary. In addition, the unstructured FEM–mesh allows higher spatial resolution where it is needed without the need of high spatial resolution in other regions of the domain. This reduces the required number of grid points compared to the rectangular FDM–meshes. A desired accuracy can also be achieved with the spatial FDM, but a much higher number of numerical grid points is needed. This advantage of the spatial FEM will be even more important in three–dimensional simulations where the number of grid points increases more rapidly. Other methods, such as the finite volume method, are also able to handle unstructured meshes and are expected to show similar accuracies as the spatial FEM. Taking the aspect of computation time into account, the best method shown in this study is the FEM in space and the explicit FDM in time. It has both the advantage of the unstructured mesh and of the fast explicit time integration. Simulations are both accurate and fast.

From a programming point of view the spatial FDM is the simplest numerical method and is also commonly used for numerical wave propagation simulations. Therefore, it is worth to evaluate the desired accuracy and calculation time for a particular problem. For many applications the spatial FDM gives accurate enough results and/or the resolution can be set high enough to provide the desired accuracy. A further advantage is that no third–party mesh generator is necessary for the spatial FDM. Therefore, the

numerical mesh is under full control. The spatial FEM with the FDM in time is slightly more complex to implement but leads to more accurate results. The space–time FEM algorithm is more complex and is not a trivial extension of the spatial FEM with the FDM in time. For discontinuous elements in time used here each spatial nodal point requires twice as many degrees of freedom compared to the spatial FEM with the FDM in time. Interpolation functions in time have to be independent of interpolation functions in space and integration schemes have to be varied. The space–time FEM is compared quantitatively and qualitatively with the spatial FEM combined with the FDM in time by Chen *et al.* (2006, 2008). A big advantage is the fact that it is straightforward to implement interpolation functions that are higher order in time (e.g. second or fourth order) that result in a higher convergence rate. In the ideal case interpolation functions in time adapt to the actual problem solved.

The analytical solution provided by Liu *et al.* (2000) is expressed as integrals and sums (Equations 2.5 and 2.6) that need to be calculated numerically. This results in a relatively lengthy numerical algorithm. It has to be made sure that the number of summands and the finite boundaries for integration and summation are chosen in a way that the solution converges. The seismogram (displacement–time–signal) for a synthetic receiver can be calculated with reasonable computation time because the number of time increments used is not too big. A snapshot as in Figure 2.1 for a high spatial resolution would need a large computational effort. Also, the coefficients of the analytical solution are so complicated and long that it is difficult to gain good physical insight in the scattering process from the provided formulas.

Generally, the comparison between the different methods is not straightforward. In explicit schemes spatial resolution and the time increment are tightly coupled through the von Neumann stability criterion. Therefore, the effect of the two on the accuracy of the numerical solution cannot easily be separated. The spatial FDM and the spatial FEM use a completely different numerical mesh. Therefore, it is also difficult to compare the spatial resolution of the two methods and several attributes describing the spatial resolution have to be considered for comparison.

2.6. Conclusions

The analytical solution for the simple scattering problem studied here is in fact expressed as infinite integrals and sums. It is therefore not a pure analytical solution and a numerical algorithm is required to calculate the values of the analytical solution. For more geometrically complicated scattering problems numerical methods become essential.

The FDM and the FEM are two different numerical methods to spatially discretize the geometry of the scattering problem. Both methods have advantages and disadvantages but the main advantage of the FEM is the application of unstructured numerical meshes while the FDM needs rectangular meshes. Therefore, the FEM provides the same numerical accuracy as the FDM but requires significantly less numerical grid points. This is a result of the unstructured mesh that allows high resolution where it is needed with lower resolution elsewhere in the model domain. Also, the boundaries of heterogeneities can be better resolved with unstructured meshes and the FEM does not require interpolation of material properties which is required for the FDM using a velocity–stress formulation on a staggered grid. On the other hand, an advantage of the FDM is the considerably simpler numerical implementation.

The results show that the numerical accuracy does not improve by using implicit time integration schemes (FDM or FEM) instead of explicit ones (FDM). Therefore, for the presented geometrical setup of a circular inclusion inside a homogeneous medium, the numerical algorithm consisting of the FEM in space combined with the explicit FDM in time is the best choice which provides accurate results and performs fastest.

Acknowledgements

References

Achenbach J. D., 1973: **Wave propagation in elastic solids**, Volume 16 of North-Holland series in Applied Mathematics and Mechanics, North-Holland Publishing Company, Amsterdam, ISBN 0-7204-2367-8

Aki K. and Richards P. G., 2002: **Quantitative seismology**, 2nd Edition, University Science Books, Sausalito, ISBN 0-9357-0296-2

Ames W. F., 1992: **Numerical methods for partial differential equations**, 3rd Edition, Series in computer science and scientific computing, Academic Press Inc., San Diego, ISBN 0-1205-6761-X

Argyris J. H. and Scharpf D. W., 1969: **Finite elements in time and space**, Nuclear Engineering and Design 10, 456–464

Bathe K.-J., 1996: **Finite element procedures**, 2nd Edition, Prentice Hall, Englewood Cliffs, ISBN 0-1330-1458-4

Ben-Menahem A. and Jit Singh S., 1981: **Seismic waves and sources**, Springer Verlag, New York, ISBN 0-3879-0506-5

Bohlen T. and Saenger E. H., 2006: **Accuracy of heterogeneous staggered-grid finite-difference modeling of Rayleigh waves**, Geophysics 71, T109–T115, doi: 10.1190/1.2213051

Carcione J. M., Herman G. C. and ten Kroode A. P. E., 2002: **Seismic modeling**, Geophysics 67, 1304–1325, doi:10.1190/1.1500393

Carcione J. M., Helle H. B. and Pham N. H., 2003: **White's model for wave propagation in partially saturated rocks: Comparison with poroelastic numerical experiments**, Geophysics 68, 1389–1398, doi:10.1190/1.1598132

Carcione J. M., Cavallini F., Santos J. E., Ravazzoli C. L. and Gauzellino P. M., 2004: **Wave propagation in partially saturated porous media: Simulation of a second slow wave**, Wave Motion 39, 227–240, doi:10.1016/j.wavemoti.2003.10.001

Cerveny V., 2001: **Seismic ray theory**, Cambridge University Press, Cambridge, ISBN 0-5213-6671-2

Chen Z. Y., Steeb H. and Diebels S., 2006: **A time-discontinuous Galerkin method for the dynamical analysis of porous media**, International Journal for Numerical and Analytical Methods in Geomechanics 30, 1113–1134, doi:10.1002/nag.516

Chen Z. Y., Steeb H. and Diebels S., 2008: **A new hybrid velocity integration method applied to elastic wave propagation**, International Journal for Numerical Methods in Engeneering 74, 56–79, doi:10.1002/nme.2167

Cohen G. C., 2002: **Higher-order numerical methods for transient wave equations**, Series in scientific computation, Springer Verlag, Berlin, ISBN 3-5404-1598-X

Frehner M., Schmalholz S. M., Saenger E. H. and Steeb H., 2008: **Comparison of finite difference and finite element methods for simulating two-dimensional scattering of elastic waves**, Physics of the Earth and Planetary Interiors 171, 112–121, doi:10.1016/j.pepi.2008.07.003

Fried I., 1969: **Finite-element analysis of time-dependent phenomena**, AIAA Journal 7, 1170–1173

Higham N. J., 1996: **Accuracy and stability of numerical algorithms**, Society for Industrial and Applied Mathematics, Philadelphia, ISBN 0-8987-1355-2

Hughes T. J. R., 1987: **The finite element method: Linear static and dynamic finite element analysis**, Dover Publications, Mineola, ISBN 0-4864-1181-8

Kelly K. R. and Marfurt K. J., 1990: **Numerical modeling of seismic wave propagation**, Volume 13 of Geophysics reprint series, Society of Exploration Geophysicists, Tulsa, ISBN 1-5608-0011-9

Korneev V. A. and Johnson L. R., 1996: **Scattering of P and S waves by a spherically symmetric inclusion**, Pure and Applied Geophysics 147, 675–718

Krüger O. S., Saenger E. H. and Shapiro S. A., 2005: **Scattering and diffraction by a single crack: An accuracy analysis of the rotated staggered grid**, Geophysical Journal International 162, 25–31, doi:10.1111/j.1365-246X.2005.02647.x

Lindsay R. B., 1960: **Mechanical radiation**, International series in pure and applied physics, McGraw-Hill, New York, ISBN 0-0703-7844-0

Liu Y. B., Wu R.-S. and Ying C. F., 2000: **Scattering of elastic waves by an elastic or viscoelastic cylinder**, Geophysical Journal International 142, 439–460

Love A. E. H., 1944: **A treatise on the mathematical theory of elasticity**, 4th Edition, Dover books on physics and chemistry, Dover Publications, New York, ISBN 0-4866-0174-9

Masson Y. J. and Pride S. R., 2007: **Poroelastic finite difference modeling of seismic attenuation and dispersion due to mesoscopic-scale heterogeneity**, Journal of Geophysical Research 112, B03204, doi:10.1029/2006JB004592

Mavko G., Mukerji T. and Dvorkin J., 2003: **The rock physics handbook: Tools for seismic analysis in porous media**, Cambridge University Press, Cambridge, ISBN 0-5215-4344-4

Moczo P., Kristek J., Vavrycuk V., Archuleta R. J. and Halada L., 2002: **3D heterogeneous staggered-grid finite-difference modeling of seismic motion with volume harmonic and arithmetic averaging of elastic moduli and densities**, Bulletin of the Seismological Society of America 92, 3042–3066

Moczo P., Robertsson J. O. A. and Eisner L., 2007: **The finite-difference time-domain method for modeling of seismic wave propagation**, in Advances in Geophysics, Volume 48, Elsevier Academic Press Inc., San Diego, pages 421–516, doi:10.1016/S0065-2687(06)48008-0

Moser T. J. and Pajchel J., 1997: **Recursive seismic ray modelling: Applications in inversion and VSP**, Geophysical Prospecting 45, 885–908

Newmark N. M., 1959: **A method of computation for structural dynamics**, Journal of the Engeneering Mechanics Division 85, 67–94

Saenger E. H., Gold N. and Shapiro S. A., 2000: **Modeling the propagation of elastic waves using a modified finite-difference grid**, Wave Motion 31, 77–92

Saenger E. H., Ciz R., Krüger O. S., Schmalholz S. M., Gurevich B. and Shapiro S. A., 2007: **Finite-difference modeling of wave propagation on microscale: A snapshot of the work in progress**, Geophysics 72, SM293–SM300, doi:10.1190/1.2753552

Sanchez-Sesma F. J. and Iturraran-Viveros U., 2001: **Scattering and diffraction of SH waves by a finite crack: An analytical solution**, Geophysical Journal International 145, 749–758

Santos J. E., Ravazzoli C. L., Gauzellino P. M. and Carcione J. M., 2005: **Numerical simulation of ultrasonic waves in reservoir rocks with patchy saturation and fractal petrophysical properties**, Computational Geosciences 9, 1–27, doi: 10.1007/s10596-005-2848-9

Shewchuk J. R., 1996: **Triangle: Engeneering a 2D quality mesh generator and delaunay triangulator**, in Applied Computational Geometry: Towards Geometric Engeneering, Volume 1148 of Lecture Notes in Computer Science, Springer Verlag, Berlin, pages 203–222, (From the First ACM Workshop on Applied Computational Geometry)

Shewchuk J. R., 2002: **Delaunay refinement algorithms for triangular mesh generation**, Computational Geometry 22, 21–74

Smith G. D., 1985: **Numerical solutions of partial differential equations: Finite difference methods**, 3rd Edition, Oxford applied mathematics and computing science series, Oxford University Press, Oxford, ISBN 0-1985-9650-2

Virieux J., 1986: **P-Sv-wave propagation in heterogeneous media: Velocity-stress finite-difference method**, Geophysics 51, 889–901

White R. M., 1958: **Elastic wave scattering at a cylindrical discontinuity in a solid**, Journal of the Acoustical Society of America 30, 771–785

Ying C. F. and Truell R., 1956: **Scattering of a plane longitudinal wave by a spherical obstacle in an isotropically elastic solid**, Journal of Applied Physics 27, 1086–1097

Zienkiewicz O. C. and Taylor R. L., 2000: **The finite element method: The Basis**, Volume 1, 5th Edition, Butterworth-Heinemann, Oxford, ISBN 0-7506-5049-4

3 Finite element simulations of Stoneley guided wave reflection and scattering at the tips of fluid–filled fractures

Abstract

The reflection and scattering of Stoneley guided waves at the tip of a crack filled with a viscous fluid is studied numerically in two dimensions using the finite element method. The rock surrounding the crack is fully elastic and the fluid filling the crack is elastic in its bulk deformation behavior and viscous in its shear deformation behavior. The crack geometry, especially the crack tip, is resolved in detail by the unstructured finite element mesh. At the tip of the crack the Stoneley guided wave is reflected. The reflection coefficient is calculated from numerical simulations, which provide values between 43 % and close to 100 % depending on the type of fluid filling the crack (water, oil or hydrocarbon gas), the crack geometry (elliptical or rectangular) and the presence of a small gas cap at the crack tip. The interference of incident and reflected Stoneley guided waves leads to nodes (zero amplitude) and anti–nodes. At anti–nodes the amplitude is increased. However, the exponential decay away from the crack is equal to or even stronger than that of an undisturbed Stoneley guided wave propagating along an infinite crack, which makes the Stoneley guided wave difficult to detect at relatively short distances away from the crack. The part of the Stoneley guided wave that is not reflected is scattered at the crack tip and as P– and S–waves emitted into the surrounding elastic rock. For fully saturated cracks the radiation pattern of these elastic body waves is almost point–symmetric around the crack tip. The emitted elastic body waves may allow detecting Stoneley guided wave–related resonant signals at distances away from the crack where the amplitude of the Stoneley guided wave itself is too small to be detected.

3.1. Introduction

Fractures in rocks are of great practical interest not only because they contribute significantly to the permeability of a rock (e.g. Faoro *et al.*, 2009) but also because they can have a significant influence on seismic waves that pass through fractured rocks. For example, Saenger and Shapiro (2002) showed with numerical simulations that the wave velocity of body waves decreases drastically with increasing crack density, Groenenboom and Falk (2000) modeled numerically and measured in the laboratory that scattering of body waves at hydraulic fractures is strong enough to determine the fracture dimensions and Ionov (2007) showed that fractures intersecting a bore hole can have a major impact in seismic surveys. One phenomenon of particular interest are Stoneley guided waves (SGW), a highly dispersive and slowly propagating wave mode that is bound to a crack (e.g. Ferrazzini and Aki, 1987; Ashour, 2000; Korneev, 2008). SGWs are also referred to as crack waves (Chouet, 1986; Yamamoto and Kawakatsu, 2008), slow Stoneley waves (Ferrazzini and Aki, 1987) or simply Stoneley waves in a fracture (Ashour, 2000). They are of interest due to their ability to develop a resonance when propagating back and forth along a crack, which "should lead to strongly frequency dependent propagation effects for seismic waves (Korneev, 2008)". Despite their potential importance for wave propagation in porous and fractured rocks, SGWs are not considered in existing effective medium and poroelastic theories, such as the Hudson–model (Hudson, 1980, 1981), the squirt flow model (Mavko and Jizba, 1991; Dvorkin *et al.*, 1995) or the Biot–model (Biot, 1962). Analytical studies of SGW propagation are available only for infinite straight cracks (Ferrazzini and Aki, 1987; Ashour, 2000; Korneev, 2008) not taking into account the reflection and scattering at crack tips. Numerical studies are rare (e.g. Chouet, 1986; Yamamoto and Kawakatsu, 2008) and only available for simple crack geometries (usually rectangular). This paper extends this body of knowledge by studying the propagation, reflection and scattering of SGWs at crack tips of different shapes and with a high numerical resolution.

The resonance caused by SGWs propagating in finite fractures was used by Aki *et al.* (1977), Chouet (1988) and Chouet (1996) to explain long–period volcanic tremor signals that are observed before volcanic eruptions and can potentially be used for eruption forecasting. The reflection coefficient at the crack tip together with the attenuation

determines how long a SGW survives propagating back and forth along a crack and therefore how well it can develop a resonance. Knowing that SGWs can not be detected a relatively short distance away from the crack due to the exponential decay of their amplitude (Ferrazzini and Aki, 1987), the way the tremor signal is transmitted to recording stations at the Earth's surface remained unclear. Ferrazzini and Aki (1987) suspected that "reflection at the crack tip should provide an important source of radiation in the case of a finite crack". However, the reflection of SGWs at the tip of a crack has not been investigated in detail, but is the main subject of this paper. The part of the SGW that is not reflected is scattered at the crack tip and P– and S–waves are radiated away from the crack tip. The radiation pattern of these P– and S–waves is of great importance for measuring the resonant behavior of the SGW (i.e. the tremor signal).

The study of SGWs is a multiscale problem where typical wavelengths can be orders of magnitudes larger than the characteristic size of the cracks. For numerical simulations this "presents a major computational challenge (Korneev, 2008)". The standard numerical method for simulating wave propagation in fractured media is the finite difference method (FDM) using a rectangular numerical grid (Chouet, 1986; Groenenboom and Falk, 2000; Saenger and Shapiro, 2002; Krüger *et al.*, 2005). The numerical method used in this study is the finite element method (FEM) (e.g. Zienkiewicz and Taylor, 2000; Cohen, 2002) that uses an unstructured numerical mesh. A similar method also using an unstructured mesh is for example the discontinuous Galerkin method described by Käser and Dumbser (2008). The unstructured mesh allows resolving geometrically complex objects with strong material contrast (e.g. the tip of a crack) very finely and accurately without the need of having a very high resolution elsewhere in the domain (Frehner *et al.*, 2008). In contrast, rectangular grids always approximate all objects in a staircase–like way, which leads to numerical inaccuracies no matter how fine the numerical grid is. For time integration in wave propagation simulations explicit schemes are most common. The largest explicit time increment allowed for stable numerical solutions is determined by the smallest spatial resolution and the largest wave velocity in the domain (Virieux, 1986; Higham, 1996; Saenger *et al.*, 2000). Both parameters take extreme values when SGWs are simulated. Spatial resolution needs to be very fine around the crack tip and the dispersive P–waves in the viscous fluid have a velocity tending to infinity for very large frequencies. Small–amplitude numerical noise, which is commonly characterized by high frequencies, can build up and lead to numerical instabilities. One possibility

to avoid these instabilities in viscous fluids is defining frequency dependent material parameters (Saenger *et al.*, 2005), which allows defining the high–frequency limit of the dispersive waves from infinity down to a finite value. The alternative used in this study is the use of an implicit time integration method (e.g. Chen *et al.*, 2008; Frehner *et al.*, 2008), which does not require fulfilling any stability criterion. Material parameters in the numerical algorithm can be implemented exactly the same way as they are written in the constitutive equations and do not have to be made frequency dependent.

The paper starts with a description of the mathematical and geometrical model. Properties of the SGW as a function of the model setup and the different fluids used in this study are described using analytical expressions of Ferrazzini and Aki (1987) and Korneev (2008). A brief introduction to the applied 2D FEM is given before the numerical results are shown. The reflection coefficient of a SGW at the tip of a crack is quantified as a function of crack geometry and the type of fluid filling the crack. The radiation pattern of P– and S–waves that are emitted into the surrounding rock is described in detail. The paper ends with simulations for two advanced model setups (two intersecting fractures and fractures filled with two different fluids) and a discussion about the applicability of the modeling results to natural environments.

3.2. Model

The propagation of SGWs is studied with a 2D model with Cartesian coordinates x and y. The mathematical description and the geometrical setup are described below.

3.2.1. Mathematical model

The force balance equation (or conservation of linear momentum) that describes the state of the acting forces in 2D (Love, 1944; Lindsay, 1960; Achenbach, 1973; Shames and Cozzarelli, 1997; Aki and Richards, 2002; Pujol, 2003) is given by

$$\rho \underbrace{\left\{ \begin{array}{c} \ddot{\tilde{u}}_x \\ \ddot{\tilde{u}}_y \end{array} \right\}}_{\ddot{\mathbf{u}}} = \underbrace{\begin{bmatrix} \frac{\partial}{\partial x} & 0 & \frac{\partial}{\partial y} \\ 0 & \frac{\partial}{\partial y} & \frac{\partial}{\partial x} \end{bmatrix}}_{\mathbf{B}^T} \underbrace{\left\{ \begin{array}{c} \sigma_{xx} \\ \sigma_{yy} \\ \sigma_{xy} \end{array} \right\}}_{\boldsymbol{\sigma}},$$

(3.1)

where ρ is density and $\ddot{\tilde{u}}$ is the second time derivative of the displacement vector. The symbol $\tilde{}$ denotes the continuous nature of $\ddot{\tilde{u}}$ (not yet discretized with any numerical method). Vector $\boldsymbol{\sigma}$ contains the three independent components σ_{ij} of the symmetric total stress tensor. Compressive stresses are defined as negative. Superscript T denotes the transpose of a matrix. The deformation behavior of the medium is divided into a bulk (or volumetric) part and a deviatoric (or shear) part. Therefore, the vector $\boldsymbol{\sigma}$ is also divided into a bulk and a deviatoric part (Shames and Cozzarelli, 1997):

$$\left\{ \begin{array}{c} \sigma_{xx} \\ \sigma_{yy} \\ \sigma_{xy} \end{array} \right\} = \left\{ \begin{array}{c} -p \\ -p \\ 0 \end{array} \right\} + \underbrace{\left\{ \begin{array}{c} s_{xx} \\ s_{yy} \\ s_{xy} \end{array} \right\}}_{\mathbf{s}}.$$

(3.2)

Vector $\mathbf{s}$ contains the three independent components s_{ij} of the symmetric deviatoric stress tensor and p is pressure (or mean stress). Vector $\boldsymbol{\varepsilon}$, containing the three independent components (two normal components ε_{ii} and shear component γ_{xy}) of the symmetric total strain tensor, is divided into a bulk and a deviatoric part in a very similar way:

$$\underbrace{\left\{ \begin{array}{c} \varepsilon_{xx} \\ \varepsilon_{yy} \\ \gamma_{xy} \end{array} \right\}}_{\boldsymbol{\varepsilon}} = \left\{ \begin{array}{c} \frac{\partial \tilde{u}_x}{\partial x} \\ \frac{\partial \tilde{u}_y}{\partial y} \\ \frac{\partial \tilde{u}_x}{\partial y} + \frac{\partial \tilde{u}_y}{\partial x} \end{array} \right\} = \left\{ \begin{array}{c} \frac{\Theta}{3} \\ \frac{\Theta}{3} \\ 0 \end{array} \right\} + \underbrace{\left\{ \begin{array}{c} e_{xx} \\ e_{yy} \\ g_{xy} \end{array} \right\}}_{\mathbf{e}}.$$

(3.3)

Vector $\mathbf{e}$ contains the three independent components (two normal components e_{ii} and shear component g_{xy}) of the symmetric deviatoric strain tensor and Θ is the bulk strain ($\varepsilon_{xx} + \varepsilon_{yy}$). Two different types of media are considered in this study, the rock (solid, superscript s) and the fluid (superscript f) that fills the crack. The behavior of both

media is the same as in Korneev (2008). The bulk deformation behavior of both media is linear elastic, while the deviatoric deformation behavior of the two media is different. The deviatoric deformation of the solid rock is linear elastic and that of the fluid is linear viscous. The constitutive equation for the elastic bulk deformation of both media is

$$- p = K^{s,f}\Theta, \tag{3.4}$$

where $K^{s,f}$ is the elastic bulk modulus of the solid and the fluid, respectively. The constitutive equation for the deviatoric deformation of the elastic solid is

$$\begin{Bmatrix} s_{xx} \\ s_{yy} \\ s_{xy} \end{Bmatrix} = \begin{bmatrix} 2\mu & 0 & 0 \\ 0 & 2\mu & 0 \\ 0 & 0 & \mu \end{bmatrix} \begin{Bmatrix} e_{xx} \\ e_{yy} \\ g_{xy} \end{Bmatrix}, \tag{3.5}$$

where μ is the elastic shear modulus. The constitutive equation for the viscous deviatoric deformation of the fluid is

$$\begin{Bmatrix} s_{xx} \\ s_{yy} \\ s_{xy} \end{Bmatrix} = \begin{bmatrix} 2\eta & 0 & 0 \\ 0 & 2\eta & 0 \\ 0 & 0 & \eta \end{bmatrix} \underbrace{\begin{Bmatrix} \dot{e}_{xx} \\ \dot{e}_{yy} \\ \dot{e}_{xy} \end{Bmatrix}}_{\dot{\mathbf{e}}}, \tag{3.6}$$

where η is the shear viscosity. Vector $\dot{\mathbf{e}}$ is the time derivative of vector $\mathbf{e}$. The formulation for total stress in the elastic solid is found by combining Equations 3.2, 3.3, 3.4 and 3.5 as

$$\begin{Bmatrix} \sigma_{xx} \\ \sigma_{yy} \\ \sigma_{xy} \end{Bmatrix} = \begin{bmatrix} K^s + \frac{4}{3}\mu & K^s - \frac{2}{3}\mu & 0 \\ K^s - \frac{2}{3}\mu & K^s + \frac{4}{3}\mu & 0 \\ 0 & 0 & \mu \end{bmatrix} \begin{Bmatrix} \frac{\partial \tilde{u}_x}{\partial x} \\ \frac{\partial \tilde{u}_y}{\partial y} \\ \frac{\partial \tilde{u}_x}{\partial y} + \frac{\partial \tilde{u}_y}{\partial x} \end{Bmatrix}. \tag{3.7}$$

The formulation for total stress in the fluid is found by combining Equations 3.2, 3.3, 3.4 and 3.6 as

$$
\begin{Bmatrix} \sigma_{xx} \\ \sigma_{yy} \\ \sigma_{xy} \end{Bmatrix} = \begin{bmatrix} K^f & K^f & 0 \\ K^f & K^f & 0 \\ 0 & 0 & 0 \end{bmatrix} \begin{Bmatrix} \frac{\partial \tilde{u}_x}{\partial x} \\ \frac{\partial \tilde{u}_y}{\partial y} \\ \frac{\partial \tilde{u}_x}{\partial y} + \frac{\partial \tilde{u}_y}{\partial x} \end{Bmatrix} + \begin{bmatrix} \frac{4}{3}\eta & -\frac{2}{3}\eta & 0 \\ -\frac{2}{3}\eta & \frac{4}{3}\eta & 0 \\ 0 & 0 & \eta \end{bmatrix} \begin{Bmatrix} \frac{\partial \dot{\tilde{u}}_x}{\partial x} \\ \frac{\partial \dot{\tilde{u}}_y}{\partial y} \\ \frac{\partial \dot{\tilde{u}}_x}{\partial y} + \frac{\partial \dot{\tilde{u}}_y}{\partial x} \end{Bmatrix}. \qquad (3.8)
$$

Equation 3.7 describes the stress–strain relation of a fully elastic medium in 2D where both the bulk and the shear deformation behavior are elastic. Therefore, P– and S–waves can propagate in such a medium without velocity dispersion or attenuation. Equation 3.8 describes the stress–strain relation of a so–called visco–acoustic medium (a viscous fluid) in 2D. Only the bulk deformation behavior is elastic while the shear deformation behavior is viscous. Therefore, shear waves exist exclusively due to viscosity and have a diffusive propagation type. On the other hand, P–waves can propagate in such a medium but they are attenuated by the viscous damping terms. The formulation is very similar to the one–dimensional formulation of a medium using a Kelvin–Voigt model (Bourbie *et al.*, 1987; Carcione, 2001). The P–wave phase velocity in the fluid V_P^f is dispersive with a low–frequency limit equal to $V_C = \sqrt{K^f/\rho^f}$. For increasing frequency the phase velocity increases continuously and goes to infinity without having a high–frequency limit. The quality factor for P–waves in such a visco–acoustic fluid Q_P^f is equal to infinity (no attenuation) in the low–frequency limit and $Q_P^f = 0$ (no propagation of waves) in the high–frequency limit. Setting the shear viscosity η to 0 leads to a purely acoustic formulation, also called an inviscid fluid. P–waves in an inviscid fluid propagate with the velocity V_C. They are neither dispersive nor attenuated. Equations 3.7 and 3.8 can be written in a more general way:

$$
\boldsymbol{\sigma} = \mathbf{D}_{\text{el}}\boldsymbol{\varepsilon} + \mathbf{D}_{\text{visc}}\dot{\boldsymbol{\varepsilon}}, \qquad (3.9)
$$

where, in the purely elastic case, $\mathbf{D}_{\text{el}}$ is the matrix given in Equation 3.7 and $\mathbf{D}_{\text{visc}}$ is equal to 0. In the visco–acoustic case, $\mathbf{D}_{\text{el}}$ is the first matrix given in Equation 3.8

and $\mathbf{D}_{\text{visc}}$ is the second matrix given in Equation 3.8. Equation 3.9 is substituted into Equation 3.1 to yield the total equations of motion:

$$\rho^{s,f}\ddot{\mathbf{u}} = \mathbf{B}^T\mathbf{D}_{\text{el}}\mathbf{B}\tilde{u} + \mathbf{B}^T\mathbf{D}_{\text{visc}}\mathbf{B}\dot{\tilde{u}}. \tag{3.10}$$

3.2.2. Geometrical model

For simulating SGWs and their behavior at a crack tip the three model setups shown in Figure 3.1 are used. The first model (labeled 1, dashed lines) consists of a straight horizontal crack of thickness h that runs through the whole model domain and is centered at $y = 0$. This model does not contain a crack tip. The SGW propagates undisturbed along the crack and can be compared with the analytical solutions for the phase velocity (Ferrazzini and Aki, 1987; Korneev, 2008). The second model (labeled 2, solid line) consists of half a crack that has an elliptical shape with a horizontal major axis $2L$ and a vertical minor axis h. The tip of the crack is located at $x = 0$ and $y = 0$. The third model (labeled 3, stippled line) consists of a straight horizontal crack of thickness h ending at a flat crack tip (i.e. rectangular crack geometry). The tip of the crack is located at $x = 0$ and $y = 0$. In both the second and the third model the SGW propagates along the crack and is partly reflected at the crack tip. In all three model setups, two vertical lines with virtual receivers recording the displacement field are located at $x/h = -70.0$ (Line 1) and $x/h = -3.3$ (Line 2), respectively. Because all model setups are symmetric around $y = 0$, receivers are only positioned in positive y–direction.

In all three models, the boundaries are far enough away from the crack to avoid boundary effects. Rigid wall boundary conditions (all displacements $u = 0$) are applied all around the model except for the position where the crack is in contact with the left boundary. There, only the displacement in y–direction is forced to vanish and the displacement in x–direction is prescribed by the time and space dependent boundary condition,

$$F(t,y) = -A_0 \frac{2(t-t_0)}{\tau^2} \exp\left\{-\frac{(t-t_0)^2}{\tau^2}\right\} \left[1 - \left(\frac{2|y|}{h}\right)^2\right] \text{ for } -\frac{h}{2} \leq y \leq \frac{h}{2}, \tag{3.11}$$

that acts as the external driving force. The time dependent part of $F(t, y)$ is the first derivative of a Gaussian, centered at time t_0. The space dependent part of $F(t, y)$ is a hyperbola with maximum amplitude 1 at $y = 0$ and zero amplitude at $y = \pm h/2$. The applied parameters are $A_0 = 10^{-2}$, $\tau = 5 \times 10^{-5}$ and $t_0 = 2 \times 10^{-4}$. This leads to a central frequency of the external force $f_0 = 4500$ Hz.
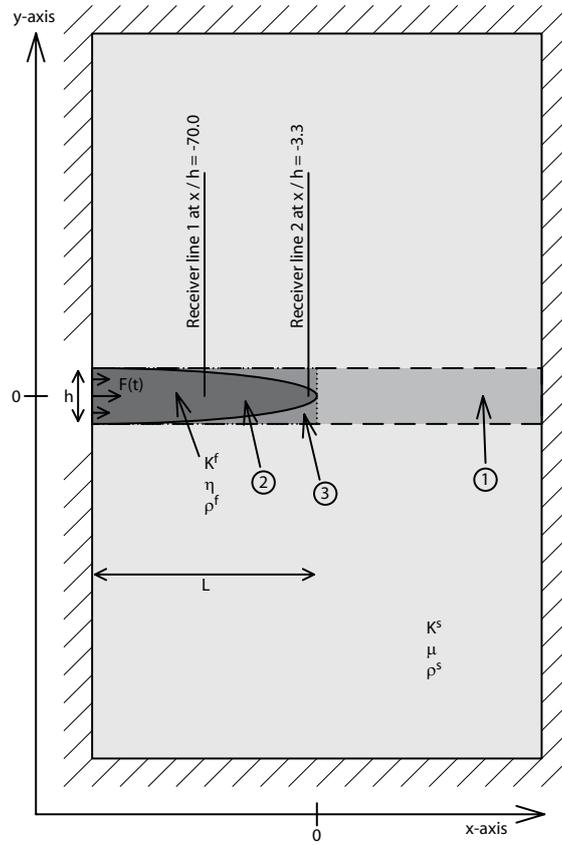
Figure 3.1: Sketches of the three model setups (labeled $1 - 3$) used for 2D numerical simulations. A crack filled with a fluid is surrounded by an elastic rock. Model 1 (dashed line): Straight horizontal crack with constant thickness that runs through the whole model domain. Model 2 (solid line): Half a crack that has an elliptical shape and ends inside the model domain. Model 3 (stippled line): Rectangular crack with constant thickness that ends inside the model domain at a flat crack tip. In all models two virtual vertical receiver lines are placed in positive y– direction. Hatched walls represent the rigid wall boundary conditions that are applied all around the model except for the position where the crack is in contact with the left boundary. There, time dependent boundary conditions act as the external source.

3.3. Model Properties

For the second and third model setups (Figure 3.1) the aspect ratio of the crack is $h/(2L) = 333$. While the elastic rock has the same properties throughout the entire study different fluids are defined to fill the crack. Table 3.1 lists the material parameters of the individual media and Table 3.2 lists the properties of the fluid–filled crack and of the SGW. Properties for the elastic rock and for water, oil and hydrocarbon gas agree with values of Ferrazzini and Aki (1987), Mavko *et al.* (2003) and Korneev (2008). The two dimensionless parameters C (crack stiffness) and F (viscous damping loss) are defined as in Chouet (1988):

$$C = \frac{K^f}{\mu} \frac{2L}{h}, \tag{3.12}$$

$$F = \frac{12\eta 2L}{\rho^f h^2 V_P^s}. \tag{3.13}$$

The applied material parameters lead to a ratio of $\lambda_{P0}^s/h = 170$, where λ_{P0}^s is the wavelength of a P–wave propagating in the elastic solid with the central frequency of the external source. The phase velocity of the SGW is a function of the elastic and visco–acoustic parameters of the rock and the fluid filling the crack, as well as the crack thickness and frequency. Dispersion curves for both inviscid and viscous fluids (Ferrazzini and Aki, 1987; Korneev, 2008, Figure 4 below) show a decrease of the phase velocity for low frequencies. For zero frequency the phase velocity is zero. The high frequency limit of the phase velocity of the SGW is that of a Scholte wave (Carcione and Helle, 2004) that is the interface wave at a single fluid–solid interface.

Figure 3.2 shows the phase velocity and the quality factor of the SGW propagating along a straight crack for a range of material parameters of the fluid together with the parameters used in this study (Table 3.1) for constant material parameters of the solid and for constant values of h and f_0. Figure 3.2 is produced by using the analytical solutions of Ferrazzini and Aki (1987) and of Korneev (2008) for inviscid and viscous fluids, respectively. For material parameters of water, oil and hydrocarbon gas, the

absolute phase velocity V_{SGW} for inviscid fluids (Figure 3.2a) lies within a very narrow range of 0.2 to 0.27 of the P–wave phase velocity in the elastic solid V_P^s. However, compared to the acoustic P–wave phase velocity in the inviscid fluid V_C the phase velocity of the SGW varies considerably for the different fluids (from $0.4V_C$ for water to $0.98V_C$ for hydrocarbon gas). The fluid parameters K^f and ρ^f for water, oil and hydrocarbon gas lie approximately on a straight line in double logarithmic representation (gray line in Figure 3.2a). This straight line is used as the abscissa in Figure 3.2b) and c) where the ordinate is the normalized viscosity of the fluid. The viscosities of water, oil and hydrocarbon gas are too small to have a significant effect on the phase velocity of the SGW compared to the inviscid case (bottom of Figure 3.2b). At the same time, the quality factor of the SGW (Figure 3.2c) is relatively large (more than 100) for the applied fluid viscosities and only very little attenuation of the SGW is expected.

Medium	Solid rock (superscript s)	Water	Oil	Gas
Bulk moduls K [GPa]	5	2.2	1.3	0.022
Ratio K/K^s	1	0.44	0.26	0.0044
Shear modulus μ	6	-	-	-
Shear viscosity η [Pa s]	-	1×10^{-3}	1×10^{-2}	2×10^{-5}
Ratio η/η^{Water}	-	1	10	0.02
Density ρ [kg/m^3]	2500	1000	800	100
Ratio ρ/ρ^s	1	0.4	0.32	0.04
P–wave phase velocity V_P [m/s]	2280.4	1483.2	1274.8	469.0
Ratio V_P/V_P^s	1	0.650	0.559	0.206
Low–frequency limit of $V_P^f = V_C$ [m/s]	-	1483.2	1274.8	469.0
Ratio V_C/V_P^s	-	0.650	0.559	0.206
Quality factor of P–wave in viscous fluid Q_P^f	-	5.8×10^7	3.4×10^6	2.9×10^7
S–wave phase velocity V_S [m/s]	1549.2	-	-	-
Ratio V_S/V_P^s	0.680	-	-	-

Table 3.1: Elastic and visco–acoustic material parameters for the different media used in this study. Superscripts s and f denote properties of the elastic rock (solid) and of the fluid, respectively. The dispersive P–wave phase velocity for viscous fluids V_P^f and the corresponding quality factor Q_P^f is calculated for the central frequency of the external force. The low–frequency limit of V_P^f (called V_C) is equal to V_P^f for an inviscid fluid. The P– and S–wave phase velocity for the elastic rock is not dispersive.
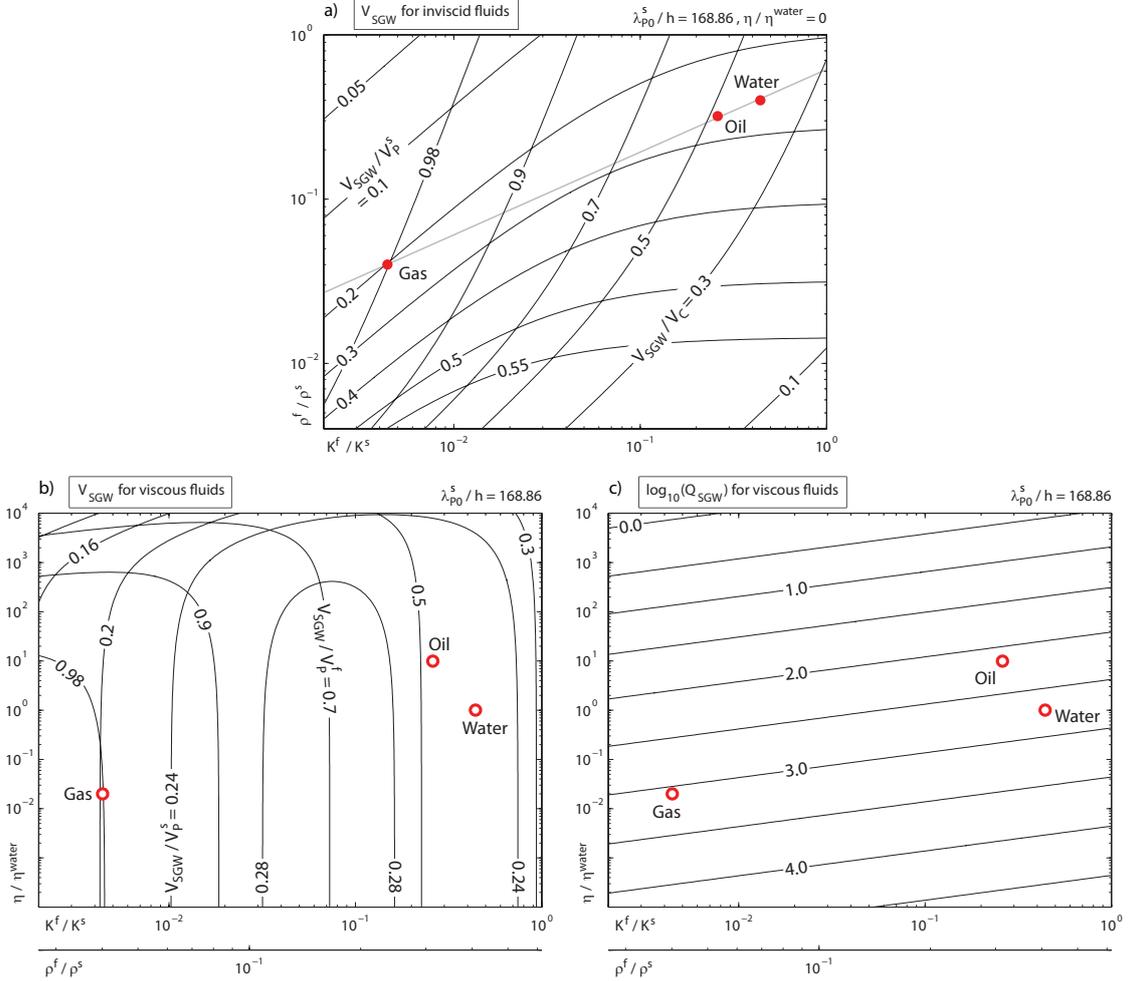
Figure 3.2: a) Contour lines of the SGW phase velocity V_{SGW} for a range of acoustic material parameters of the fluid and for zero viscosity (inviscid fluids). b) Contour lines of the SGW phase velocity V_{SGW} for a range of visco–acoustic parameters of the fluid. c) Contour lines of the logarithm of the quality factor of the SGW Q_{SGW} for a range of visco–acoustic parameters of the fluid. The abscissa of b) and c) is a linear relationship between $log_{10}\left(\rho^f\right)$ and $log_{10}\left(K^f\right)$ that approximately connects the material parameters ρ^f and K^f of water, oil and hydrocarbon gas and is shown in a) as a gray line. In a) and b) V_{SGW} is divided by the P–wave phase velocity in the elastic rock V_P^s and by the P–wave phase velocity in the visco–acoustic fluid V_P^f (V_C for the inviscid case in a). Material parameters for the solid, the crack thickness h and the central frequency of the waves f_0 are constant in all subfigures. Material parameters of the inviscid (acoustic) and visco–acoustic fluids used in this study (water, oil and hydrocarbon gas) are indicated as full and open circles, respectively.

Type of fluid	Water	Oil	Gas
Crack stiffness $C = \left(2K^f L\right)/\left(\mu h\right)$	122.2	72.2	1.22
Viscous damping loss $F = \left(23\eta L\right)/\left(\rho^f h^2 V_P^s\right)$	5.8×10^{-4}	71.1×10^{-4}	5.1×10^{-4}
Phase velocity of SGW for viscous fluids V_{SGW} [m/s]	586.2	608.7	459.8
Ratio V_{SGW}/V_P^s	0.257	0.267	0.202
Ratio V_{SGW}/V_P^f	0.395	0.478	0.980
Phase velocity of SGW for inviscid fluids $V_{SGW}^{\text{inviscid}}$ [m/s]	586.7	610.7	459.9
Ratio $V_{SGW}^{\text{inviscid}}/V_P^s$	0.257	0.268	0.202
Ratio $V_{SGW}^{\text{inviscid}}/V_C$	0.396	0.479	0.981
Quality factor of SGW Q_{SGW}	527.8	144.3	1189.2

Table 3.2: Properties of the crack and of the SGW for different fluids that fill the crack. Superscripts s and f denote properties of the elastic rock (solid) and of the fluid, respectively. All properties are calculated for the particular values for the crack geometry, the material properties of the solid and the central frequency of the external force used in this study. The phase velocity of the SGW is calculated using the solutions of Ferrazzini and Aki (1987) and Korneev (2008) for inviscid and viscous fluids, respectively.

3.4. Numerical Method

The algorithm used for numerical simulations is an extended version of the algorithm presented and benchmarked in Frehner *et al.* (2008). It employs the finite element method (FEM) (Hughes, 1987; Bathe, 1996; Zienkiewicz and Taylor, 2000) for discretization of the spatial derivatives in Equation 3.10. The particular finite element used is a 7–node isoparametric triangular element with biquadratic continuous interpolation functions (Hughes, 1987; Bathe, 1996; Zienkiewicz and Taylor, 2000). The unstructured numerical grid is generated by the software Triangle (Shewchuk, 1996, 2002). It is generated in such a way that interfaces between different media coincide with element boundaries of the finite element grid. Figure 3.3 shows three subfigures on different scales of the same finite element grid that discretizes the model setup with the elliptical crack. The finite element algorithm used comprises the Galerkin weighted residual method (Zienkiewicz and Taylor, 2000), lumped mass matrix (Bathe, 1996; Cohen, 2002) and Gauss–Legendre

quadrature on seven integration points (Zienkiewicz and Taylor, 2000). Equation 3.10, discretized in space with the FEM takes the following form:

$$\mathbf{M}_L\ddot{\mathbf{u}} + \mathbf{C}\dot{\mathbf{u}} + \mathbf{K}\mathbf{u} = 0, \tag{3.14}$$

where $\mathbf{M}_L$, $\mathbf{C}$ and $\mathbf{K}$ are the lumped mass matrix, the damping matrix and the stiffness matrix, respectively. The displacement vector $\mathbf{u}$ contains the unknown displacements u_x and u_y at all discrete positions in the finite element grid. Note that the symbol ˜ has been removed from $\mathbf{u}$ compared to Equation 3.10 because it is now discretized in space (i.e. $\mathbf{u}$ contains only the values at numerical nodes). Time derivatives are discretized with an implicit version of the Newmark algorithm (Zienkiewicz and Taylor, 2000). It is a predictor–corrector algorithm based on a finite difference formulation.

- Predictor:

$$
\begin{aligned}
\ddot{\mathbf{u}}_{j+1}^{\mathrm{prediction}} &= -\frac{1}{\beta\Delta t^2}\mathbf{u}_j - \frac{1}{\beta\Delta t}\dot{\mathbf{u}}_j - \frac{1-2\beta}{2\beta}\ddot{\mathbf{u}}_j \\
\dot{\mathbf{u}}_{j+1}^{\mathrm{prediction}} &= -\frac{\gamma}{\beta\Delta t}\mathbf{u}_j + \left(1 - \frac{\gamma}{\beta}\right)\dot{\mathbf{u}}_j + \left(1 - \frac{\gamma}{2\beta}\right)\Delta t\ddot{\mathbf{u}}_j
\end{aligned}
\tag{3.15}
$$

- Solution:

$$\mathbf{u}_{j+1} = -\left(\frac{1}{\beta\Delta t^2}\mathbf{M}_L + \frac{\gamma}{\beta\Delta t}\mathbf{C} + \mathbf{K}\right)^{-1}\left(\mathbf{C}\dot{\mathbf{u}}_{j+1}^{\mathrm{prediction}} + \mathbf{M}_L\ddot{\mathbf{u}}_{j+1}^{\mathrm{prediction}}\right) \tag{3.16}$$

- Corrector:

$$
\begin{aligned}
\ddot{\mathbf{u}}_{j+1} &= \ddot{\mathbf{u}}_{j+1}^{\mathrm{prediction}} + \frac{1}{\beta\Delta t^2}\mathbf{u}_{j+1} \\
\dot{\mathbf{u}}_{j+1} &= \dot{\mathbf{u}}_{j+1}^{\mathrm{prediction}} + \frac{\gamma}{\beta\Delta t}\mathbf{u}_{j+1}
\end{aligned}
\tag{3.17}
$$

Subscript j is the index of any discrete time interval and Δt is the time increment. For the two Newmark parameters β and γ the optimal values of $1/4$ and $1/2$ are chosen (Newmark, 1959; Bathe, 1996). Because the time integration method is implicit, no stability criterion for the time increment has to be fulfilled and the time increment Δt can be chosen independently from the spatial resolution. This allows having a very fine spatial resolution (Figure 3.3) without the need of a very small time increment. The time

increment is chosen in such a way that a P–wave in the elastic rock travels the distance $2L$ in 2000 time steps.
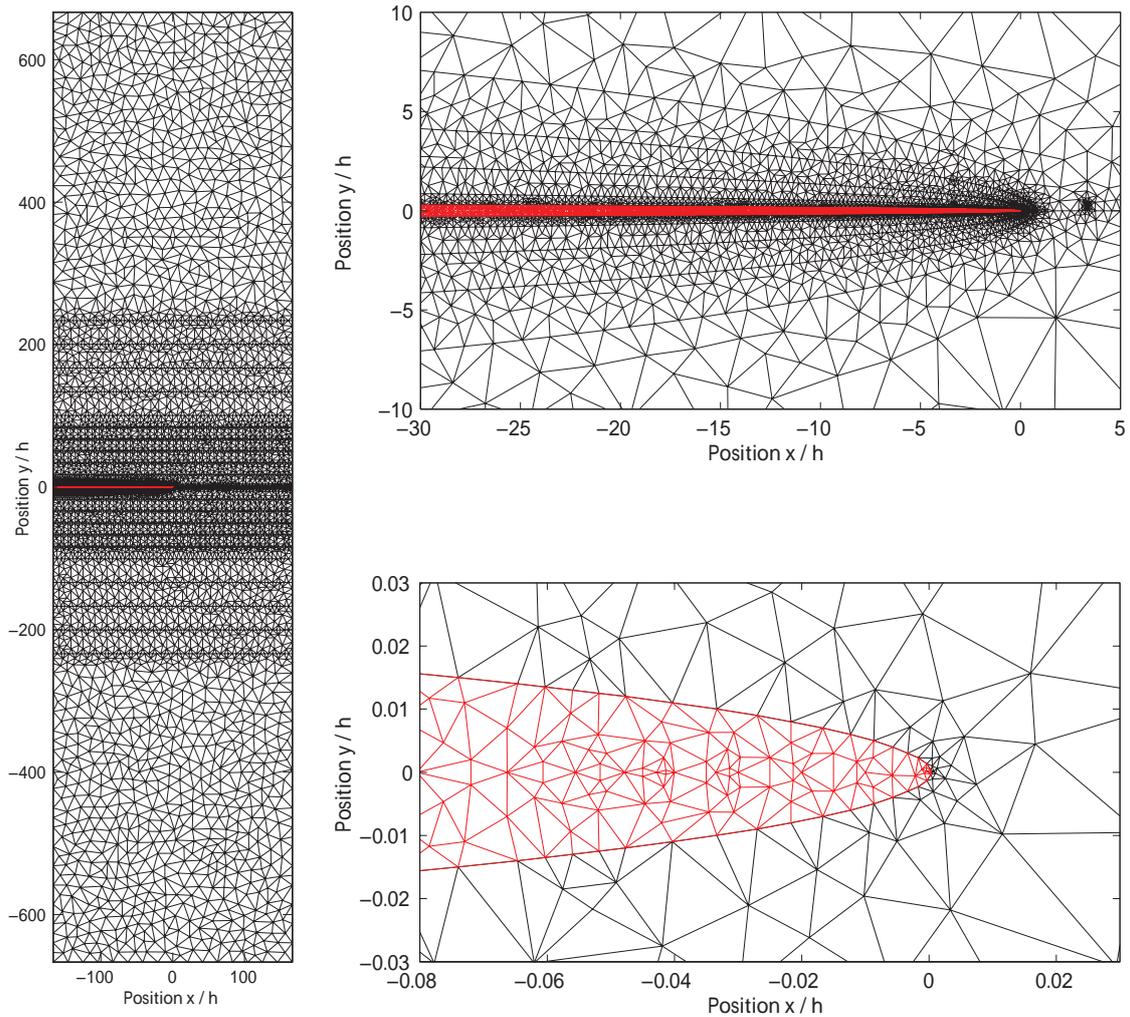
**Figure 3.3:** Three subfigures on different scales of the same numerical finite element grid discretizing the model with the elliptical crack (second model in Figure 3.1). Red elements have material parameters of the visco–acoustic fluid. Black elements have material parameters of the elastic rock. The spatial resolution of the grid varies strongly, being very fine inside and close to the crack.

3.4.1. Benchmark of the numerical code

An earlier version of the numerical code was benchmarked in Frehner *et al.* (2008) for a different geometrical setup comprising fully elastic and acoustic media but no visco–acoustic media. Figure 3.4 shows the phase velocity dispersion curves of a SGW calculated for a straight crack and for the model parameters displayed in the figure. Analytical solutions are taken from Ferrazzini and Aki (1987) and Korneev (2008) for acoustic (inviscid) and visco–acoustic fluids, respectively. Five numerical simulations were performed with different central frequencies of the external source. The model consisting of a straight crack (first model in Figure 3.1) is used for comparison with the analytical solutions. The velocity of the SGW calculated from the time shift between measurements at the two receiver lines (Figure 3.1) is plotted on top of the analytical solutions. These numerically calculated velocities agree well with the analytic solutions.
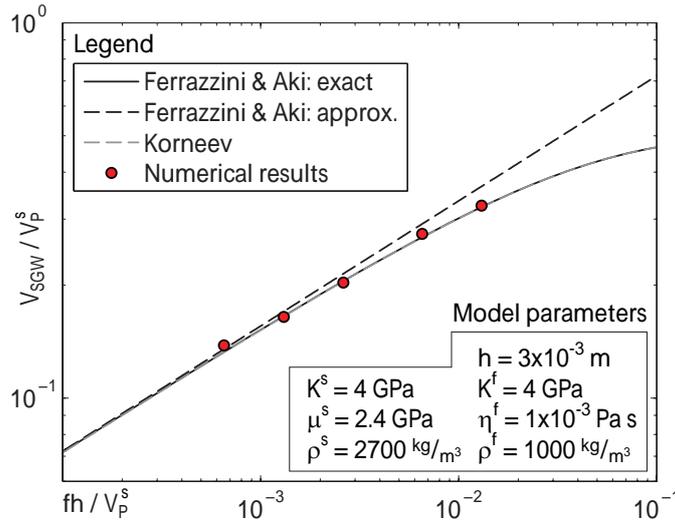
Figure 3.4: Phase velocity dispersion curve for a SGW propagating along a straight crack in a system with the given model parameters. Ferrazzini and Aki (1987) provide an exact (their equation 14b) and an approximate (their equation 16, also equation 1 in Korneev (2008)) solution for an infinite crack filled with an inviscid (acoustic) fluid. Korneev (2008) provides a solution for a crack filled with a visco–acoustic fluid (his equation 40). Numerical results are derived from five simulations using the first model in Figure 3.1 with different central frequencies f_0 in the external source. The phase velocity of the SGW V_{SGW} is normalized with the phase velocity of a P–wave in the rock V_P^s. The frequency f is normalized with V_P^s/h.

3.5. Numerical Results

In the following, results of the propagation, reflection and scattering of SGWs are presented that are derived from different numerical simulations.

3.5.1. Radiation of P– and S–waves from the crack tip

The SGW is bound to the crack and can not propagate further when the crack ends. It must be (partly) reflected at the crack tip. Figure 3.5 shows the snapshots of a simulation of a SGW propagating from left to right along an elliptical crack (second model in Figure 3.1) filled with viscous water. Panels a) and b) show the incident SGW, which is almost unaffected by the presence of the crack tip. Because the crack thins towards the crack tip due to its elliptical shape, the SGW slows down towards the crack tip. Therefore, even though the SGW has not reached the crack tip yet, it is slightly deformed at its front. The regular spacing of the logarithmically plotted contour lines demonstrates the exponential decay of the amplitude away from the crack (Ferrazzini and Aki, 1987). The amplitude decays more than one order of magnitude within one wavelength of the SGW. Panels c) and d) show the SGW as it starts being reflected from the crack tip. Also, a part of the wave energy is transferred to the surrounding elastic rock in the form of P– and S–waves. The P–wave is visible in the upper panel while the S–wave is visible in the lower panel. The difference in propagation distance between the P– and S–wave due to the different wave velocities is clearly visible. In panels e) and f) the incident and reflected wave trains of the SGW interfere destructively and the amplitude close to the crack tip is relatively small. Also, a second pulse of P– and S–waves is radiated into the surrounding elastic rock. The first S–wave pulse is still visible in the lower panel but its amplitude decreased due to geometrical spreading. Panels g) and h) show the final phase of the reflection process of the SGW. The SGW now propagates to the left away from the crack tip. Interestingly, the P– and S–waves radiated away from the crack tip form an almost point symmetric radiation pattern around the crack tip, which leads to the interpretation that the crack tip acts like a point diffractor for the SGW. This interpretation can be understood because the width of the crack and therefore the size of the crack tip are orders of magnitudes smaller than the wavelength of the SGW. In

all panels the interference of the incoming and reflected SGW trains leads to nodes (zero amplitude) and anti–nodes (maximum amplitudes). One of the nodes is exactly at the crack tip. Therefore, the reflection pattern of the SGW can be compared to a reflection of a one–dimensional wave propagating in a medium with lower impedance at the interface to a medium with higher impedance.
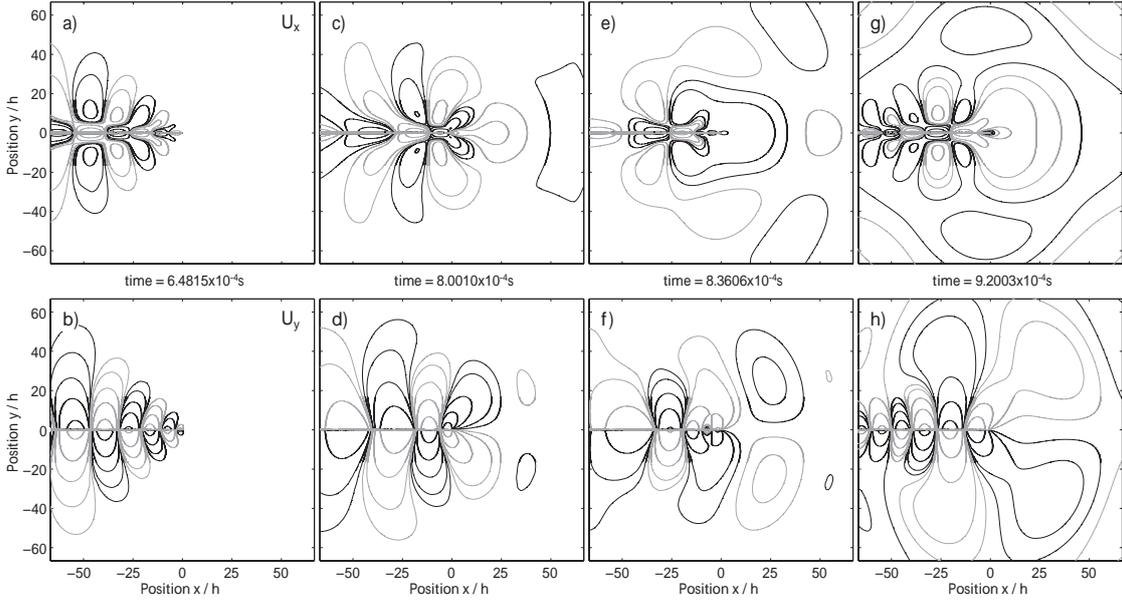
Figure 3.5: Snapshots of the 2D displacement field of a simulation of a SGW propagating along an elliptical crack (second model in Figure 3.1) filled with viscous water. Shown in black are contour lines at the values 1×10^{-8} m, 3×10^{-8} m, 1×10^{-7} m, 3×10^{-7} m and 1×10^{-6} m. Shown in gray are contour lines at the values -1×10^{-8} m, -3×10^{-8} m, -1×10^{-7} m, -3×10^{-7} m and -1×10^{-6} m. Upper panels show the x–component of the displacement field u_x. Lower panels show the y–component of the displacement field u_y. Panels from left to right represent progressive points in time with the time indicated between the panels. Axis labels are only given in the left and lower panels but are valid for all panels. The SGW is partially reflected at the crack tip and elastic P– and S–waves are emitted from the crack tip into the surrounding rock.

Figure 3.6 shows snapshots of a simulation of a SGW propagating from left to right along a straight crack with a flat crack tip (third model in Figure 3.1) filled with viscous water. Unlike in Figure 3.5, the wave velocity of the SGW is constant due to the constant thickness of the crack. Therefore, the individual snapshots in Figure 3.6 are not displayed for the same points in time as in Figure 5 but it was tried to display the same stages of the reflection process as in Figure 3.5 to make the figures comparable. The reflection pattern

of the SGW at the flat crack tip is very similar to the one at the elliptical crack tip. However, the nodes and anti–nodes along the crack are further apart because the SGW does not slow down towards the crack tip. Similar to the elliptical crack tip the P– and S–waves radiated away from the flat crack tip form an almost point symmetric radiation pattern at the end of the reflection process. However, a major difference between the two geometrical setups is the amplitudes of these P– and S–waves in the elastic solid, the amplitudes being considerably higher for a flat crack tip.
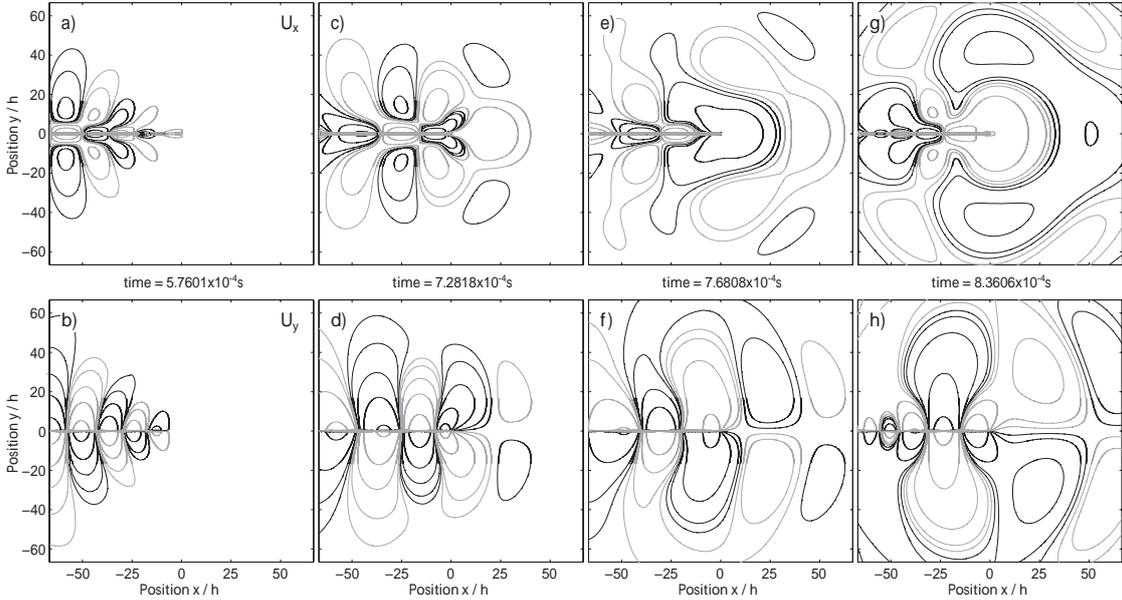
Figure 3.6: Same as Figure 3.5 but for a rectangular crack with a flat crack tip (third model in Figure 3.1). Note that the time of the snapshots is not the same as in Figure 3.5 because the SGW travels with a slightly different velocity.

3.5.2. Reflection of the SGW at the crack tip

As seen above, not all of the wave energy of the SGW is reflected at the crack tip but a part is radiated into the surrounding rock in the form of P– and S–waves. Figure 3.7 displays the displacement–time signal at two receivers on receiver line 1 (Figure 3.1), one inside and one outside the crack, for a simulation of a SGW being reflected at the tip of an elliptical crack (second model in Figure 3.1) filled with viscous water. The incident and reflected SGWs are well separated from each other in time. To quantify the reflected part

of the SGW Figure 3.8 shows the reflection coefficient R for different model setups and for different fluids filling the crack. Values of R are calculated from the displacement–time signals at receivers on receiver line 1 (Figure 3.1), like the example shown in Figure 3.7. For each simulation two values for R are calculated, one at receivers inside the crack in the visco–acoustic fluid and one for receivers outside the crack in the elastic rock. Values labeled "oil with gas cap, elliptical crack tip" are discussed later. Values plotted for material properties of water (values to the right of Figure 3.8) correspond to the two simulations shown in Figure 3.5 and Figure 3.6.
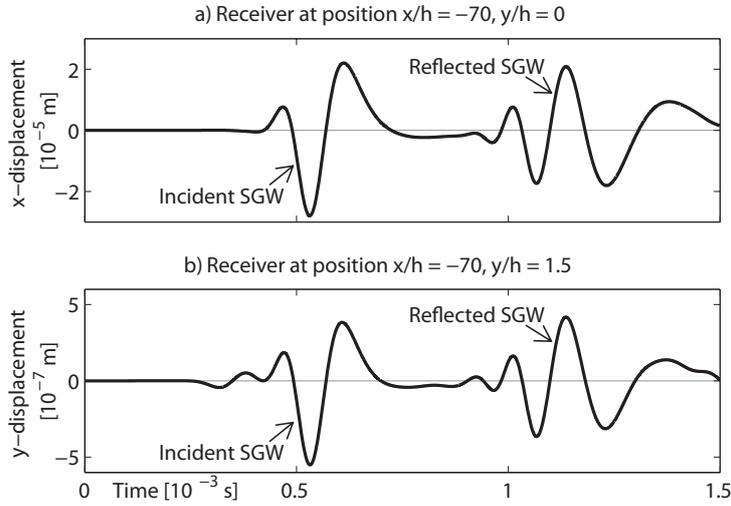
Figure 3.7: a) Displacement–time signal in x–direction at a receiver inside the crack on receiver line 1 (Figure 3.1). b) Displacement–time signal in y–direction at a receiver outside the crack on receiver line 1. Both traces are obtained from a simulation of a SGW propagating along an elliptical crack (second model in Figure 3.1) filled with viscous water. Axis labels for the time–axis are only given in the lower subfigure but are valid for both subfigures.

Around 77 % of the SGW is reflected at the elliptical crack tip and only around 43 % is reflected at the flat crack tip. This is remarkable because the size of the crack tip is orders of magnitude smaller than the wavelength of the SGW but still has a big impact. The difference in the reflection coefficient also explains the amplitude difference of the radiated P– and S–waves shown in Figure 3.5 and Figure 3.6. What is not reflected is radiated into the surrounding rock. Therefore, a higher reflection coefficient (elliptical crack) leads to smaller amplitudes of the radiated P– and S–waves. For different fluids filling the elliptical crack the reflection coefficient is also different. Hydrocarbon gas leads

to the highest reflection coefficient of almost 100 %. This also means that from a crack filled with hydrocarbon gas only very small amplitude P– and S–waves are radiated when the SGW is reflected at the crack tip. A SGW propagates both in the fluid that fills the crack and in the rock surrounding the crack. It is therefore unclear how to calculate the impedance for a SGW. However, the high reflection coefficient for a crack filled with hydrocarbon gas can be qualitatively understood by considering the impedance of the P–wave in the fluid ($\sqrt{K^f \rho^f}$), which is much smaller for hydrocarbon gas than for water and oil. Therefore, the impedance contrast to the surrounding rock is much bigger, which leads to a high reflection coefficient.
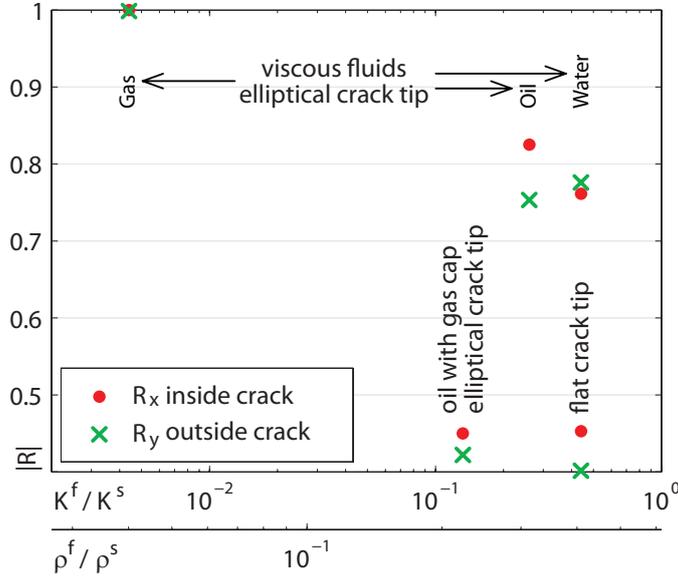
Figure 3.8: Absolute value of the reflection coefficient $|R|$ of a SGW that is reflected at the tip of a crack. The abscissa is the same as in Figure 3.2b) and c). R_x is calculated from the displacement–time signals in x–direction of eight receivers inside the crack on receiver line 1 at position $y/h = 0 - 0.35$. R_y is calculated from the displacement–time signals in y–direction of six receivers outside the crack on receiver line 1 at position $y/h = 0.45 - 5.5$. Values labeled "*viscous fluids, elliptical crack tip*" are derived from simulations of an elliptical crack (second model in Figure 3.1) fully saturated with the corresponding viscous fluid. Values labeled "*flat crack tip*" are derived from a simulation of a rectangular crack with a flat crack tip (third model in Figure 3.1) fully saturated with viscous water. Values labeled "*oil with gas cap, elliptical crack tip*" are derived from a simulation of an elliptical crack (second model in Figure 3.1) partially saturated with viscous oil and having a small gas cap at the crack tip. These values are plotted at $\left(K^{\text{Oil}} + K^{\text{Gas}}\right)/2$. All values of $|R|$ are corrected for the intrinsic attenuation due to viscous damping in the fluids.
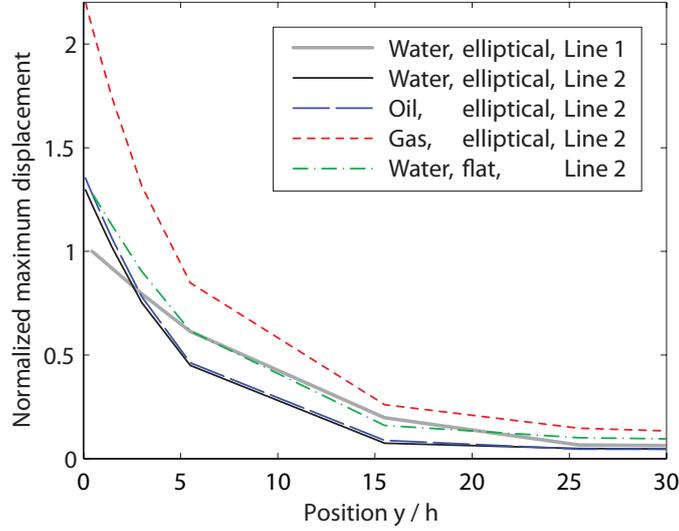
Figure 3.9: Maximum absolute particle displacement along receiver lines 1 and 2 (Figure 3.1) measured during the course of four different simulations. Three simulations consist of an elliptical crack filled with three different viscous fluids. The fourth simulation consists of a rectangular crack ending at a flat crack tip filled with viscous water. Maximum absolute particle displacement along receiver line 1 is only shown for the elliptical crack filled with water (solid gray line) because it is almost identical for all simulations. All values of one simulation are normalized with the maximum absolute particle displacement at the crack interface at receiver line 1.

Due to the interference between incident and reflected SGWs the amplitudes add up close to the crack tip. Figure 3.9 shows this effect and how the amplitude decays away from the crack along receiver line 2 (Figure 3.1) for different model setups and different fluids filling the crack. The amplitude distribution shows the same exponential decay as discussed in Ferrazzini and Aki (1987). As a reference (solid gray line) the amplitude decay along receiver line 1 for an elliptical crack filled with water is also given in Figure 3.9. For this case the wavelength of the SGW is around 40 times the crack thickness h. At this distance away from the crack the amplitude decay is more than an order of magnitude. The amplitude at the crack interface at receiver line 2 for a water and oil filled crack is increased by about 30 %. Also the two different crack geometries (elliptical and rectangular crack) that are filled with water do not influence this factor significantly. The same amplitude for a crack filled with hydrocarbon gas is increased by about 120 %. This is remarkable because for a reflection coefficient of 100 % (Figure 3.8) a maximal increase in amplitude close to the crack tip of 100 % is expected. However, the wave

velocity of the SGW also decreases towards the crack tip due to the elliptical shape of the crack. This lets the amplitude of the SGW further increase, which adds up to the maximal 100 % increase in amplitude due to the reflection process. For all cases shown in Figure 3.9, even though the amplitude at the crack interface is increased, the decay away from the crack happens within a relatively short distance. For cracks filled with water or oil the amplitude along receiver line 2 is even smaller than along receiver line 1 for distances greater than 5 times the crack thickness.

3.5.3. Advanced model setups

The model setup consisting of an elliptical crack (second model in Figure 3.1) is used for simulating a partially filled crack. The crack is filled with viscous oil and has a small cap at the crack tip filled with hydrocarbon gas. The gas cap extends from $x/h = -31.8$ to $x/h = 0$. Figure 3.10 shows the snapshots of the displacement field in x– and y–direction after the SGW is reflected at the crack tip. A major part of the SGW is reflected already at the oil–gas contact line and only a small–amplitude SGW propagates further along the crack where it is reflected at the crack tip. This multiple reflection leads to the complex reflection pattern in Figure 3.10. One major difference to the crack filled only with oil (almost identical to crack filled only by water, Figure 3.5) is the amplitude and radiation pattern of the P– and S–waves that are radiated away from the crack tip when the SGW is reflected. The radiation pattern is much more forward directed towards the propagation direction of the incident SGW, compared to an almost point–symmetric radiation pattern for the fully saturated crack (Figure 3.5). Also, the amplitudes of the radiated P– and S–waves are much larger. Figure 3.8 shows the reflection coefficient for both cases. For the crack fully saturated with oil the reflection coefficient is about 78 %. It is reduced to about 43 % when the gas cap is present. The larger amplitudes of the radiated P– and S–waves also mean that less of the energy of the SGW is reflected compared to the fully saturated crack.
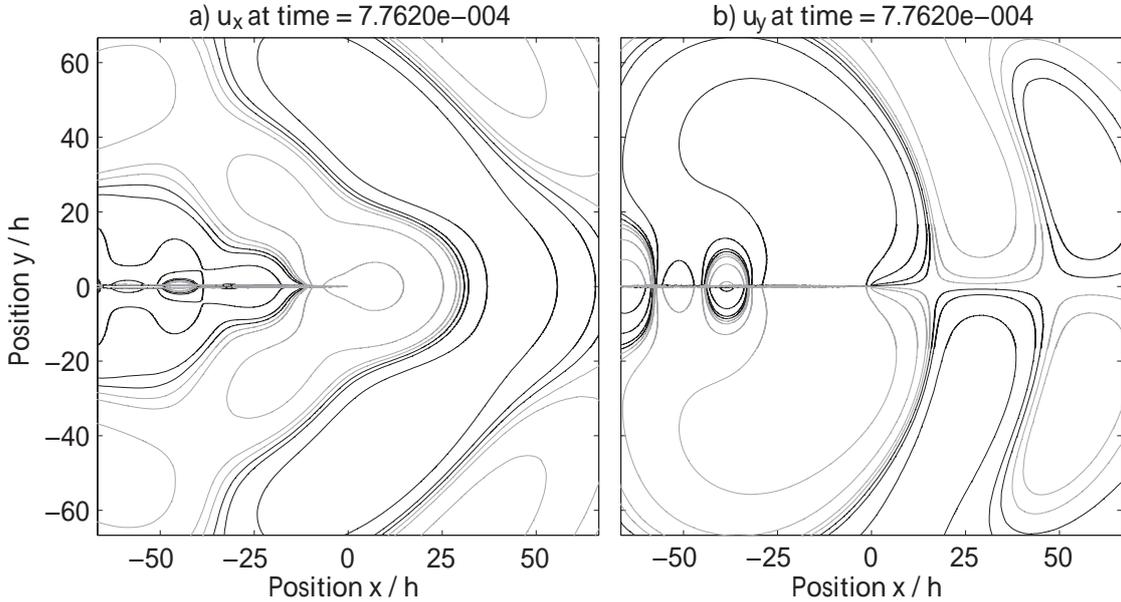
Figure 3.10: Snapshots of the x– (a) and y–component (b) of the 2D displacement field of a simulation of a SGW propagating along an elliptical crack (second model in Figure 3.1). The crack is filled with viscous oil and has a small gas cap at the crack tip. Contour lines are the same as in Figure 3.5. Axis labels for the ordinate are only given in the left subfigure but are valid for both subfigures.

Individual isolated cracks are relatively unusual in nature. More common are swarms of similarly oriented cracks or two or more families of cracks whose orientations intersect. Figure 3.11 shows two snapshots at different points in time of a simulation of two intersecting cracks. The first crack, in which the SGW is initiated, has an aspect ratio of 333. The second crack has an aspect ratio of 95. The first snapshot (Figure 3.11a) is taken before the SGW reaches the intersection point of the two cracks. Two SGW trains propagated away from the external source. The left wave train is already reflected at the left crack tip and now both wave trains are propagating towards the intersection point to the right. Also visible are the P– and S–waves that propagate in the surrounding rock away from the external source and are scattered by the cracks. The second snapshot (Figure 3.11b) is taken after the first SGW train passed the intersection point of the two cracks. Only a part of the SGW continues propagating straight ahead on the first crack. A part is reflected at the intersection point and interferes with the second SGW train on the first crack. A considerable part of the SGW makes a sharp turn and propagates

along the two branches of the second crack. Also, P– and S–waves are radiated away from the intersection point into the surrounding rock.
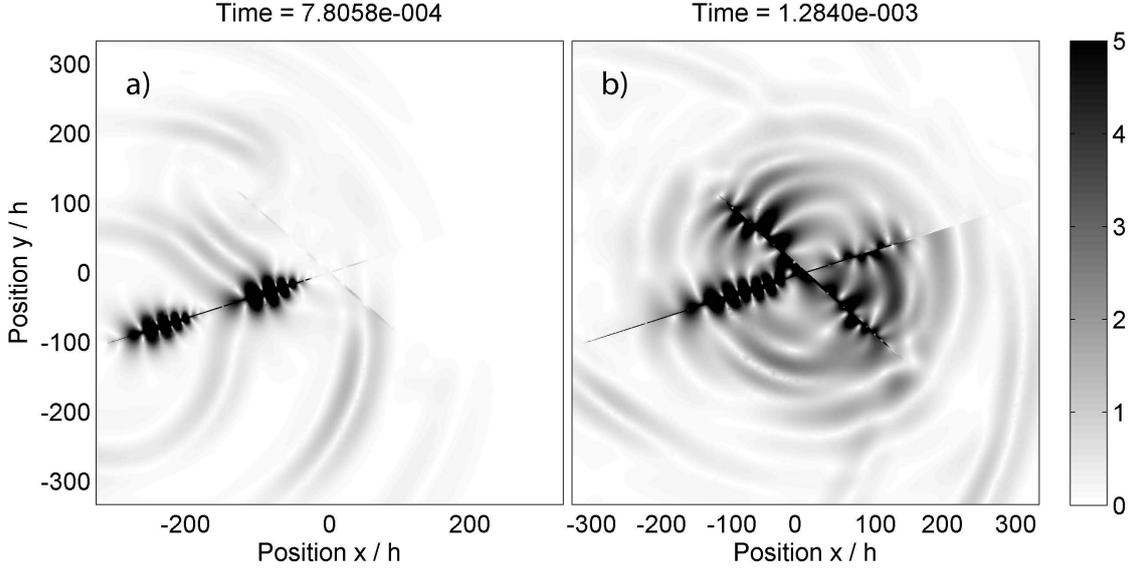
Figure 3.11: Snapshots of the 2D displacement field at two different points in time (a and b) of a simulation of a SGW propagating along an elliptical crack that is intersected by a second elliptical crack. The displayed value is the normalized absolute particle displacement $10^6\sqrt{u_x^2 + u_y^2}$. The cracks are filled with viscous water. Axis labels for the ordinate are only given in the left subfigure but are valid for both subfigures.

3.6. Discussion

Models of SGWs propagating along fluid–filled cracks on various scales are used to explain the occurrence of long period volcanic tremor (Aki *et al.*, 1977; Chouet, 1988, 1996). The magma chamber as a whole or hydro–fractures around the volcanic conduit may be considered as the wave guide where a SGW propagates back and forth, which results in a characteristic frequency. The way this long period signal is transmitted to recording stations at the Earth's surface remained unclear. The present study shows how P– and S–waves are emitted into the surrounding rock when a SGW is reflected at the crack tip. The emission of elastic body waves makes it possible to detect the presence of a SGW even in distances away from the crack where the amplitude of the SGW itself is too

small to be measured. The orientation of fully saturated cracks (or magma chambers) might not be determinable from measurements of volcanic tremor due to the almost point–symmetric radiation pattern, but it might be possible for cracks containing a gas cap. Which model is more realistic in nature is still to be determined. The viscosity of magma is considerably larger than that of the fluids in this study. Even though the reflection coefficient of a SGW at the tip of a crack filled with magma may be high, the SGW is expected to be attenuated relatively fast. This means that a single SGW can not propagate back and forth the crack many times and produce a continuous long period volcanic tremor. For this, a continuous excitation of SGWs would be necessary.

The presented numerical models deal with a multiscale wave propagation phenomenon. Although highly resolved, the numerical setup is still rather simple, consisting of only one single crack. One approach toward more realistic model setups was shown in the present study by modeling two highly resolved intersecting cracks. Another approach is for example a model of many cracks (Saenger and Shapiro, 2002; Saenger *et al.*, 2004). The primary investigation target of such models is to determine effective bulk rock properties. However, the high spatial resolution that is needed for accurately modeling SGWs is lacking in these models. For further insight into the significance of SGWs in a realistic fractured rock both end member modeling approaches have to be brought together to have a high–resolution model of a strongly fractured rock.

Using the FDM, it is not straightforward to discretize an elliptical crack with the rectangular numerical grid. Staircase–like discretization leads to numerical inaccuracies (Frehner *et al.*, 2008). A logical choice for the crack geometry is a straight crack with a flat crack tip (Chouet, 1986; Groenenboom and Falk, 2000). Conversely, the FEM can handle both crack geometries with ease because it uses an unstructured numerical mesh. This difference is critical because the two different crack geometries have a major influence on the reflection coefficient of SGWs and on the amplitude of the radiated P– and S–waves. The sharp edges at the tip of the straight crack scatter SGWs much more than the smooth elliptical crack tip. The question remains which crack geometry is more realistic for natural cracks. Supposedly, a straight crack with flat crack tips is not the most realistic model. Further investigations including rugose crack surfaces or cracks not being straight can also be addressed simply with the FEM approach.

3.7. Conclusions

The propagation of SGWs along a thin crack is a multiscale problem where the different scales need to be resolved in detail. The FEM is a suitable numerical method for simulating such problems. The unstructured numerical grid allows having a fine resolution where it is needed without the need of a fine resolution elsewhere in the numerical domain. Also, the unstructured grid allows resolving complex geometries accurately without introducing staircase–like discretization. The very fine spatial resolution would lead to a very small explicit time increment and therefore to long calculation times. The implicit time integration is a suitable alternative for the problem studied here.

SGWs propagate along cracks and are partly reflected at the crack tip. The interference between incident and reflected SGWs leads to nodes (zero amplitude) and anti–nodes (maximum amplitude) with one node exactly at the crack tip. A relatively short distance away from the crack the SGW amplitude is too small to be detected due to the exponential decay away from the crack. This is true even during the reflection process when the SGW amplitude is increased at anti–nodes (Figure 3.9).

The reflection coefficient of the SGW at the crack tip depends on the fluid properties in the crack and on the crack geometry (Figure 3.8). An elliptical crack having a round tip exhibits a significantly higher reflection coefficient than a rectangular crack having sharp corners at the tip. Elliptical fractures filled with gas, oil or water exhibit high reflection coefficients between about 75 % and almost 100 % (Figure 3.8).

The part of the SGW that is not reflected at the crack tip is emitted into the surrounding elastic rock in the form of P– and S–waves (Figure 3.5 and Figure 3.6). This makes the detection of SGW–related signals possible even away from the crack where the SGW itself can not be detected. The radiation pattern of these body waves is almost point–symmetric around the crack tip for a fully saturated crack. In the presence of a small gas cap at the crack tip the radiation pattern is predominantly directed in the propagation direction of the incident SGW (Figure 3.10).

Acknowledgements

References

Achenbach J. D., 1973: **Wave propagation in elastic solids**, Volume 16 of North-Holland series in Applied Mathematics and Mechanics, North-Holland Publishing Company, Amsterdam, ISBN 0-7204-2367-8

Aki K. and Richards P. G., 2002: **Quantitative seismology**, 2nd Edition, University Science Books, Sausalito, ISBN 0-9357-0296-2

Aki K., Fehler M. and Das S., 1977: **Source mechanism of volcanic tremor: Fluid-driven crack models and their application to the 1963 Kilauea eruption**, Journal of Volcanology and Geothermal Research 2, 259–287

Ashour A. S., 2000: **Wave motion in a viscous fluid-filled fracture**, International Journal of Engineering Science 38, 505–515

Bathe K.-J., 1996: **Finite element procedures**, 2nd Edition, Prentice Hall, Englewood Cliffs, ISBN 0-1330-1458-4

Biot M. A., 1962: **Mechanics of deformation and acoustic propagation in porous media**, Journal of Applied Physics 33, 1482–1498

Bourbie T., Coussy O. and Zinszner B., 1987: **Acoustics of porous media**, Editions Technip, Paris, ISBN 2-7108-0516-2

Carcione J. M., 2001: **Wave fields in real media: Wave propagation in anisotropic, anelastic and porous media**, Volume 31 of Handbook of Geophysical Exploration, Elsevier Science Ltd., Amsterdam, ISBN 0-0804-3929-2

Carcione J. M. and Helle H. B., 2004: **The physics and simulation of wave propagation at the ocean bottom**, Geophysics 69, 825–839, doi:10.1190/1.1759469

Chen Z. Y., Steeb H. and Diebels S., 2008: **A new hybrid velocity integration method applied to elastic wave propagation**, International Journal for Numerical Methods in Engeneering 74, 56–79, doi:10.1002/nme.2167

Chouet B., 1986: **Dynamics of a fluid-driven crack in three dimensions by the finite-difference method**, Journal of Geophysical Research 91, 13967–13992

Chouet B., 1988: **Resonance of a fluid-driven crack: Radiation properties and implications for the source of long-period events and harmonic tremor**, Journal of Geophysical Research 93, 4375–4400

Chouet B. A., 1996: **Long-period volcano seismicity: Its source and use in eruption forecasting**, Nature 380, 309–316

Cohen G. C., 2002: **Higher-order numerical methods for transient wave equations**, Series in scientific computation, Springer Verlag, Berlin, ISBN 3-5404-1598-X

Dvorkin J., Mavko G. and Nur A., 1995: **Squirt flow in fully saturated rocks**, Geophysics 60, 97–107

Faoro I., Niemeijer A., Marone C. and Elsworth D., 2009: **Influence of shear and deviatoric stress on the evolution of permeability in fractured rock**, Journal of Geophysical Research 114, B01201, doi:10.1029/2007JB005372

Ferrazzini V. and Aki K., 1987: **Slow waves trapped in a fluid-filled infinite crack: Implication for volcanic tremor**, Journal of Geophysical Research 92, 9215–9223

Frehner M. and Schmalholz S. M., 2009: **Finite element simulations of Stoneley guided wave reflection and scattering at the tips of fluid-filled fractures**, Geophysics Submitted

Frehner M., Schmalholz S. M., Saenger E. H. and Steeb H., 2008: **Comparison of finite difference and finite element methods for simulating two-dimensional scattering of elastic waves**, Physics of the Earth and Planetary Interiors 171, 112–121, doi:10.1016/j.pepi.2008.07.003

Groenenboom J. and Falk J., 2000: **Scattering by hydraulic fractures: Finite-difference modeling and laboratory data**, Geophysics 65, 612–622

Higham N. J., 1996: **Accuracy and stability of numerical algorithms**, Society for Industrial and Applied Mathematics, Philadelphia, ISBN 0-8987-1355-2

Hudson J. A., 1980: **Overall properties of a cracked solid**, Mathematical Proceedings of the Cambridge Philosophical Society 88, 371–384

Hudson J. A., 1981: **Wave speeds and attenuation of elastic-waves in material containing cracks**, Geophysical Journal of the Royal Astronomical Society 64, 133–150

Hughes T. J. R., 1987: **The finite element method: Linear static and dynamic finite element analysis**, Dover Publications, Mineola, ISBN 0-4864-1181-8

Ionov A. M., 2007: **Stoneley wave generation by an incident P-wave propagating in the surrounding formation across a horizontal fluid-filled fracture**, Geophysical Prospecting 55, 71–82

Korneev V., 2008: **Slow waves in fractures filled with viscous fluid**, Geophysics 73, N1–N7, doi:10.1190/1.2802174

Krüger O. S., Saenger E. H. and Shapiro S. A., 2005: **Scattering and diffraction by a single crack: An accuracy analysis of the rotated staggered grid**, Geophysical Journal International 162, 25–31, doi:10.1111/j.1365-246X.2005.02647.x

Käser M. and Dumbser M., 2008: **A highly accurate discontinuous Galerkin method for complex interfaces between solids and moving fluids**, Geophysics 73, T23–T35, doi:10.1190/1.2870081

Lindsay R. B., 1960: **Mechanical radiation**, International series in pure and applied physics, McGraw-Hill, New York, ISBN 0-0703-7844-0

Love A. E. H., 1944: **A treatise on the mathematical theory of elasticity**, 4th Edition, Dover books on physics and chemistry, Dover Publications, New York, ISBN 0-4866-0174-9

Mavko G. and Jizba D., 1991: **Estimating grain-scale fluid effects on velocity dispersion in rocks**, Geophysics 56, 1940–1949

Mavko G., Mukerji T. and Dvorkin J., 2003: **The rock physics handbook: Tools for seismic analysis in porous media**, Cambridge University Press, Cambridge, ISBN 0-5215-4344-4

Newmark N. M., 1959: **A method of computation for structural dynamics**, Journal of the Engeneering Mechanics Division 85, 67–94

Pujol J. A., 2003: **Elastic wave propagation and generation in seismology**, Cambridge University Press, Cambridge

Saenger E. H. and Shapiro S. A., 2002: **Effective velocities in fractured media: a numerical study using the rotated staggered finite-difference grid**, Geophysical Prospecting 50, 183–194

Saenger E. H., Gold N. and Shapiro S. A., 2000: **Modeling the propagation of elastic waves using a modified finite-difference grid**, Wave Motion 31, 77–92

Saenger E. H., Krüger O. S. and Shapiro S. A., 2004: **Effective elastic properties of randomly fractured soils: 3D numerical experiments**, Geophysical Prospecting 52, 183–195

Saenger E. H., Shapiro S. A. and Keehm Y., 2005: **Seismic effects of viscous Biot-coupling: Finite difference simulations on micro-scale**, Geophysical Research Letters 32, doi:10.1029/2005GL023222, l14310

Shames I. H. and Cozzarelli F. A., 1997: **Elastic and inelastic stress analysis**, revised printing Edition, Taylor and Francis, Washington

Shewchuk J. R., 1996: **Triangle: Engeneering a 2D quality mesh generator and delaunay triangulator**, in Applied Computational Geometry: Towards Geometric Engeneering, Volume 1148 of Lecture Notes in Computer Science, Springer Verlag,

Berlin, pages 203–222, (From the First ACM Workshop on Applied Computational Geometry)

Shewchuk J. R., 2002: **Delaunay refinement algorithms for triangular mesh generation**, Computational Geometry 22, 21–74

Virieux J., 1986: **P-Sv-wave propagation in heterogeneous media: Velocity-stress finite-difference method**, Geophysics 51, 889–901

Yamamoto M. and Kawakatsu H., 2008: **An efficient method to compute the dynamic response of a fluid-filled crack**, Geophysical Journal International 174, 1174–1186, doi:10.1111/j.1365-246X.2008.03871.x

Zienkiewicz O. C. and Taylor R. L., 2000: **The finite element method: The Basis**, Volume 1, 5th Edition, Butterworth-Heinemann, Oxford, ISBN 0-7506-5049-4

4 Spectral modification of seismic waves propagating through solids exhibiting a resonance frequency: A 1D coupled wave propagation–oscillation model

Abstract

A 1D model is presented that couples the microscale oscillations of non–wetting fluid blobs in a partially saturated poroelastic medium with the macroscale wave propagation through the elastic skeleton. The fluid oscillations are caused by surface tension forces that act as the restoring forces driving the oscillations. The oscillations are described mathematically with the equation for a linear oscillator and the wave propagation is described with the 1D elastic wave equation. Coupling is done using Hamilton's variational principle for continuous systems. The resulting linear system of two partial differential equations is solved numerically with explicit finite differences. Numerical simulations are used to analyse the effect of solids exhibiting internal oscillations, and consequently a resonance frequency, on seismic waves propagating through such media. The phase velocity dispersion relation shows a higher phase velocity in the high–frequency limit and a lower phase velocity in the low–frequency limit. At the resonance frequency a singularity in the dispersion relation occurs. Seismic waves can initiate oscillations of the fluid by transferring energy from solid to fluid at the resonance frequency. Due to this transfer, the spectral amplitude of the solid particle velocity decreases at the resonance frequency. After initiation, the oscillatory movement of the fluid continuously transfers energy at the resonance frequency back to the solid. Therefore, the spectral amplitude of the solid particle velocity is increased at the resonance frequency. Once initiated, fluid oscillations decrease in amplitude with increasing time. Consequently, the spectral peak of the solid particle velocity at the resonance frequency decreases with time.

4.1. Introduction

A number of processes can cause oscillations with a resonance frequency within a heterogeneous rock. For example, the behaviour of non–wetting fluids entrapped in capillary tubes and in idealized pore spaces were studied (Dvorkin *et al.*, 1990; Graham and Higdon, 2000a,b), and one of the main results is the oscillatory movement of the fluids when an external force is applied (Hilpert *et al.*, 2000). The restoring force driving the oscillations is the surface tension force or capillary force. The result that isolated oil blobs in partially saturated rocks can exhibit a resonance frequency, motivated the suggestion of a new enhanced oil recovery method (EOR) termed 'wave stimulation of oil' or 'vibratory mobilization' (Beresnev and Johnson, 1994; Iassonov and Beresnev, 2003; Beresnev *et al.*, 2005; Li *et al.*, 2005; Hilpert, 2007; Pride *et al.*, 2008). Another example of solids exhibiting internal oscillations is cavities or other heterogeneities in solids. These heterogeneities can oscillate and exhibit a resonance frequency (Meyer *et al.*, 1958; Anderson and Hampton, 1980a,b; Landau and Lifschitz, 1997). The process is also called resonant scattering (Werby and Gaunaurd, 1989, 1990; Hassan and Nagy, 1997) and has applications in non–destructive testing of materials (Ida and Wang, 1996; Castellini *et al.*, 2000; Schultz *et al.*, 2006). A third example of oscillatory behaviour is stratified media. Urquizu and Correig (2004) showed that under certain circumstances a seismic wave pulse propagating through a layered medium can be described mathematically with a differential equation for an oscillator.

The oscillating effects caused by heterogeneities or layered media are implicitly included in numerical models solving the full elastodynamic wave equations, as long as the heterogeneities or the layering are numerically well resolved (e.g. Frehner *et al.*, 2008). However, the oscillatory behaviour of non–wetting fluid blobs in partially saturated rocks (e.g. Hilpert *et al.*, 2000) is not included in mathematical models of wave propagation in partially saturated rocks. These models can be separated into two groups: 1) models based on Biot's equations (Biot, 1962) for fully–saturated rocks, applying a spatial variation of the pore fluid properties representing a partial saturation on the mesoscale (i.e. larger than the pore size and smaller than the wavelength; White (1975); Dutta and Ode (1979)), and 2) models for three–phase (i.e. solid, wetting and non–wetting fluid) media considering a partial saturation on the pore scale, including particular capillary

74

pressure versus saturation relations (Santos *et al.*, 1990; Tuncay and Corapcioglu, 1996; Smeulders and Van Dongen, 1997; Wei and Muraleetharan, 2002). In the derivation of all of these continuum models for fully and partially saturated media, the individual phases are usually mixed and their properties are averaged in a so–called representative elementary volume. During this averaging the individual interfaces between the wetting and non–wetting fluids in a pore disappear and the restoring force caused by the surface tension is not included in the continuum models for wave propagation in partially satu-rated rocks. Therefore, in these continuum models only the flow of the pore fluids caused by fluid pressure differences (described most frequently by Darcy flow) is considered. Additionally, numerical studies of microscale wave propagation in porous rocks (Saenger *et al.*, 2007) also do not include surface tension effects. However, they include microscale scattering because they resolve the 3D pore geometry.

In this study a basic 1D model is presented that couples oscillations within a rock with the seismic wave propagation through the rock. The model is not intended to be an extension of the well–known Biot's equations (Biot, 1962) to three phases (i.e. solid, wetting and non–wetting fluid), but rather to study the fundamental energy transfer between waves and oscillations and the resulting modification of the spectral content of elastic waves while propagating through a solid exhibiting internal oscillations. Here, oscillations caused by partial saturation of porous solids with a non–wetting fluid are considered. The remaining pore space is assumed to be filled by a gas. Resonance frequencies of such oscillations lie at the low–frequency end of the seismic spectrum (Hilpert, 2007; Holzner *et al.*, 2009). The motivation of this work is to couple the microscale pore fluid oscillation models (assuming a rigid elastic skeleton) to the macroscale elastic wave propagation model for the elastic skeleton. However, the model could be modified to study other oscillatory processes.

The paper starts by deriving the coupled wave propagation–oscillation model. Next, the resulting system of two coupled differential equations is solved numerically with explicit finite differences. The dispersion relation and the energy balance of the coupled system are studied numerically and analytically. Also, the spectral modification of elastic waves propagating through solids exhibiting internal oscillations is analysed. A discussion on the model's applicability to hydrocarbon reservoirs is followed by conclusions.

4.2. Mathematical Model

4.2.1. Elastic solid

The behaviour of the elastic solid in 1D is described by the total stress in the elastic solid σ^s, the strain ε^s, being the spatial derivative of solid displacement u^s and the elastic modulus K. The elastic stress–strain constitutive relationship with x as the spatial coordinate is

$$\sigma^s = K\varepsilon^s = K\frac{\partial u^s}{\partial x}, \tag{4.1}$$

where K represents the bulk modulus of the poroelastic rock, which is saturated by two immiscible fluids. The value of K is a function of the dry rock frame bulk modulus, the grain bulk modulus, the bulk moduli of the two fluids and the porosity (Gassmann, 1951; Berryman and Milton, 1991; Toms *et al.*, 2006). There exists good understanding on the value of K within the general theory of porous media (Borja, 2006; Gray and Schrefler, 2007), and values of K are, for example, applied in the theory of wave propagation in partially saturated rocks (Santos *et al.*, 1990; Tuncay and Corapcioglu, 1996). In the low–frequency range, the Gassmann–Wood limit can be applied to estimate the value of K (Mavko *et al.*, 2003). Thereby, Wood's law is used to calculate the effective fluid bulk modulus from the bulk moduli of the two immiscible fluids and this effective fluid bulk modulus is then used in the Gassmann relations (Gassmann, 1951) to estimate the effective bulk modulus of the fluid–saturated rock.

4.2.2. Fluid movement as linear oscillations

In the following, oscillations caused by partial saturation of porous solids with a non–wetting fluid are considered. The remaining pore space is assumed to be filled by a gas. Beresnev (2006) showed that the movement of such non–wetting fluids can be described with an oscillator equation. Here, a 1D harmonic oscillator equation with an angular resonance frequency ω_0 is assumed to represent this oscillatory behaviour:

76

$$\ddot{u}^f = -\omega_0^2 \left(u^f - u^s \right).$$ (4.2)

Superscripts f and s refer to the non–wetting fluid and the solid rock frame, respectively, and u and $\ddot{u}$ are displacement and second time derivative of displacement. The restoring force that leads to a oscillatory behaviour is the surface tension force or capillary force (Dvorkin *et al.*, 1990; Hilpert *et al.*, 2000; Hilpert, 2007; Holzner *et al.*, 2009). Both the non–wetting pore fluid and the solid rock frame can be deformed, but only the relative displacement leads to a restoring force. Therefore, the relative displacement is used on the right–hand side of Equation 4.2. Hilpert *et al.* (2000) and Holzner *et al.* (2009) derived analytical formulae for ω_0 using different pore geometries and different boundary conditions at the pore wall. Hilpert *et al.* (2000) used a fluid blob with pinned contact lines in a pore with straight walls. The resulting formula is

$$\omega_0 = \sqrt{\frac{4\gamma}{r^2 h \rho^f} \sin\theta_0 \left(1 + \sin\theta_0\right)^2}.$$ (4.3)

Holzner *et al.* (2009) used a fluid blob with sliding contact lines in a bi–conically shaped pore. The resulting formula is

$$\omega_0 = \sqrt{\frac{6\gamma}{r h^2 \rho^f}}.$$ (4.4)

In both formulae, the parameters γ , r, h and ρ^f are surface tension, radius of the pore, length of the fluid blob and density of the fluid, respectively. θ_0 in Equation 4.3 is the contact angle between the non–wetting fluid surface and the rigid pore wall. The two formulae have the same structure. Table 4.1 lists a set of parameters that is in accordance with the parameters used by Hilpert *et al.* (2000) and Holzner *et al.* (2009). Using these parameters, Equation 4.3 results in $\omega_0 = 107.7$ ($= 17.1$ Hz $\times 2\pi$) and Equation 4.4 in $\omega_0 = 75.1$ ($= 12.0$ Hz $\times 2\pi$)), which is the same order of magnitude. The difference is a result of the different pore geometries and boundary conditions at the pore walls of the two cases. Considering n oscillators, the total kinetic energy of the fluid E_{kin}^f is

$$E_{kin}^f = \frac{1}{2} \sum_{j=1}^{n} m_j^f \left(\dot{u}_j^f \right)^2. \tag{4.5}$$

In Equation 4.5 m_j^f and $\dot{u}_j^f$ are mass and time derivative of the displacement of each individual oscillator. The pores are assumed to be non–connected. The individual oscillations therefore do not interact with each other directly. However, the individual fluid oscillations are coupled indirectly through their coupling to the solid (see below). Also, the individual oscillations are assumed to exhibit the same resonance frequency ω_0. These two major assumptions lead to a simplified model where no fluid flow between pores can take place. There will be no wave travelling due to the presence of the fluid, such as the Biot slow wave. However, the resulting model allows studying first–order effects of the oscillations on seismic wave propagation, which is included below. The total potential energy of the pore fluid, E_{pot}^f, is the sum of the individual potential energies:

$$E_{pot}^f = \frac{1}{2} \sum_{j=1}^{n} m_j^f \omega_0^2 \left(u_j^f - u_j^s \right)^2. \tag{4.6}$$

Parameter	Symbol	Value
Surface tension	γ	0.02 N/m
Radius of pore	r	0.001 m
Length of pore	h	0.005 m
Density of fluid	ρ^f	850 kg/m^3
Contact angle	θ_0	20°

Table 4.1: Parameters used to calculate the resonance frequency ω_0 with Equations 4.3 and 4.4.

4.2.3. Coupling between fluid oscillations and elastic waves

The coupling of the microscale (i.e. pore scale) fluid oscillations with a 1D linear elastic solid yields the effective rheological model sketched in Figure 4.1. Two displacements have to be considered individually in this model, the displacement of the solid phase u^s and the displacement of the oscillating fluid phase u^f. The solid is represented by a linear elastic element and the fluid by an oscillating mass. The elastic wave propagation and the fluid oscillations are coupled using Hamilton's variational principle for continuous systems (Fetter and Walecka, 1980; Bourbie $et\ al.$, 1987). Therefore, the energies of the oscillating fluid (Equations 4.5 and 4.6), which were defined in a discrete way, need to be reformulated in the continuous limit. The different contributions to the total system energy are then written in the following way:
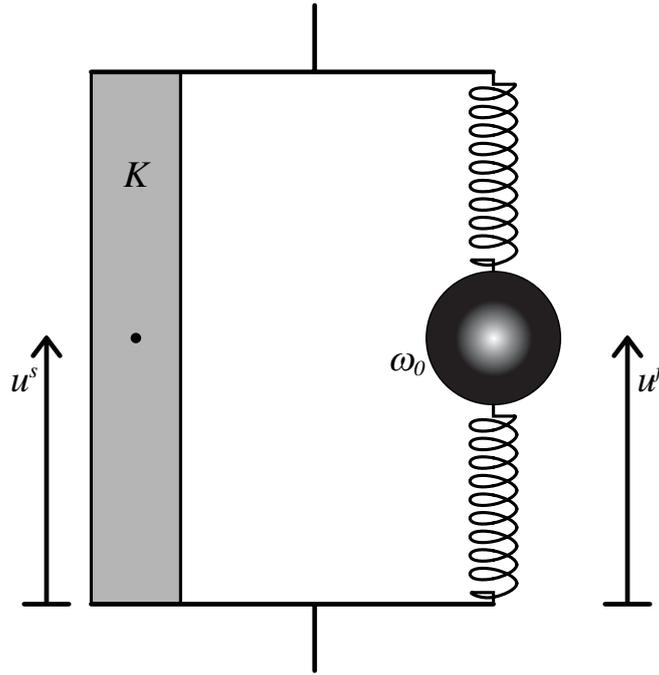
Figure 4.1: Schematic rheological model for coupling between elastic deformation and fluid oscillations. The elastic bar with bulk modulus K on the left–hand side is coupled in parallel with a linear oscillator with a resonance frequency ω_0.

$$E_{kin}^f \quad = \quad \frac{1}{2} \int_0^l S\phi\rho^f \left(\dot{u}^f\right)^2 dx, \tag{4.7}$$

$$E_{pot}^f \quad = \quad \frac{1}{2} \int_0^l S\phi\rho^f \omega_0^2 \left(u^f - u^s\right)^2 dx, \tag{4.8}$$

$$E_{kin}^s \quad = \quad \frac{1}{2} \int_0^l \left(1 - \phi\right) \rho^s \left(\dot{u}^s\right)^2 dx, \tag{4.9}$$

$$E_{pot}^s \quad = \quad \frac{1}{2} \int_0^l \sigma^s \varepsilon^s dx. \tag{4.10}$$

Parameters ρ^f, ρ^s and l are density of the fluid and the solid, respectively, and length of the 1D model. Parameters ϕ and S are porosity of the rock matrix and saturation of the pores by the non–wetting fluid, respectively. Both parameters are dimensionless and have a value between 0 and 1. They are both assumed to be constant in time, that is, porosity and saturation do not change when a wave is passing. Equations 4.7–4.10 only consider the solid and the non–wetting fluid phase. In the presented cases, saturation of the pores is smaller than 1 and a third phase is present. It is assumed that the third phase is gaseous and that both its kinetic and potential energies are small compared to the fluid and solid phases. Therefore, the third phase is neglected. Also, the gaseous phase is assumed to have a much smaller bulk modulus than the fluid phase. Therefore, the compression of the fluid can be neglected and the fluid bulk modulus is not considered as a model parameter. Combining Equations 4.7–4.10, the Lagrangian functional L can be formulated (Fetter and Walecka, 1980) using the total kinetic energy T and the total potential energy U:

$$L = T - U = \left(E_{kin}^f + E_{kin}^s\right) - \left(E_{pot}^f + E_{pot}^s\right) = \int_0^l \mathcal{L} dx. \tag{4.11}$$

The Lagrangian density $\mathcal{L}$ has the dimension of energy per unit length. Hamilton's variational principle for continuous systems (Fetter and Walecka, 1980; Bourbie *et al.*, 1987) can now be applied to the Lagrangian functional:

$$\delta \int_{t_1}^{t_2} L dt = \int_{t_1}^{t_2} \int_0^l \delta\mathcal{L} dx dt = \int_{t_1}^{t_2} \int_0^l \left\{ \frac{\partial\mathcal{L}}{\partial u^i} - \frac{d}{dt}\left(\frac{\partial\mathcal{L}}{\partial \dot{u}^i}\right) - \frac{d}{dx}\left(\frac{\partial\mathcal{L}}{\partial \varepsilon^i}\right) \right\} \delta u^i dx dt = 0. \quad (4.12)$$

Superscript i in Equation 4.12 replaces superscripts s (solid) or f (fluid). The variations δu^i are arbitrary (Fetter and Walecka, 1980). Therefore, their coefficients in curly brackets must be equal to zero. The resulting equations are the Euler–Lagrange equations for the continuous two–component system:

$$\frac{\partial\mathcal{L}}{\partial u^i} - \frac{d}{dt}\left(\frac{\partial\mathcal{L}}{\partial \dot{u}^i}\right) - \frac{d}{dx}\left(\frac{\partial\mathcal{L}}{\partial \varepsilon^i}\right) = 0. \quad (4.13)$$

The Lagrangian density $\mathcal{L}$ (in Equation 4.11) is substituted into the Euler–Lagrange equations. The final equations of motions are

$$S\phi\rho^f \ddot{u}^f = -S\phi\rho^f \omega_0^2 \left(u^f - u^s\right), \quad (4.14)$$

$$(1-\phi)\rho^s \ddot{u}^s = \frac{\partial}{\partial x}\left(K\frac{\partial u^s}{\partial x}\right) + S\phi\rho^f \omega_0^2 \left(u^f - u^s\right). \quad (4.15)$$

Equations 4.14 and 4.15 form a closed system of two equations for the two unknown functions u^s and u^f. Equation 4.14 is identical to a linear 1D oscillator equation (Equation 4.2) but is formulated in terms of averaged density $(S\phi\rho^f)$. The left–hand side together with the first term of the right–hand side of Equation 4.15 represents a 1D wave equation (Lindsay, 1960; Achenbach, 1973; Szabo, 1985). It is also written in terms of averaged density $[(1-\phi)\rho^s]$. This 1D wave equation can represent a P–wave or an S–wave, depending on the interpretation of the unknown solid displacement u^s and the material parameter K. In this study, the solid displacement is assumed to be parallel

to the propagation direction of the wave as well as parallel to the fluid displacement u^f. Therefore, in the following, the solid wave is called a P–wave. The additional term on the right–hand side of Equation 4.15 links the fluid motion and the solid motion. If Equations 4.14 and 4.15 are added the coupling term disappears and the equation of conservation of the total linear momentum can be derived.

4.3. Numerical Model

Equation 4.1, the two Equations 4.14 and 4.15 and two additional kinematic equations ($\partial u^i / \partial t = v^i$) represent a coupled system of five first–order linear partial differential equations. The equations are spatially discretized over the model length l using the finite difference method with a 1D staggered grid (Virieux, 1986). The two displacements and the two velocities are defined on nodal points and the solid stress is defined on staggered points (i.e. center points). Discretization in time is formulated explicitly with a staggered method (Virieux, 1986). For some simulations the boundary conditions are rigid (all displacements and velocities are equal to zero) and for some simulations, non–reflecting (Ionescu and Igel, 2003). Figure 4.2 shows the model setup used in this study. Time signals are recorded at two synthetic receiver locations R_1 and R_2. For some simulations an external source is applied at the position S. In fact, the source is active over a small number of spatial gridpoints whereas the source amplitude is highest at position S and decays strongly over a few numerical points. The source acts as an additional force term in Equation 4.15 and therefore acts only on the elastic solid. The fluid phase is only affected indirectly through the coupling terms in Equations 4.14 and 4.15. The resonance frequency of the pore fluid oscillations is set to 3 Hz throughout the model domain but, using non–dimensionalization, the results can be translated to other frequencies. Physical parameters used in the simulations are given in Table 4.2. For all simulations the spatial resolution is chosen in such a way that the wavelength of a P–wave with a frequency of 50 Hz is resolved with 50 nodal points. The explicit time increment is calculated using the von Neumann stability criterion (Virieux, 1986; Higham, 1996).
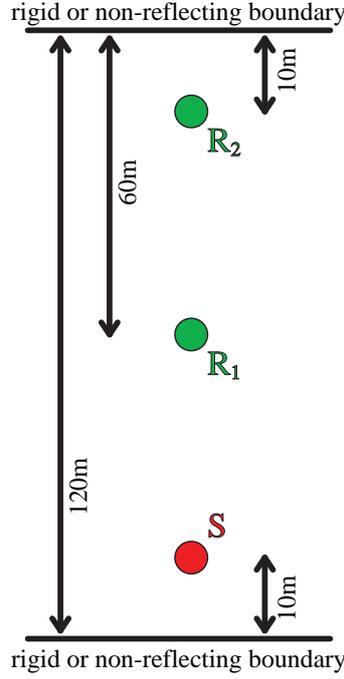
Figure 4.2: 1D model setup for numerical simulations consists of two receivers R_1 and R_2 and one source S. The whole domain is described by the coupled system of Equations 4.14 and 4.15. The lower and upper boundaries can be rigid (zero displacement) or non–reflecting.

Parameter	Symbol	Value
Resonance frequency of oscillations	ω_0	18.85 (= 3 Hz $\times 2\pi$)
Density of fluid	ρ^f	800 kg/m^3
Density of solid	ρ^s	2800 kg/m^3
Elastic bulk modulus	K	10^{10} Pa
Porosity	ϕ	0.3
Non–wetting fluid saturation of pores	S	0.9
Frequency of external source	Ω	$\omega_0/10$
High–frequency limit of P–wave velocity	V_P^{HF}	2259 m/s
Low–frequency limit of P–wave velocity	V_P^{LF}	2132 m/s

Table 4.2: Parameters used in numerical simulations.

4.4. Numerical Results

4.4.1. Energy conservation and transfer

To test for conservation of energy of the numerical scheme a homogeneous numerical simulation was performed with two rigid boundaries (Figure 4.2). No source function was applied, but a Gaussian–shaped initial perturbation of the solid velocity field was prescribed. After the simulation started, this perturbation propagates through the solid part of the model as an elastic wave and also initiates the fluid oscillations. In Figure 4.3 the four energies in the system (Equations 4.7 – 4.10), which are calculated from the numerical simulation, are plotted versus time.
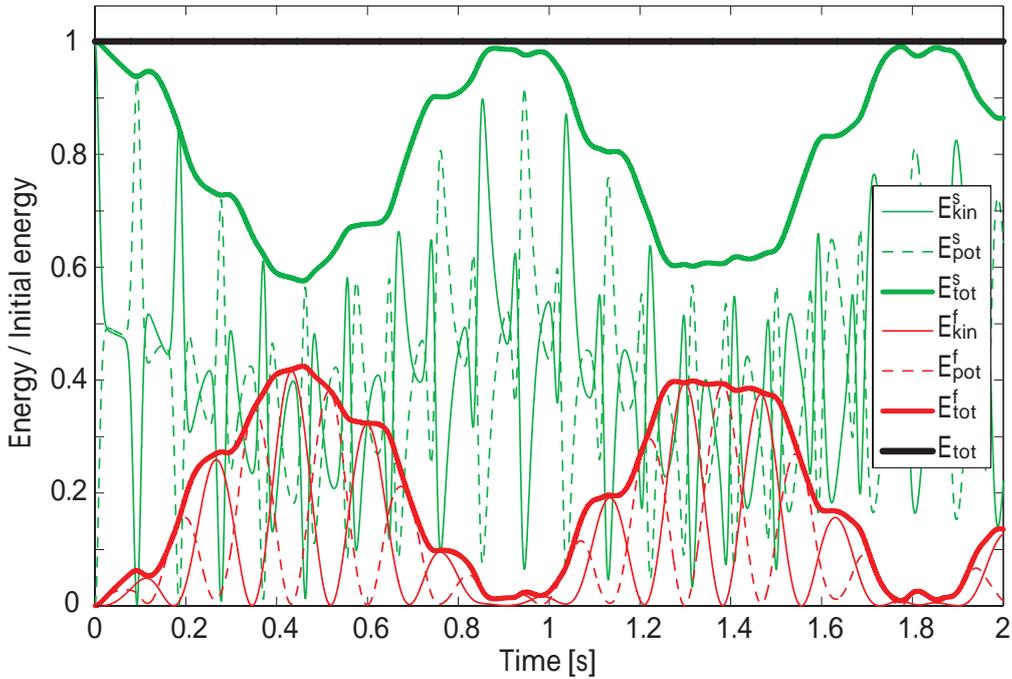
Figure 4.3: Time evolution of the different energies in the coupled system (Equations 4.7–4.10). A 120 m long homogeneous model with two rigid boundaries is used, and an initial perturbation in the solid velocity field is applied. The total energy, that is, the sum of all energies (thick black line) stays constant over time. Individual energy contributions are transferred between fluid (red lines) and solid (green lines) phases.

The energies of the solid and the fluid phase always add up to a constant total system energy. The total energy of the system is conserved, which also illustrates the correctness of the numerical algorithm. At time zero, following the initial conditions, energy of the fluid is zero and energy of the solid is maximal. A significant part of the energy is then transferred back and forth between solid and fluid phase, showing that the pore fluid oscillations influence the behaviour of the solid phase considerably. For example, after about 0.4 s, the solid has transferred about 45 % of its total energy to the fluid (Figure 4.3).

4.4.2. Eigenvalues and dispersion curve

In Figure 4.4 the phase velocity dispersion curve for a P–wave travelling in a medium described by the coupled Equations 4.14 and 4.15 is plotted. The black line is the analytical P–wave phase velocity as a function of frequency that is calculated from the eigenvalues of Equations 4.14 and 4.15. For calculating the phase velocity numerically (red dots in Figure 4.4), several simulations were performed using different frequencies Ω in the external source function,

$$F\left(t\right) = \sin\left(\Omega t\right). \tag{4.16}$$

The source function was applied at position S of the model shown in Figure 4.2 with two non–reflecting boundaries. The phase velocity of the P–wave was calculated from the time–shift between the recordings at receivers R_1 and R_2. Numerical results agree well with the analytically calculated phase velocity and the numerical simulations reproduce well the phase velocity discontinuity around the resonance frequency.

The P–wave velocity in a dry poroelastic solid $\sqrt{K/[(1 - \phi)\,\rho^s]}$ is the high–frequency limit of the dispersion relation. At frequencies much larger than the resonance frequency, inertia prohibits a movement of the pore fluid and the seismic waves travel as if there was no pore fluid. At frequencies much smaller than the resonance frequency, solid and fluid move in phase. In this regime, the effective density that has to be considered in calculating the P–wave velocity is a combination of fluid and solid densities, and it becomes

$\sqrt{K/[(1 - \phi)\,\rho^s + S\phi\rho^f]}$. This low–frequency limit is very similar to the low–frequency limit of the Biot's equations (Gassmann, 1951; Geerstma and Smit, 1961) but using a constant bulk modulus. At frequencies just below the resonance frequency of the fluid oscillations a decrease of phase velocity is observed, followed by a sharp velocity jump at the resonance frequency to very high values. Mathematically, the phase velocity is indefinite at this point. With increasing frequencies the phase velocity decreases and finally reaches the high–frequency limit. This characteristic P–wave velocity dispersion curve is also observed in other media that exhibit an internal resonance behaviour. For example Fox *et al.* (1955), Silberman (1957) and Anderson and Hampton (1980a) measured and described a very similar dispersion relation in water containing gas bubbles. Although the mechanism of oscillation is different, the effect on the propagation of seismic waves is comparable. The model described by Equations 4.14 and 4.15 conserves energy (Figure 4.3). Therefore, P–waves are not attenuated. Attenuation can be calculated from the eigenvalues of the system of Equations 4.14 and 4.15, but it results in zero attenuation for all frequencies.
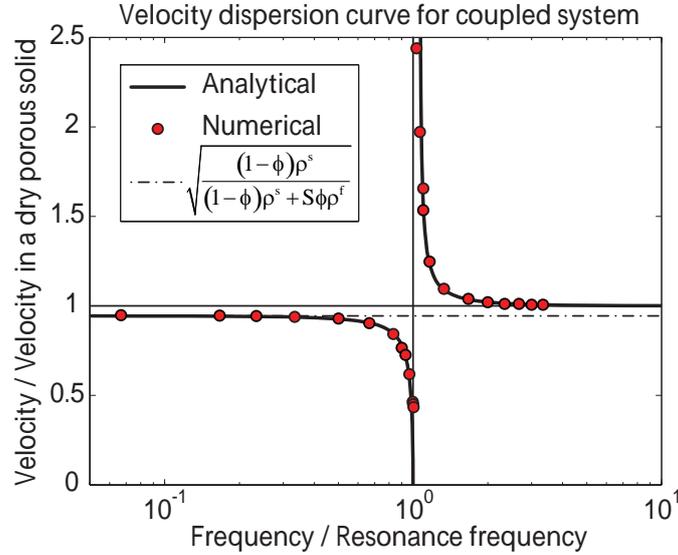
Figure 4.4: P–wave phase velocity versus frequency. Frequency is normalized with the resonance frequency of the fluid oscillations. Velocity is normalized with the phase velocity in a dry porous rock. Analytical phase velocity is calculated from the eigenvalues of the system of Equations 4.14 and 4.15. Numerical phase velocities are calculated from simulations with a monochromatic external source. Each point represents one individual simulation using one particular external frequency.

4.4.3. Spectrograms for wave incidence

A numerical simulation was run with the model setup shown in Figure 4.2 with two non–reflecting boundaries. The external source applied at position S is a Gaussian curve in time,

$$F\left(t\right) = \exp\left[-\frac{(t-t_0)^2}{2\tau^2}\right], \qquad (4.17)$$

where $t_0 = 10$ s and $\tau = 0.01$ s. The inlay in Figure 4.5a) shows the spectrum of this source function. At receiver R_2, both fluid and solid particle velocities were recorded. Figure 4.5 shows the spectrograms for both particle velocities. The spectral values are normalized with the spectrum of the external source. To calculate a spectrogram, a 10 s time window is moved along the time axis of the recorded particle velocity–time signal with 1 s steps. For each step, the spectrum is calculated and plotted at the center of the 10 s window. Due to this algorithm, the pulse of the external source is visible in the spectrogram between 5 and 15 s. Over this time interval, the spectrogram of the solid particle velocity (Figure 4.5a) shows a minimum at the resonance frequency of the fluid oscillations. The amplitude of this minimum is around one order of magnitude smaller than the amplitude of the external source (orange colour of the minimum). The second half of the spectrogram, where the external source is not present, shows a peak at this frequency. Immediately after the source pulse has passed, this peak has the same amplitude as the source at this frequency (dark red colour of the peak). The amplitude of the peak decreases over time, becoming around one order of magnitude smaller after 25 s (orange colour). The spectrogram of the fluid velocity (Figure 4.5b) shows a peak at the resonance frequency of the fluid oscillations throughout the whole simulation. The amplitude of this peak is larger than the amplitude of the external source at this frequency.
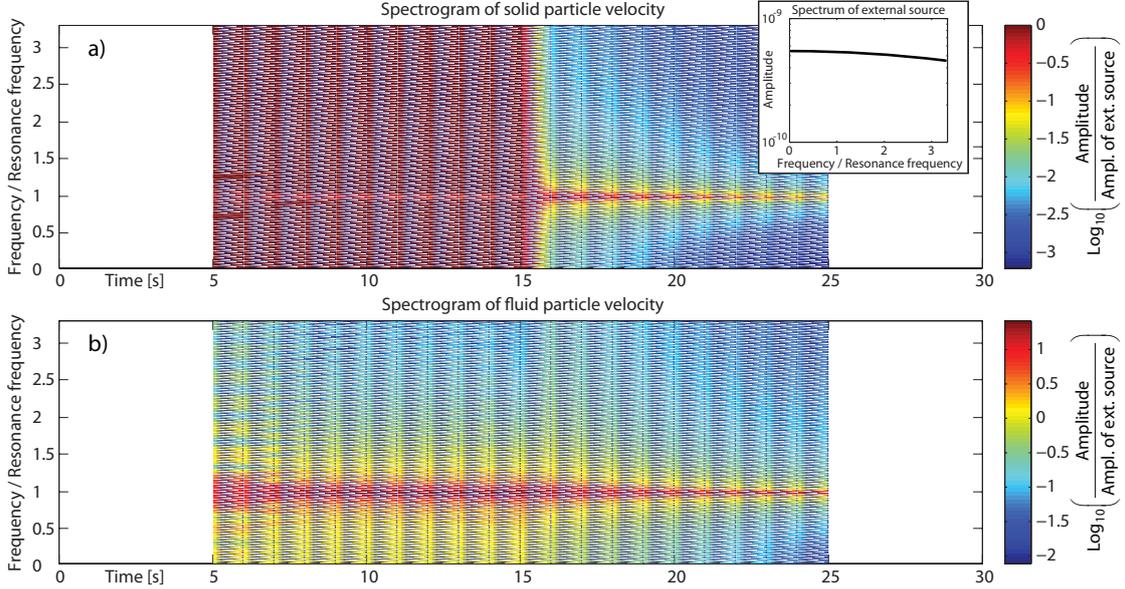
Figure 4.5: Spectrogram of solid (a) and fluid (b) particle velocities at receiver R_2 of the model shown in Figure 4.2, with two non–reflecting boundaries. Inlay: Spectrum of the applied Gaussian source function (Equation 4.17) applied at position S. Frequency is normalized with the resonance frequency of the fluid oscillations. Spectral values are normalized with the spectrum of the source function and are plotted logarithmically. Due to the algorithm calculating the spectrograms (see text), the Gaussian peak of the external source is visible for 10 s (between 5 and 15 s).

Figure 4.5 indicates that at the moment of incidence of the elastic wave, fluid oscillations are immediately excited. The oscillations take place at the resonance frequency. Therefore, a maximum at the resonance frequency develops in the spectrogram of the fluid particle velocity from the very beginning of the simulation (Figure 4.5b). At the same time, a minimum in the spectrogram of the solid particle velocity develops at this frequency (Figure 4.5a). This happens because the energy for the initiation of the fluid oscillations is taken from the solid. This energy transfer from solid to fluid takes place only at the resonance frequency due to the linear nature of the system equations. After the fluid oscillations are initiated and the elastic wave has passed, the fluid continues to oscillate with its resonance frequency. Fluid oscillations in adjacent pores are almost in phase because they are excited by the macroscale elastic wave at almost the same

instant. Therefore, the effect of the different pores on the seismic wave adds up to a measurable effect. The oscillating fluid continuously transfers energy back to the solid. This energy transfer from fluid to solid happens only at the resonance frequency due to the linear nature of the system equations. Therefore, a maximum in the spectrogram of the solid particle velocity occurs at this frequency (Figure 4.5a). The amplitude of this peak cannot be larger than the amplitude of the external source, which initialized the oscillations. The non–reflecting boundaries of the system allow the P–waves to transport energy out of the system. Therefore, the fluid oscillations decrease in amplitude and the maxima in both spectrograms decrease.

4.4.4. Resonance curves

Figure 4.6 shows two resonance curves for the coupled Equations 4.14 and 4.15. The two curves represent the solid and the fluid response at the frequency of the external source. They are numerically calculated in the following way: a set of numerical simulations was performed using a different frequency Ω in the monochromatic external source function (Equation 4.16) for each of the simulations. The source function was applied at position S of the model shown in Figure 4.2 with two non–reflecting boundaries. For each simulation two mean spectra are calculated, one for the fluid particle velocity and one for the solid particle velocity, both recorded for 300 s at receiver R_2. Mean spectra are calculated by arithmetically averaging in time the spectrograms that are calculated the same way as described above for Figure 4.5. From these two mean spectra, the spectral values are picked at the external frequency Ω. Each simulation (i.e. each external frequency) results in two spectral values (i.e. solid and fluid response at the external frequency) that are plotted in Figure 4.6. The frequency is normalized with the resonance frequency of the fluid oscillations. Spectral values are normalized with the spectral values of the external source function.

As expected for an oscillatory behaviour, the closer the external frequency is to the resonance frequency the stronger the fluid response becomes. Below the resonance frequency, the fluid response is equal to the solid response at very low external frequencies. Above

the resonance frequency, the fluid response becomes much smaller than the solid response with increasing frequency. The solid response is equal to the external source for all frequencies except for a sharp minimum at the resonance frequency of the fluid oscillations. The amplitude of this minimum is around one order of magnitude smaller than the amplitude of the external source. This is very similar to the minimum described in the first half of Figure 4.5a). The observations in Figure 4.6 can be interpreted with the energy transfer already described for Figures 4.3 and 4.5. The minimum in the solid response develops because energy is transferred from solid to fluid only at the resonance frequency to drive the fluid oscillations. At very low frequencies, the fluid moves in phase with the solid. Consequently, the fluid response at very low external frequencies is equal to the solid response. At very high external frequencies, inertia of the fluid prohibits excitation of the oscillations and the fluid does not move. Consequently, the fluid response becomes very small with increasing frequency.
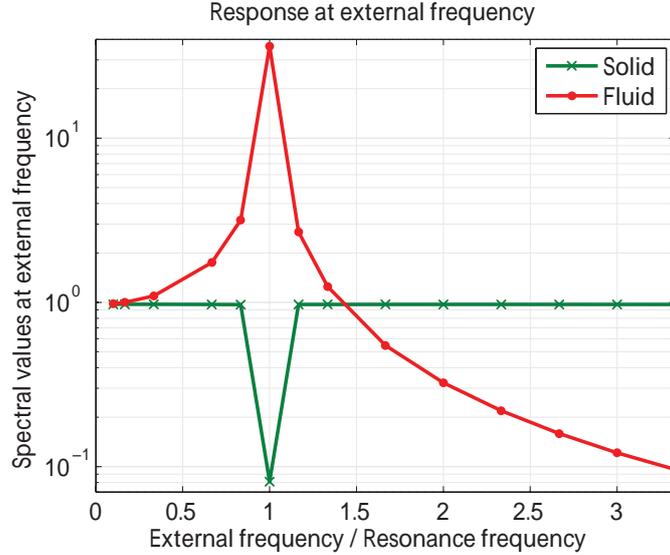
Figure 4.6: Spectral response of the fluid and solid particle velocity at the external source frequency for different external frequencies. Velocities are recorded at receiver R_2 of the model shown in Figure 4.2, with two non–reflecting boundaries. One simulation with a monochromatic source function (Equation 4.16) at position S provides the two data points at one frequency. Frequency is normalized with the resonance frequency of the fluid oscillations. Spectral values are normalized with the spectral values of the external source.
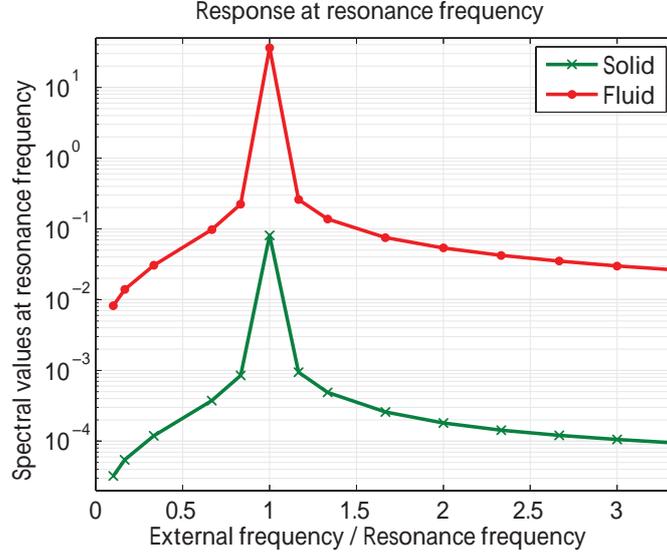
Figure 4.7: Spectral response of the fluid and solid particle velocity at the resonance frequency for different external frequencies. Velocities are recorded at receiver R_2 of the model shown in Figure 4.2 with two non–reflecting boundaries. One simulation with a monochromatic source function (Equation 4.16) at position S provides the two data points at one frequency. Frequency is normalized with the resonance frequency of the fluid oscillations. Spectral values are normalized with the spectral values of the external source.

Figure 4.7 shows two resonance curves that are similar to the ones in Figure 4.6. The two curves represent the solid and the fluid response at the resonance frequency of the fluid oscillations. They are calculated in the same way as described above for Figure 4.6, but instead of picking the spectral values at the external frequency in the mean spectra, the spectral values are picked at the resonance frequency. Normalization of the frequency and of the spectral values is also done in the same way as in Figure 4.6. The two data points at an external frequency equal to the resonance frequency are the same data points as in Figure 4.6 at the same frequency. The two curves in Figure 4.7 have the same shape but different amplitudes. They clearly represent the resonance effect of the fluid. The closer the external frequency is to the resonance frequency, the stronger the fluid response becomes. Because energy transfer between fluid and solid only takes place at the resonance frequency, the solid response at the resonance frequency is dominated by the oscillatory behaviour of the fluid. However, the fluid oscillations are also excited

for other external frequencies than the resonance frequency, that is, spectra do not drop to zero for external frequencies different from the resonance frequency. This is an effect of the incidence of the elastic wave at the beginning of each simulation. At the moment of elastic wave incidence, all frequencies are introduced into the system and the fluid oscillations are excited. This excitation is stronger for elastic waves having a frequency close to the resonance frequency.

4.4.5. Comparison to purely elastic case

From the set of numerical simulations used in Figures 4.6 and 4.7, one simulation is taken for comparison with a purely elastic model. The chosen simulation uses a monochromatic external source (Equation 4.16) applied at position S with a frequency Ω, 10 times smaller than the resonance frequency. This choice is motivated by the fact that the Fourier spectra of typical passive measurements of seismic background noise show a dominant peak at around 0.2 Hz (Peterson, 1993; Berger *et al.*, 2004), which is about a factor 10 smaller than the applied resonance frequency. This high–energy spectral peak is a global feature that can be measured everywhere in the world and is presumably related to seismic surface waves generated by ocean waves (Aki and Richards, 2002). After different simulation durations, a Fourier spectrum is calculated from the solid particle velocity recorded at receiver R_2. The procedure to calculate a spectrum is not a moving–window method with a constant time–window length but always uses the whole time signal from the beginning of the simulation until the current time. It is therefore different from the method used to produce Figures 4.5–4.7. For the same simulation duration, a model is considered that has the same dimensions, the same source and receiver locations and the same elastic properties as the numerical model but is purely elastic and does not exhibit internal oscillations. Because this additional model is purely elastic, the particle velocity–time signal at receiver R_2 can be analytically calculated.
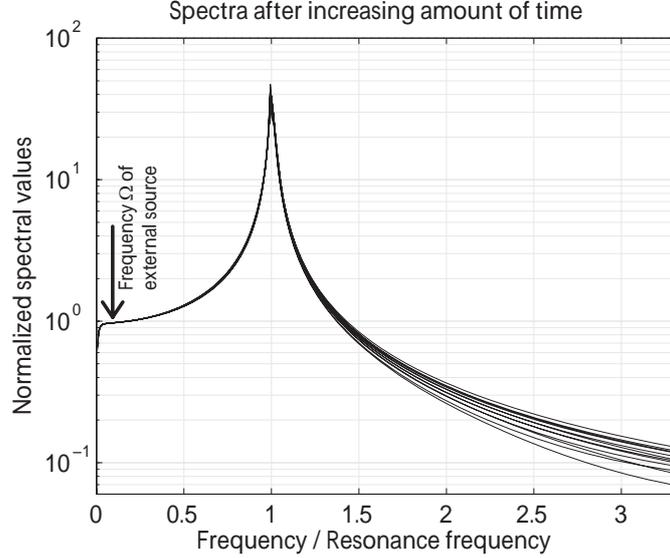
Figure 4.8: Fourier spectra of solid particle velocity–time signal at receiver R_2 of the model shown in Figure 4.2 with two non–reflecting boundaries. A monochromatic source (Equation 4.16) is applied at position S with a frequency 10 times smaller than the resonance frequency of the fluid oscillations. Different spectra are calculated after different simulation lengths. Longest time signal is 120 s, shortest is 3.5 s. Frequency is normalized with the resonance frequency of the fluid oscillations. Spectra are normalized with spectra of the analytically calculated solid particle velocity–time signal at the same receiver but for a purely elastic model.

Figure 4.8 shows the division of the Fourier spectrum derived from the numerical simulation (model exhibiting internal oscillations) by the Fourier spectrum derived from the analytical time signal (purely elastic) for different simulation lengths. The frequency is normalized with the resonance frequency of the fluid oscillations. The two spectra before the division (not shown here) show a very distinct peak at the frequency of the external source. This peak has a constant value after different simulation durations. Also, this peak has the same value for both models (with internal oscillations and purely elastic) and therefore cancels to a value of 1 when the two spectra are divided (Figure 4.8). Evolution of the two spectra before the division (not shown here) shows that the spectral amplitude of all other frequencies than the external frequency decreases with increasing simulation duration. This decrease of spectral amplitudes is exactly the same for the two cases (with internal oscillations and purely elastic). Therefore, the division of the two

spectra lets them collapse onto one single curve (Figure 4.8), no matter what simulation duration was considered.

The decrease of spectral amplitudes with increasing simulation duration before the spectral division is interpreted in the following way. The particle velocity–time signal contains the incidence of the elastic wave front as the first event. This event introduces all frequencies when the Fourier spectrum is calculated. After that, the particle velocity–time signal contains only the signal of the monochromatic source (in the purely elastic case) and the signal of the oscillating fluid that is transferred to the solid. For a long simulation, the monochromatic part of the time signal dominates and the first event, which introduced all other frequencies, becomes less important in calculating the Fourier spectrum. Therefore, although the monochromatic part of the time signal stays constant, the spectral amplitude of all other frequencies decreases with time. Figure 4.8 therefore shows the time–independent spectral difference between the recorded particle velocity–time signal at receiver R_2 of the model exhibiting internal oscillations and the purely elastic model. The strong peak at the resonance frequency is initiated at the very beginning of the simulation when the wave front of the source signal propagates through the medium and initiates the fluid oscillations. The time–constant peak in Figure 4.8 shows that the amplitude at the resonance frequency decreases with the same rate as in the purely elastic case and that no intrinsic attenuation due to the fluid oscillations takes place.

4.5. Discussion

The oscillation behaviour of individual, partially saturated pores was studied thoroughly theoretically (Graham and Higdon, 2000b), experimentally (Li *et al.*, 2005) and numerically (Hilpert, 2007; Pride *et al.*, 2008; Holzner *et al.*, 2009). However, the influence of such oscillations on the propagation of seismic waves in the porous skeleton was not studied in detail. Also, oscillatory behaviour of fluids and surface tension effects are not included in poroelastic theories, such as Biot Theory (Biot, 1962), in patchy–saturation models (White, 1975; White *et al.*, 1975; Dutta and Ode, 1979), in 3–phase wave prop-

agation models (Santos *et al.*, 1990; Lo and Sposito, 2005), nor in microscale models of porous flow (Saenger *et al.*, 2007). For studying fundamental effects of the coupling between fluid oscillations and seismic wave propagation, the presented model equations (Equataions 4.14 and 4.15) are intentionally kept simple. Additional effects, for example, damping of the oscillations, interaction between individual pores (i.e. connected pores), attenuation of seismic waves, non–linear oscillations due to more complex pore geometries or more spatial dimensions could be included to gain more insight into the coupling effects. Despite the simplicity of the model, the dispersion relation (Figure 4.4) agrees well with the dispersion relation for water containing gas bubbles (Fox *et al.*, 1955; Silberman, 1957; Anderson and Hampton, 1980a), which is a comparable problem of a wave travelling through a medium exhibiting internal oscillations.

Because the system Equations 4.14 and 4.15 are linear, the energy transfer between solid and fluid only happens at the resonance frequency of the oscillations (Figures 4.5a) and 4.6). Therefore, the source, which is only active in the solid in the presented cases, needs to contain some energy at this frequency for the oscillations to be initiated. Even using a monochromatic source (Equation 4.16), every point in the model experiences a moment of seismic wave incidence because simulations are done in the time–domain. The wavefield is therefore not stationary like in a frequency–domain simulation. At the moment of seismic wave incidence all frequencies are introduced into the model, despite the monochromatic source, and the oscillations are initiated. After the wave front has passed, the fluid continues to oscillate and constantly transfers energy to the elastic porous matrix. This results in a decrease of amplitude of the oscillations as long as the oscillations stay undisturbed (Figure 4.5a). Seismic background noise in nature (Aki and Richards, 2002; Peterson, 1993) contains the most energy at around 0.2 Hz but also at larger frequencies with smaller amplitudes. Additionally, natural wavefields show significant variations in amplitude. These amplitude variations can have similar effects as individual incident wave pulses, which can potentially drive the fluid oscillations.

A possible application of the coupled wave propagation–oscillation model presented here is passive low–frequency spectral analysis applied for detection of hydrocarbon reservoirs (Dangel *et al.*, 2003; Graf *et al.*, 2007; Walker, 2008; Lambert *et al.*, 2008; Holzner *et al.*, 2009). Passive low–frequency measurements show increased spectral amplitudes between 1 to 6 Hz when the ambient seismic background noise is measured above a hydrocarbon

95

reservoir compared with measurements in areas without a reservoir. Several different physical mechanisms are discussed as a potential cause of this phenomenon (Graf *et al.*, 2007), but no accepted physical theory has been published until now. Current models suggest that reservoirs act like a filter or scatterer and modify the ambient seismic background noise. Fluid oscillations and surface tension effects could play an important role in hydrocarbon reservoirs because of the coexistence of a wetting and a non–wetting phase in the pores and other cavities, such as fractures. The presented model requires that the ambient seismic background noise contains some energy at the resonance frequency of the oscillations (presumably between 1 and 6 Hz) at reservoir depth. Bradley *et al.* (1997) and Bonnefoy-Claudet *et al.* (2006) indicate that the spectral amplitude of the ocean wave peak (0.2 Hz) stays very constant with depth but that spectral amplitudes of higher frequencies drop relatively fast with depth. However, ambient seismic noise still contains energy at these higher frequencies at reservoir depth. The presented model also requires a partial saturation of the pore space. A hydrocarbon reservoir can be only partially saturated or fully saturated. However, the effect in nature is expected to be stronger close to the oil–water contact, close to the oil–gas contact or at the margin of a reservoir, where the pores are partially saturated.

In natural environments, the resonance frequency of the fluid oscillations is not expected to be constant for all pores due to complex pore geometries, different pore sizes, different degree of connectivity or different degree of saturation. In addition, there can be other effects causing oscillatory behaviour of a solid with a different resonance frequency, such as multiple reflections in layered media (Urquizu and Correig, 2004) or resonant scattering at heterogeneities (Werby and Gaunaurd, 1989, 1990; Hassan and Nagy, 1997). Therefore, natural media should be represented by a range of resonance frequencies rather than one particular value. The expected effects are smoother peaks and minima rather than such strong and distinct peaks and minima shown in Figures 4.5 – 4.8.

4.6. Conclusions

The impact of media exhibiting internal oscillations on elastic waves propagating through such media is studied with a basic 1D model that couples microscale oscillations with macroscale seismic waves. Oscillations are assumed to arise from non–wetting fluids trapped in pores or other cavities in the solid rock matrix but can also arise from other processes. The coupling of fluid oscillations with wave propagation models causes dispersion of the P–wave velocities around the resonance frequency (Figure 4.4). Numerical simulations show that incident seismic waves initiate oscillations in the media. The energy required for the initiation of the oscillations is transferred from solid to fluid at the resonance frequency. A seismic wave front therefore looses energy at the resonance frequency and a minimum in the spectrum of the solid particle velocity develops. After the wave front has passed, the fluid continues to oscillate with its resonance frequency and energy is continuously transferred back from fluid to solid. Therefore, a peak develops in the spectrum of the solid particle velocity after the wave front has passed. The continuous transfer of energy from fluid to solid after the wave front has passed leads to a decrease of amplitude of the fluid oscillations. Consequently, the spectral peak at the resonance frequency also decreases with increasing time (Figure 4.5). However, no intrinsic attenuation takes place due to the fluid oscillations (Figure 4.8).

The results indicate that the frequency content of a wavefield can be modified by a medium exhibiting a resonance frequency as long as the original wavefield contains energy at the resonance frequency. Depending on the piece of the recorded particle velocity–time signal used for calculating the Fourier spectrum the spectral amplitude at the resonance frequency can be larger (i.e. a peak) or smaller (i.e. a minimum) than in the original wave. No constant peak or constant minimum is expected.

The presented model is a basic one for studying fundamental effects. It includes the impact of fluid oscillations on propagating waves that is not included in poroelastic theories or in microscale models. Oscillatory effects might play an important role in natural porous media that are partially saturated with a non–wetting fluid, such as hydrocarbon reservoirs, or other media exhibiting a resonance frequency. Despite the simplicity of the presented model, the dispersion relation agrees well with the one for water containing gas bubbles, which is another example of a medium exhibiting a resonance frequency.

97

Acknowledgements

References

Achenbach J. D., 1973: **Wave propagation in elastic solids**, Volume 16 of North-Holland series in Applied Mathematics and Mechanics, North-Holland Publishing Company, Amsterdam, ISBN 0-7204-2367-8

Aki K. and Richards P. G., 2002: **Quantitative seismology**, 2nd Edition, University Science Books, Sausalito, ISBN 0-9357-0296-2

Anderson A. L. and Hampton L. D., 1980a: **Acoustics of gas-bearing sediments, 1. Background**, Journal of the Acoustical Society of America 67, 1865–1889

Anderson A. L. and Hampton L. D., 1980b: **Acoustics of gas-bearing sediments, 2. Measurements and models**, Journal of the Acoustical Society of America 67, 1890–1903

Beresnev I. A., 2006: **Theory of vibratory mobilization on nonwetting fluids entrapped in pore constrictions**, Geophysics 71, N47–N56, doi:10.1190/1.2353803

Beresnev I. A. and Johnson P. A., 1994: **Elastic-wave stimulation of oil production: A review of methods and results**, Geophysics 59, 1000–1017

Beresnev I. A., Vigil R. D., Li W. Q., Pennington W. D., Turpening R. M., Iassonov P. P. and Ewing R. P., 2005: **Elastic waves push organic fluids from reservoir rock**, Geophysical Research Letters 32, L13303, doi:10.1029/2005GL023123

Berger J., Davis P. and Ekstrom G., 2004: **Ambient Earth noise: A survey of the Global Seismographic Network**, Journal of Geophysical Research 109, B11307, doi:10.1029/2004JB003408

Berryman J. G. and Milton G. W., 1991: **Exact results for generalized Gassmann equations in composite porous media with two constituents**, Geophysics 56, 1950–1960

Biot M. A., 1962: **Mechanics of deformation and acoustic propagation in porous media**, Journal of Applied Physics 33, 1482–1498

Bonnefoy-Claudet S., Cotton F. and Bard P.-Y., 2006: **The nature of noise wavefield and its applications for site effects studies - A literature review**, Earth-Science Reviews 79, 205–227, doi:10.1016/j.earscirev.2006.07.004

Borja R. I., 2006: **On the mechanical energy and effective stress in saturated and unsaturated porous continua**, International Journal of Solids and Structures 43, 1764–1786, doi:10.1016/j.ijsolstr.2005.04.045

Bourbie T., Coussy O. and Zinszner B., 1987: **Acoustics of porous media**, Editions Technip, Paris, ISBN 2-7108-0516-2

Bradley C. R., Stephen R. A., Dorman L. M. and Orcutt J. A., 1997: **Very low frequency (0.2-10.0 Hz) seismoacoustic noise below the seafloor**, Journal of Geophysical Research 102, 11703–11718

Castellini P., Esposito E., Paone N. and Tomasini E. P., 2000: **Non-invasive measurements of damage of frescoes paintings and icon by laser scanning vibrometer: experimental results on artificial samples and real works of art**, Measurement 28, 33–45

Dangel S., Schaepman M. E., Stoll E. P., Carniel R., Barzandji O., Rode E. D. and Singer J. M., 2003: **Phenomenology of tremor-like signals observed over hydrocarbon reservoirs**, Journal of Volcanology and Geothermal Research 128, 135–158, doi:10.1016/S0377-0273(03)00251-8

Dutta N. C. and Ode H., 1979: **Attenuation and dispersion of compressional waves in fluid-filled porous rocks with partial gas saturation (White model), 1. Biot theory**, Geophysics 44, 1777–1788

Dvorkin J., Mavko G. and Nur A., 1990: **The oscillations of a viscous compressible fluid in an arbitrarily-shaped pore**, Mechanics of Materials 9, 165–179

Fetter A. L. and Walecka J. D., 1980: **Theoretical mechanics of particles and continua**, McGraw-Hill Book Company, New York, ISBN 0-0702-0658-9

Fox F. E., Curley S. R. and Larson G. S., 1955: **Phase velocity and absorption measurements in water containing air bubbles**, Journal of the Acoustical Society of America 27, 534–539

Frehner M., Schmalholz S. M., Saenger E. H. and Steeb H., 2008: **Comparison of finite difference and finite element methods for simulating two-dimensional scattering of elastic waves**, Physics of the Earth and Planetary Interiors 171, 112–121, doi:10.1016/j.pepi.2008.07.003

Frehner M., Schmalholz S. M. and Podlachikov Y., 2009: **Spectral modification of seismic waves propagating through solids exhibiting a resonance frequency: A 1-D coupled wave propagation-oscillation model**, Geophysical Journal International 176, 589–600, doi:10.1111/j.1365-246X.2008.04001.x

Gassmann F., 1951: **Über die Elastizität poröser Medien**, Vierteljahrsschrift der Naturforschenden Gesellschaft Zürich 96, 1–23

Geerstma J. and Smit D. C., 1961: **Some aspects of elastic wave propagation in fluid-saturated porous solids**, Geophysics 26, 169–181

Graf R., Schmalholz S. M., Podladchikov Y. and Saenger E. H., 2007: **Passive low frequency spectral analysis: Exploring a new field in geophysics**, World Oil January, 47–52

Graham D. R. and Higdon J. J. L., 2000a: **Oscillatory flow of droplets in capillary tubes. Part 1. Straight tubes**, Journal of Fluid Mechanics 425, 31–53

Graham D. R. and Higdon J. J. L., 2000b: **Oscillatory flow of droplets in capillary tubes. Part 2. Constricted tubes**, Journal of Fluid Mechanics 425, 55–77

Gray W. G. and Schrefler B. A., 2007: **Analysis of the solid phase stress tensor in multiphase porous media**, International Journal for Numerical and Analytical Methods in Geomechanics 31, 541–581, doi:10.1002/nag.541

Hassan W. and Nagy P. B., 1997: **Circumferential creeping waves around a fluid-filled cylindrical cavity in an elastic medium**, Journal of the Acoustical Society of America 101, 2496–2503

Higham N. J., 1996: **Accuracy and stability of numerical algorithms**, Society for Industrial and Applied Mathematics, Philadelphia, ISBN 0-8987-1355-2

Hilpert M., 2007: **Capillarity-induced resonance of blobs in porous media: Analytical solutions, Lattice-Boltzmann modeling, and blob mobilization**, Journal of Colloid and Interface Science 309, 493–504, doi:10.1016/j.jcis.2006.11.052

Hilpert M., Jirka G. H. and Plate E. J., 2000: **Capillarity-induced resonance of oil blobs in capillary tubes and porous media**, Geophysics 65, 874–883

Holzner R., Eschle P., Dangel S., Frehner M., Narayanan C. and Lakehal D., 2009: **Hydrocarbon microtremors interpreted as nonlinear oscillations driven by oceanic background waves**, Communications in nonlinear science and numerical simulation 14, 160–173, doi:10.1016/j.cnsns.2007.06.013

Iassonov P. P. and Beresnev I. A., 2003: **A model for enhanced fluid percolation in porous media by application of low-frequency elastic waves**, Journal of Geophysical Research 108, 2138, doi:10.1029/2001JB000683

Ida N. and Wang J. S., 1996: **Models for microwave nondestructive testing of materials**, in Nondestructive Characterization of Materials vii, Pts 1 and 2, Volume 210- of Materials Science Forum, pages 93–100

Ionescu D. C. and Igel H., 2003: **Transparent boundary conditions for wave propagation on unbounded domains**, in Computational Sicence - ICCS 2003, Pt iii, Proceedings, Volume 2659 of Lecture Notes In Computer Science, pages 807–816

Lambert M.-A., Schmalholz S. M., Saenger E. H. and Steiner B., 2008: **Low-frequency microtremor anomalies at an oil and gas field in Voitsdorf, Austria**, Geophysical Prospecting In Press, doi:10.1111/j.1365-2478.2008.00734.x

Landau L. D. and Lifschitz E. M., 1997: **Mechanik**, Volume 1 of Lehrbuch der theoretischen Physik, 14th Edition, Harri Deutsch, Thun, ISBN 3-8171-1326-9

Li W. Q., Vigil R. D., Beresnev I. A., Iassonov P. and Ewing R., 2005: **Vibration-induced mobilization of trapped oil ganglia in porous media: Experimental validation of a capillary-physics mechanism**, Journal of Colloid and Interface Science 289, 193–199, doi:10.1016/j.jcis.2005.03.067

Lindsay R. B., 1960: **Mechanical radiation**, International series in pure and applied physics, McGraw-Hill, New York, ISBN 0-0703-7844-0

Lo W.-C. and Sposito G., 2005: **Wave propagation through elastic porous media containing two immiscible fluids**, Water Resources Research 41, W2025, doi:10.1029/2004WR003162

Mavko G., Mukerji T. and Dvorkin J., 2003: **The rock physics handbook: Tools for seismic analysis in porous media**, Cambridge University Press, Cambridge, ISBN 0-5215-4344-4

Meyer E., Brendel K. and Tamm K., 1958: **Pulsation oscillations of cavities in rubber**, Journal of the Acoustical Society of America 30, 1116–1124

Peterson J., 1993: **Observations and modeling of seismic background noise**, U.S. Geological Survey Open File Report pages 93–322

Pride S. R., Flekkoy E. G. and Aursjo O., 2008: **Seismic stimulation for enhanced oil recovery**, Geophysics 73, O23–O35, doi:10.1190/1.2968090

Saenger E. H., Ciz R., Krüger O. S., Schmalholz S. M., Gurevich B. and Shapiro S. A., 2007: **Finite-difference modeling of wave propagation on microscale: A snapshot of the work in progress**, Geophysics 72, SM293–SM300, doi:10.1190/1.2753552

Santos J. E., Douglas J., Corbero J. and Lovera O. M., 1990: **A model for wave-propagation in a porous-medium saturated by a two-phase fluid**, Journal of the Acoustical Society of America 87, 1439–1448

Schultz T., Cattafesta L. N. and Sheplak M., 2006: **Modal decomposition method for acoustic impedance testing in square ducts**, Journal of the Acoustical Society of America 120, 3750–3758, doi:10.1121/1.2360423

Silberman E., 1957: **Sound velocity and attenuation in bubbly mixtures measured in standing wave tubes**, Journal of the Acoustical Society of America 29, 925–933

Smeulders D. M. J. and Van Dongen M. E. H., 1997: **Wave propagation in porous media containing a dilute gas-liquid mixture: Theory and experiments**, Journal of Fluid Mechanics 343, 351–373

Szabo I., 1985: **Höhere technische Mechanik**, 5th Edition, Springer-Verlag, Berlin, ISBN 3-5401-5007-2

Toms J., Müller T. M., Ciz R. and Gurevich B., 2006: **Comparative review of theoretical models for elastic wave attenuation and dispersion in partially saturated rocks**, Soil Dynamics and Earthquake Engineering 26, 548–565, doi: 10.1016/j.soildyn.2006.01.008

Tuncay K. and Corapcioglu M. Y., 1996: **Body waves in poroelastic media saturated by two immiscible fluids**, Journal of Geophysical Research 101, 25149–25159

Urquizu M. and Correig A. M., 2004: **On the equivalence between stratified media and oscillators**, Geophysical Journal International 157, 245–250, doi:10.1111/j. 1365-246X.2004.02167.x

Virieux J., 1986: **P-Sv-wave propagation in heterogeneous media: Velocity-stress finite-difference method**, Geophysics 51, 889–901

Walker D., 2008: **Recent developments in low frequency spectral analysis of passive seismic data**, First Break 26, 65–72

Wei C. F. and Muraleetharan K. K., 2002: **A continuum theory of porous media saturated by multiple immiscible fluids: II. Lagrangian description and variational structure**, International Journal of Engineering Science 40, 1835–1854

Werby M. F. and Gaunaurd G. C., 1989: **Broadside resonance scattering from elastic spheroids**, IEEE Journal of Oceanic Engineering 14, 400–406

Werby M. F. and Gaunaurd G. C., 1990: **Resonance scattering from submerged elastic spheroids of high aspect ratios and its three-dimensional interpretation**, Journal of the Acoustical Society of America 88, 951–960

White J. E., 1975: **Computed seismic speeds and attenuation in rocks with partial gas saturation**, Geophysics 40, 224–232

White J. E., Mikhaylova N. G. and Lyakhovitsky F. M., 1975: **Low-frequency seismic-waves in fluid-saturated layered rocks**, Izvestija Academy of Science USSR, Physics of the Solid Earth 11, 654–659

5 Discussion

From the presented doctoral thesis a number of discussion points can be adressed, mainly concerning two aspects:

- The physical interpretations of the presented phenomena in fluid–rock systems.
- The numerical challenges that are faced for simulating such systems.

These two aspects are covered separately in the following two sections.

5.1. Discussion concerning physics

In this thesis two wave propagation phenomena were investigated, the Stoneley guided waves (SGW, Chapter 3) and the propagation of seismic waves through a medium exhibiting internal oscillations (Chapter 4). Both phenomena occur in porous and fractured rocks. Scattering used for the numerical accuracy study in Chapter 2 also occurs in the same types of rocks. All of these phenomena are not considered in existing effective medium or mixture models, such as the Biot theory (Biot, 1962), patchy–saturation models (White, 1975; White *et al.*, 1975; Dutta and Ode, 1979) or the Hudson model (Hudson, 1980, 1981). However, these phenomena can be of importance in porous and fractured rocks. For example, Saenger *et al.* (2007) presented two poroelastic wave propagation simulations, one using Biot's equations and one fully resolving the pore structures in three dimensions and therefore also including scattering. The comparison showed that scattering plays a significant role because it attenuates seismic waves. Also, Korneev (2008) argues that incorporating SGW–related effects into poroelastic theories "might be critically important for wave propagation effects in fractured reservoirs". The effects described in this thesis are difficult to generalize and incorporate into existing models using effective parameters. However, when dealing with porous and fractured rocks, one has to bear in mind that additional phenomena exist that are not included in the standard theories but may have an important effect.

The studied reflection coefficient of SGWs at the tip of a crack is strong enough (between 43 % and almost 100 %) that a SGW can propagate several times back and forth along a finite crack. This leads to a resonant behavior of SGWs. The fundamental frequency of such a resonance can be relatively low, for example between 46 Hz and 61 Hz for the material parameters in Chapter 3 and a 10 m long fracture (but can be lower for different material parameters and longer fractures). An object, at which seismic waves are scattered, can also exhibit a resonance due to the periodicity of the circumferential waves and the internal reflections (e.g. Hassan and Nagy, 1997; Liu *et al.*, 2000, also Appendix D). These types of resonant behavior may act as alternative arguments for the coupled wave propagation–oscillation model presented in Chapter 4.

In Chapter 4 one particular resonance effect, i.e. oscillations on the pore–level due to surface tension, was coupled with the wave–equation. The resulting medium exhibiting internal oscillations temporarily modifies the frequency content of waves when they propagate through this medium. This observation also applies to any medium that exhibits an internal resonant behavior, e.g. a porous or fractured rock. However, this is only true if the propagating wave already contains some energy at the resonance frequency of the internal oscillations. As shown in Chapter 4 the wave looses energy at the resonance frequency when the internal oscillations are initiated. Later, when the internal oscillations continuously radiate P– and S–waves into the surrounding rock, the resonance frequency can be measured away from the porous or fractured rock. How the radiation patterns of P– and S–waves look like was shown in Chapter 3 for the case of SGWs that are scattered at the tip of a crack. In real rocks a wide range of resonance frequencies is expected because cracks have different lengths, are filled with different fluids and pore structures are complex. This would lead to a continuous transfer of energy between the internal oscillations and the wavefield. This thesis just presents the beginning of understanding the complicated interplay between seismic wave propagation and fluids in a porous or fractured rock that can exhibit a resonance frequency. More realistic models need to be developed to better understand the importance of internal oscillations, such as resonant SGWs, resonant scattering or resonance du to surface tension.

5.2. Discussion concerning numerics

This thesis has shown that the finite element method (FEM) has great potential for simulating wave propagation in heterogeneous media. As a non–standard technique it is often wrongfully thought to be linked to an implicit time integration method and is therefore put down as too computationally expensive for wave propagation simulations. However, the FEM used in this thesis is exclusively used for spatial discretization and does not influence the time integration. Both implicit and explicit time integration can be used, which makes the FEM very flexible and well suitable for wave propagation simulations. The FEM used for time–integration in parts of Chapter 2 is mathematically separated from the space–FEM and only represents one possibility for an implicit time–integration method.

Material contrasts lead to infinite values for the spatial derivatives of material parameters in the governing equations, such as bulk or shear modulus (Equations 2.1, 3.10 and A.15). The main difference between the FEM and the FDM used in this thesis is the approach to remove the spatial derivatives from material parameters. The FDM introduces stress as a new unknown that has to be determined with additional first–order equations (see Appendix B for details). This leads to a reduction of the spatial derivatives in the governing equations by one order. The resulting first–order equations are solved on discrete points where the material parameters are defined. On the other hand, the FEM uses an integral formulation of the governing equations (see Appendix C for details). Integration by parts reduces the spatial derivatives by one order. The resulting integral equations are solved element–wise. These two different formulations also lead to two completely different numerical meshes. The FEM uses an unstructured triangular mesh while the FDM uses a rectangular grid. Therefore, especially for heterogeneous media, the FEM has some major advantages over the FDM. These are:

- An unstructured mesh is very flexible because it can resolve fine geometrical structures very accurately without the need of a fine resolution elsewhere in the model domain. For example, the pore walls in a porous rock can be resolved with a high resolution while the resolution inside the pores and the grains can be much

coarser. This way, an unstructured mesh saves many unnecessary numerical points compared to a rectangular grid.

- No matter how fine the FDM–grid is, it can not be avoided that objects are approximated in a staircase–like way because the grid is always rectangular. This leads to numerical inaccuracies. On the other hand, the unstructured triangular FEM–mesh can accurately follow any geometry.

- Strong material contrasts are handled by the FEM whithout problems while the FDM can cause numerical inaccuracies at material boundaries. The first–order spatial derivatives of the FDM–formulation have to be calculated across material contrasts, which can cause numerical inaccuracies. The integral equations used for the FEM are solved element–wise, which allows neighboring elements to have hugely different material properties without introducing any numerical inaccuracies.

The first point will be even more important in three–dimensional simulations where the number of numerical points increases more rapidly. For one–dimensional simulations (e.g. Chapter 4) the listed advantages become less important and the FEM and the FDM work equally well for wave propagation simulations. Using the FEM also has some disadvantages compared to the FDM. However, they are considered as of minor importance in this thesis. The disadvantages are:

- The implementation of the FEM is somewhat more difficult than that of the FDM. For many applications the FDM is accurate enough (e.g. one–dimensional problems or setups without strong material contrasts) and the effort of a FEM–implementation is not worthwhile.

- The FEM always requires calculating the system matrices, no matter if an implicit or explicit time–integration method is used. This is done only once before the time–loop starts. However, it takes some calculation time. On the other hand, the FDM hardly needs any calculations before the time–loop.

- The unstructured triangular mesh makes it more difficult for plotting results compared to rectangular grids. Simple plotting routines in for example MATLAB do not work for unstructured meshes. Also, plotting results along profile lines is not straightforward. However, when the profile lines are known before the start of a simulation, the software Triangle used for generating the FEM–meshes in this thesis is flexible enough to incorporate them as a part of the unstructured mesh.

One particular situation where an unstructured mesh is of no advantage is when measured material distributions are used in wave propagation simulations. For example, digitized microtomographic images of real porous rocks are used for creating velocity models for seismic wave propagation simulations on the microscale (e.g. Saenger *et al.*, 2004) or interpreted seismic velocity cubes from three–dimensional seismic surveys are used for the simulation of waves in the subsurface (e.g. Lambert *et al.*, 2008; Steiner *et al.*, 2008). Such measurements of material property distributions are usually provided in grid–like formats. It does not make sense to use unstructured numerical meshes in such cases because the given data resolution can not be enhanced. However, the FEM can still be advantageous over the FDM because, even though on a rectangular grid, strong material contrast are approximated more precisely with the element–wise formulation of the FEM.

Optimizing calculation time was not a major subject of this thesis. It is clear that all numerical codes can be made faster by using for example another programming language than MATLAB, faster implicit solvers or an optimized matrix–assembly algorithm (e.g. Dabrowski *et al.*, 2008). However, choosing between an implict and an explicit time–integration method is of major importance when using the FEM and it depends on the problem under study which one is better. The model setup with a thin fracture presented in Chapter 3 requires a very high spatial resolution. Therefore, the explicit time increment, which is a function of the shortest distance between two numerical points, becomes very small. Also, the model includes viscous fluids, which leads to dispersion problems (see Chapter 3 for a discussion). In such situations an implicit time–integration method is the best choice. However, the implicit time increment has to be choosen small enough to obtain accurate results. In other situations, such as in Chapter 2 where no viscous fluids are involved and the numerical resolution does not have to be extraordinarily high, an explicit time–integration is the better choice and even makes the simulation faster.

5.3. Broader implications

One example of heterogeneous and fractured rocks containing fluids is in volcanic areas and below hydrothermal fields. Magma or hydrothermal water opening and migrating along cracks can trigger microearthquakes and initiate the resonance effects in the rocks discussed above. Resonant SGWs have drawn particular attention as a possible explanation for low–frequency volcanic tremor (e.g. Aki *et al.*, 1977; Chouet, 1988, 1996). The narrow frequency band of the tremor–signal was quickly realized but a reasonable mechanism for its explanation has only been found when the resonant behavior of SGWs was discovered. However, other oscillatory phenomena may play a role in volcanic tremor–signals, such as resonant scattering of magma or fluid pockets or the resonance due to surface tension effects between different fluids and gas bubbles.

Another example of fractured and porous media containing fluids is reservoir rocks for hydrocarbons. The network of fractures and the porosity contributes significantly to the permeability of a reservoir. In recent years, with increasing sensor sensitivity, similar low–frequency signals to volcanic tremor have been observed above hydrocarbon reservoirs, often referred to as hydrocarbon microtremor (Dangel *et al.*, 2003; Holzner *et al.*, 2005; Bloch and Akrawi, 2006; Suntsov *et al.*, 2006; Graf *et al.*, 2007; Walker, 2008; Holzner *et al.*, 2009). Steiner *et al.* (2008) used passive seismic surface measurements of hydrocarbon microtremor and numerically back–propagated them into the subsurface to detect potential source areas in the subsurface. Lambert *et al.* (2008) used similar surface measurements to identify modifications of the wavefield in the frequency domain above known hydrocarbon reservoirs. Saenger *et al.* (2009) presented an extensive hydrocarbon microtremor survey over a gas field in Mexico where a good agreement between interpreted surface attributes of the measurements and known gas intervalls was found. However, all of these studies did not explain the mechanism causing hydrocarbon microtremor. They only assumed that the hydrocarbon reservoir modifies the wavefield in the low–frequency range in a certain way that makes it detectable.

Quintal *et al.* (2009) showed that a porous partially saturated reservoir exhibits a strongly frequency dependent reflectivity for elastic body waves because of attenuation within the reservoir caused by wave–induced fluid flow between different saturation–domains. Such a mechanism may cause the frequency dependent modification of the wavefield necessary

to explain hydrocarbon microtremor. Resonance effects, such as oscillations on the pore–level due to surface tension, resonant SGWs or resonant scattering may also explain the harmonic nature of hydrocarbon microtremor. In any case, a final explanation for the cause of hydrocarbon microtremor can not be given at this point and further research into all mentioned potential mechanisms, and also others, has to be conducted.

Also in active seismic surveys (i.e. seismic survey with an active man–made source) frequency dependent phenomena have been observed. For example Korneev *et al.* (2004) desribed a frequency dependent reflection coefficient in the low–frequency range for a seismic survey above a fluid–saturated reservoir. Effects described by Quintal *et al.* (2009), resonance effects or both may play a role in such observed phenomena.

References

Aki K., Fehler M. and Das S., 1977: **Source mechanism of volcanic tremor: Fluid-driven crack models and their application to the 1963 Kilauea eruption**, Journal of Volcanology and Geothermal Research 2, 259–287

Biot M. A., 1962: **Mechanics of deformation and acoustic propagation in porous media**, Journal of Applied Physics 33, 1482–1498

Bloch G. and Akrawi K., 2006: **Application of low frequency passive seismic surveys in ADCO, UAE**, in EAGE Workshop Passive Seismic, Dubai, United Arab Emirates

Chouet B., 1988: **Resonance of a fluid-driven crack: Radiation properties and implications for the source of long-period events and harmonic tremor**, Journal of Geophysical Research 93, 4375–4400

Chouet B. A., 1996: **Long-period volcano seismicity: Its source and use in eruption forecasting**, Nature 380, 309–316

Dabrowski M., Krotkiewski M. and Schmid D. W., 2008: **MILAMIN: MATLAB-based finite element method solver for large problems**, Geochemistry Geophysics Geosystems 9, Q04030, doi:10.1029/2007GC001719

Dangel S., Schaepman M. E., Stoll E. P., Carniel R., Barzandji O., Rode E. D. and Singer J. M., 2003: **Phenomenology of tremor-like signals observed over hydrocarbon reservoirs**, Journal of Volcanology and Geothermal Research 128, 135–158, doi: 10.1016/S0377-0273(03)00251-8

Dutta N. C. and Ode H., 1979: **Attenuation and dispersion of compressional waves in fluid-filled porous rocks with partial gas saturation (White model), 1. Biot theory**, Geophysics 44, 1777–1788

Graf R., Schmalholz S. M., Podladchikov Y. and Saenger E. H., 2007: **Passive low frequency spectral analysis: Exploring a new field in geophysics**, World Oil January, 47–52

Hassan W. and Nagy P. B., 1997: **Circumferential creeping waves around a fluid-filled cylindrical cavity in an elastic medium**, Journal of the Acoustical Society of America 101, 2496–2503

Holzner R., Eschle P., Zürcher H., Lambert M., Graf R., Dangel S. and Meier P. F., 2005: **Applying microtremor analysis to identify hydrocarbon reservoirs**, First Break 23, 41–46

Holzner R., Eschle P., Dangel S., Frehner M., Narayanan C. and Lakehal D., 2009: **Hydrocarbon microtremors interpreted as nonlinear oscillations driven by oceanic background waves**, Communications in nonlinear science and numerical simulation 14, 160–173, doi:10.1016/j.cnsns.2007.06.013

Hudson J. A., 1980: **Overall properties of a cracked solid**, Mathematical Proceedings of the Cambridge Philosophical Society 88, 371–384

Hudson J. A., 1981: **Wave speeds and attenuation of elastic-waves in material containing cracks**, Geophysical Journal of the Royal Astronomical Society 64, 133–150

Korneev V., 2008: **Slow waves in fractures filled with viscous fluid**, Geophysics 73, N1–N7, doi:10.1190/1.2802174

Korneev V. A., Goloshubin G. M., Daley T. M. and Silin D. B., 2004: **Seismic low-frequency effects in monitoring fluid-saturated reservoirs**, Geophysics 69, 522–532, doi:10.1190/1.1707072

Lambert M.-A., Schmalholz S. M., Saenger E. H. and Steiner B., 2008: **Low-frequency microtremor anomalies at an oil and gas field in Voitsdorf, Austria**, Geophysical Prospecting In Press, doi:10.1111/j.1365-2478.2008.00734.x

Liu Y. B., Wu R.-S. and Ying C. F., 2000: **Scattering of elastic waves by an elastic or viscoelastic cylinder**, Geophysical Journal International 142, 439–460

Quintal B., Schmalholz S. M. and Podladchikov Y. Y., 2009: **Low-frequency reflections from a thin layer with high attenuation caused by interlayer flow**, Geophysics 74, N15–N23, doi:10.1190/1.3026620

Saenger E. H., Kruger O. S. and Shapiro S. A., 2004: **Numerical considerations of fluid effects on wave propagation: Influence of the tortuosity**, Geophysical Research Letters 31, L21613, doi:10.1029/2004GL020970, l21613

Saenger E. H., Ciz R., Krüger O. S., Schmalholz S. M., Gurevich B. and Shapiro S. A., 2007: **Finite-difference modeling of wave propagation on microscale: A snapshot of the work in progress**, Geophysics 72, SM293–SM300, doi:10.1190/1.2753552

Saenger E. H., Schmalholz S. M., Lambert M., Nguyen T. T., Torres A., Metzger S., Habiger R., Rentsch S. and Mendez-Hernandez E., 2009: **A passive seismic survey over a gas field: Analysis of low-frequency anomalies**, Geophysics 74, doi: 10.1190/1.3078402

Steiner B., Saenger E. H. and Schmalholz S. M., 2008: **Time reverse modeling of passive seismic measurements**, Geophysical Research Letters 35, L03307, doi:10.1029/2007GL032097

Suntsov A. E., Aroutunov S. L., Mekhnin A. M. and Meltchouk B. Y., 2006: **Passive infra-frequency microseismic technology - Experience and problems of practical use**, in EAGE Workshop Passive Seismic, Dubai, United Arab Emirates

Walker D., 2008: **Recent developments in low frequency spectral analysis of passive seismic data**, First Break 26, 65–72

White J. E., 1975: **Computed seismic speeds and attenuation in rocks with partial gas saturation**, Geophysics 40, 224–232

White J. E., Mikhaylova N. G. and Lyakhovitsky F. M., 1975: **Low-frequency seismic-waves in fluid-saturated layered rocks**, Izvestija Academy of Science USSR, Physics of the Solid Earth 11, 654–659

6 Conclusions

In porous or fractured rocks a number of multiscale wave propagation phenomena can occur, such as Stoneley guided waves, oscillations on the pore–level or scattering at heterogeneities. They are multiscale because seismic wave lengths can be orders of magnitude larger than heterogeneities, such as pores or fractures, or they can be of the same order as heterogeneities, such as hydrocarbon reservoirs. Analytical solutions are limited to simple geometries and often require advanced numerical calculations to solve for example analytical integral equations. Therefore, numerical simulations are a necessary tool to gain insight into multiscale wave propagation phenomena in fluid–rock systems.

For numerical simulations two different approaches may be followed. 1) Effective medium and mixture theories incorporate the effects of small scale processes approximatively into wave propagation models with effective parameters. 2) Direct simulations resolve small scale heterogeneities and directly model their effects. For direct numerical simulations of multiscale problems the finite element method is a well suitable technique because it can accurately resolve small scale heterogeneities with the unstructured numerical mesh.

The reflection of Stoneley guided waves at the tip of a crack is strong enough that a Stoneley guided wave can propagate several times back and forth along a finite crack and develop a resonance. The reflection coefficient depends on the fluid filling the crack and on the crack geometry. The part of the Stoneley guided wave not reflected at the crack tip is scattered and emitted into the surrounding rock as P– and S–waves. This emission makes detecting the resonating Stoneley guided wave possible away from the crack.

Resonance effects in porous or fractured rocks, such as resonant Stoneley guided waves or oscillations on the pore–level, introduce velocity dispersion and temporarily modify the frequency content of seismic waves because energy is transferred between resonators and seismic waves. One has to be aware that such effects are commonly not included in continuum models using effective material parameters. More elaborate models need to be investigated for understanding the importance of internal resonance effects in porous or fractured rocks.

APPENDICES

Appendix A
Governing equations for two–dimensional elastic and visco–acoustic deformation

For wave propagation phenomena discussed in Chapters 2 and 3 a purely linear elastic surrounding medium in two dimensions is considered. The inclusion in Chapter 2 and cracks in parts of Chapter 3 are filled with an inviscid gas or fluid with a shear modulus μ equal to 0. Some cracks considered in Chapter 3 are filled with a viscous fluid. There, the shear deformation is controlled by the shear viscosity η while the elastic shear modulus μ is equal to 0. This appendix describes the governing equations of the materials used in Chapters 2 and 3.

The symbols in this appendix may differ from the symbols used in Chapters 2 and 3, especially the use of symbols ˜ and ˘ on top of some variables.

The equations presented in this appendix can be found in many textbooks, e.g. Love (1944), Lindsay (1960), Achenbach (1973), Aki and Richards (2002), Shames and Cozzarelli (1997) or Pujol (2003). Not many further references are given in the following.

A.1. Stess and strain

The homogeneous two–dimensional state of deformation of a small volume of material is described by the strain vector $\boldsymbol{\varepsilon}$,

$$\boldsymbol{\varepsilon} = \begin{Bmatrix} \varepsilon_{xx} \\ \varepsilon_{yy} \\ \gamma_{xy} \end{Bmatrix} = \begin{Bmatrix} \frac{\partial u_x}{\partial x} \\ \frac{\partial u_y}{\partial y} \\ \frac{\partial u_x}{\partial y} + \frac{\partial u_y}{\partial x} \end{Bmatrix}. \tag{A.1}$$

The components ε_{xx} and ε_{yy} are the normal components of strain in x– and y–direction, respectively, and γ_{xy} is the shear strain, also referred to as the engineering shear strain. Displacements u_x and u_y are components in x– and y–direction of the total displacement field, respectively. The strain vector $\boldsymbol{\varepsilon}$ can be decomposed into a bulk (i.e. volumetric) part and a deviatoric (i.e. shear) part. The bulk part Θ is also called cubical dilatation and is

$$\Theta = \varepsilon_{xx} + \varepsilon_{yy}. \tag{A.2}$$

The deviatoric part $\mathbf{e}$ is

$$\mathbf{e} = \begin{Bmatrix} e_{xx} \\ e_{yy} \\ g_{xy} \end{Bmatrix} = \begin{Bmatrix} \varepsilon_{xx} - \frac{1}{3}\Theta \\ \varepsilon_{yy} - \frac{1}{3}\Theta \\ \gamma_{xy} \end{Bmatrix}. \tag{A.3}$$

The homogeneous two–dimensional state of stress of a small volume of material is described by the stress vector $\boldsymbol{\sigma}$, which can also be decomposed into a bulk (i.e. volumetric) part p and a deviatoric (i.e. shear) part $\mathbf{s}$:

$$\underbrace{\begin{Bmatrix} \sigma_{xx} \\ \sigma_{yy} \\ \sigma_{xy} \end{Bmatrix}}_{\boldsymbol{\sigma}} = \begin{Bmatrix} -p \\ -p \\ 0 \end{Bmatrix} + \underbrace{\begin{Bmatrix} s_{xx} \\ s_{yy} \\ s_{xy} \end{Bmatrix}}_{\mathbf{s}}, \tag{A.4}$$

where p is pressure. Compressive stresses are defined to be negative. Because compressive pressure is defined to be positive, the minus sign in front of the pressure p becomes necessary.

A.2. Conservation equations

The fundamental mechanical conservation equations governing the two–dimensional deformation of a material are:

1. Conservation of linear momentum
2. Conservation of angular momentum
3. Conservation of mass

It can be shown that angular momentum is conserved when the stress tensor is symmetric. In two dimensions this is written as

$$\sigma_{xy} = \sigma_{yx}. \tag{A.5}$$

This is the well–known complementary property of shear. It is explained in in many textbooks (e.g. Shames and Cozzarelli, 1997) and is not further discussed here. In Equation A.4 symmetry of the stress tensor was already assumed. Conservation of linear momentum in two dimensions takes the following form:

$$\rho \ddot{u}_x = \frac{\partial \sigma_{xx}}{\partial x} + \frac{\partial \sigma_{xy}}{\partial y}, \tag{A.6}$$

$$\rho \ddot{u}_y = \frac{\partial \sigma_{xy}}{\partial x} + \frac{\partial \sigma_{yy}}{\partial y}, \tag{A.7}$$

where ρ is the mass density of the material under consideration and $\ddot{u}_x$ and $\ddot{u}_y$ are the second time derivatives of the displacement components in x– and y–direction, respectively (i.e. acceleration). Hereby, the two dots denote the second time derivative (one dot denotes the first time derivative). Note that in Equations A.6 and A.7 gravity is ignored. Equations A.6 and A.7 represent two equations for the two unknowns u_x and u_y. Conservation of mass of a compressible medium in two–dimensions is

$$\rho = \frac{\rho_0}{1 + \Theta} \approx \rho_0, \tag{A.8}$$

where ρ_0 is the mass density in the undeformed state of the material and ρ is the mass density in a deformed state. The cubical dilatation Θ is assumed to be small compared to unity in Equation A.8. Therefore, density ρ is constant over time. However, this does not mean that the material is incompressible. The compressibility will have an effect in the constitutive equations.

A.3. Constitutive equations

To be able to solve equations A.6 and A.7 a relation between the stress components and the displacement components has to be defined, the so–called constitutive equations. The constitutive equations describe the material behavior under loading and they are separated into a bulk (i.e. volumetric) part and a deviatoric (i.e. shear) part. The bulk deformation of all materials under consideration is linear elastic compressible and is described as

$$- p = K\Theta, \tag{A.9}$$

The elastic material parameter K is the so–called bulk modulus. The deviatoric part of deformation is defined differently for different materials. It is either elastic, i.e.

$$\begin{Bmatrix} s_{xx} \\ s_{yy} \\ s_{xy} \end{Bmatrix} = \begin{bmatrix} 2\mu & 0 & 0 \\ 0 & 2\mu & 0 \\ 0 & & \mu \end{bmatrix} \begin{Bmatrix} e_{xx} \\ e_{yy} \\ g_{xy} \end{Bmatrix}, \tag{A.10}$$

or viscous, i.e.

$$\begin{Bmatrix} s_{xx} \\ s_{yy} \\ s_{xy} \end{Bmatrix} = \begin{bmatrix} 2\eta & 0 & 0 \\ 0 & 2\eta & 0 \\ 0 & & \eta \end{bmatrix} \underbrace{\begin{Bmatrix} \dot{e}_{xx} \\ \dot{e}_{yy} \\ \dot{g}_{xy} \end{Bmatrix}}_{\dot{\mathbf{e}}}, \tag{A.11}$$

where μ is the elastic shear modulus and η is the shear viscosity. The deviatoric strain rate vector $\dot{\mathbf{e}}$ is the time derivative of the deviatoric strain vector $\mathbf{e}$. Two total constitutive equations can be derived. Combining Equations A.2, A.3, A.4, A.9 and A.10 the total constitutive equation describing the behavior of a purely elastic material can be derived:

$$\begin{Bmatrix} \sigma_{xx} \\ \sigma_{yy} \\ \sigma_{xy} \end{Bmatrix} = \begin{bmatrix} K + \frac{4}{3}\mu & K - \frac{2}{3}\mu & 0 \\ K - \frac{2}{3}\mu & K + \frac{4}{3}\mu & 0 \\ 0 & & \mu \end{bmatrix} \begin{Bmatrix} \frac{\partial u_x}{\partial x} \\ \frac{\partial u_y}{\partial y} \\ \frac{\partial u_x}{\partial y} + \frac{\partial u_y}{\partial x} \end{Bmatrix}. \tag{A.12}$$

Combining Equations A.2, A.3, A.4, A.9 and A.11 the total constitutive equation describing the behavior of a visco–acoustic material can be derived:

$$\begin{Bmatrix} \sigma_{xx} \\ \sigma_{yy} \\ \sigma_{xy} \end{Bmatrix} = \begin{bmatrix} K & K & 0 \\ K & K & 0 \\ 0 & & 0 \end{bmatrix} \begin{Bmatrix} \frac{\partial u_x}{\partial x} \\ \frac{\partial u_y}{\partial y} \\ \frac{\partial u_x}{\partial y} + \frac{\partial u_y}{\partial x} \end{Bmatrix} + \begin{bmatrix} \frac{4}{3}\eta & -\frac{2}{3}\eta & 0 \\ -\frac{2}{3}\eta & \frac{4}{3}\eta & 0 \\ 0 & & \eta \end{bmatrix} \begin{Bmatrix} \frac{\partial \dot{u}_x}{\partial x} \\ \frac{\partial \dot{u}_x}{\partial y} \\ \frac{\partial \dot{u}_x}{\partial y} + \frac{\partial \dot{u}_x}{\partial x} \end{Bmatrix}. \tag{A.13}$$

Equation A.12 describes the behavior of an elastic solid. A viscous fluid (parts of Chapter 3) is described by Equation A.13 (visco–acoustic medium). Here, the elastic shear modulus is implicitly set to zero, but a shear viscosity is applied. An inviscid fluid (Chapter 2 and parts of 3) is also described by Equation A.13 but using a shear viscosity η equal to zero (acoustic medium). Using the elastic constitutive matrix $\mathbf{D}_{el}$ and the viscous constitutive matrix $\mathbf{D}_{visc}$, Equations A.12 and A.13 can be expressed more generally as

$$\boldsymbol{\sigma} = \mathbf{D}_{el}\boldsymbol{\varepsilon} + \mathbf{D}_{visc}\dot{\boldsymbol{\varepsilon}}. \tag{A.14}$$

A.4. Total equations of motion

Substituting the constitutive equations (Equation A.14) into the equations of conservation of linear momentum (Equations A.6 and A.7) leads to the final equations of motion:

$$\rho \begin{Bmatrix} \ddot{u}_x \\ \ddot{u}_y \end{Bmatrix} = \begin{bmatrix} \frac{\partial}{\partial x} & 0 & \frac{\partial}{\partial y} \\ 0 & \frac{\partial}{\partial y} & \frac{\partial}{\partial x} \end{bmatrix} \mathbf{D}_{el} \begin{bmatrix} \frac{\partial}{\partial x} & 0 \\ 0 & \frac{\partial}{\partial y} \\ \frac{\partial}{\partial y} & \frac{\partial}{\partial x} \end{bmatrix} \begin{Bmatrix} u_x \\ u_y \end{Bmatrix} + \begin{bmatrix} \frac{\partial}{\partial x} & 0 & \frac{\partial}{\partial y} \\ 0 & \frac{\partial}{\partial y} & \frac{\partial}{\partial x} \end{bmatrix} \mathbf{D}_{visc} \begin{bmatrix} \frac{\partial}{\partial x} & 0 \\ 0 & \frac{\partial}{\partial y} \\ \frac{\partial}{\partial y} & \frac{\partial}{\partial x} \end{bmatrix} \begin{Bmatrix} \dot{u}_x \\ \dot{u}_y \end{Bmatrix}. \tag{A.15}$$

Using

$$\tilde{\mathbf{u}} = \begin{Bmatrix} u_x \\ u_y \end{Bmatrix}, \tag{A.16}$$

$$\tilde{\mathbf{B}} = \begin{bmatrix} \frac{\partial}{\partial x} & 0 \\ 0 & \frac{\partial}{\partial y} \\ \frac{\partial}{\partial y} & \frac{\partial}{\partial x} \end{bmatrix}, \tag{A.17}$$

Equation A.15 can be written in a simplified matrix notation, with supterscript T denoting the transpose of a matrix:

$$\rho\ddot{\tilde{\mathbf{u}}} = \tilde{\mathbf{B}}^T \mathbf{D}_{el}\tilde{\mathbf{B}}\tilde{\mathbf{u}} + \tilde{\mathbf{B}}^T \mathbf{D}_{visc}\tilde{\mathbf{B}}\dot{\tilde{\mathbf{u}}}. \tag{A.18}$$

References

Achenbach J. D., 1973: **Wave propagation in elastic solids**, Volume 16 of North-Holland series in Applied Mathematics and Mechanics, North-Holland Publishing Company, Amsterdam, ISBN 0-7204-2367-8

Aki K. and Richards P. G., 2002: **Quantitative seismology**, 2nd Edition, University Science Books, Sausalito, ISBN 0-9357-0296-2

Lindsay R. B., 1960: **Mechanical radiation**, International series in pure and applied physics, McGraw-Hill, New York, ISBN 0-0703-7844-0

Love A. E. H., 1944: **A treatise on the mathematical theory of elasticity**, 4th Edition, Dover books on physics and chemistry, Dover Publications, New York, ISBN 0-4866-0174-9

Pujol J. A., 2003: **Elastic wave propagation and generation in seismology**, Cambridge University Press, Cambridge

Shames I. H. and Cozzarelli F. A., 1997: **Elastic and inelastic stress analysis**, revised printing Edition, Taylor and Francis, Washington

Appendix B
Finite difference method

The finite difference method used for spatial discretization of the governing equations in Chapter 2 is here explained in more details. Only fully elastic media and inviscid fluids are modeled with the finite difference method. Therefore, only Equation A.12 is considered here. A velocity–stress finite difference formulation is used. Equations A.6, A.7 and A.12 are reformulated in the following way:

$$\dot{v}_x = \frac{1}{\rho}\frac{\partial \sigma_{xx}}{\partial x} + \frac{1}{\rho}\frac{\partial \sigma_{xy}}{\partial y}, \tag{B.1}$$

$$\dot{v}_y = \frac{1}{\rho}\frac{\partial \sigma_{xy}}{\partial x} + \frac{1}{\rho}\frac{\partial \sigma_{yy}}{\partial y}, \tag{B.2}$$

$$\dot{\sigma}_{xx} = \left(K + \frac{4}{3}\mu\right)\frac{\partial v_x}{\partial x} + \left(K - \frac{2}{3}\mu\right)\frac{\partial v_y}{\partial y}, \tag{B.3}$$

$$\dot{\sigma}_{yy} = \left(K - \frac{2}{3}\mu\right)\frac{\partial v_x}{\partial x} + \left(K + \frac{4}{3}\mu\right)\frac{\partial v_y}{\partial y}, \tag{B.4}$$

$$\dot{\sigma}_{xy} = \mu\left(\frac{\partial v_x}{\partial y} + \frac{\partial v_y}{\partial x}\right). \tag{B.5}$$

Here, the components v stand for the first derivative of the displacement in Equations A.6 and A.7, i.e. the velocity. Equations B.1–B.5 represent five first order partial differential equations for the five unknowns v_x, v_y, σ_{xx}, σ_{yy} and σ_{xy}. The spatial derivatives are approximated with a finite difference quotient. The particular finite difference scheme is equivalent, though not exactly the same, to the rotated staggered grid approach (Saenger *et al.*, 2000; Saenger and Bohlen, 2004; Krüger *et al.*, 2005; Bohlen and Saenger, 2006). Figure B.1 shows an example of a spatial indexing scheme with index i counting the nodal points (dots in Figure B.1) in x–direction and index j counting the nodal points in y–direction. A staggered grid approach is used with so–called center points (empty circles in Figure B.1) at half–positions. Positions where the velocity and stress components

are located are also indicated in Figure B.1. For getting the two equations for velocity (Equations B.1 and B.2) at position (i, j), the following steps have to be performed.

1. Approximate the spatial derivatives in x–direction of the stress components σ_{xx} and σ_{xy} at positions $\left(i, j \pm \frac{1}{2}\right)$ (crosses in Figure B.1) using a finite difference quotient:

$$\left(\frac{\partial \sigma_{xx}}{\partial x}\right)_{\left(i, j \pm \frac{1}{2}\right)} \approx \frac{\sigma_{xx}^{\left(i+\frac{1}{2}, j\pm\frac{1}{2}\right)} - \sigma_{xx}^{\left(i-\frac{1}{2}, j\pm\frac{1}{2}\right)}}{x_{\left(i+\frac{1}{2}, j\pm\frac{1}{2}\right)} - x_{\left(i-\frac{1}{2}, j\pm\frac{1}{2}\right)}} \tag{B.6}$$

$$\left(\frac{\partial \sigma_{xy}}{\partial x}\right)_{\left(i, j \pm \frac{1}{2}\right)} \approx \frac{\sigma_{xy}^{\left(i+\frac{1}{2}, j\pm\frac{1}{2}\right)} - \sigma_{xy}^{\left(i-\frac{1}{2}, j\pm\frac{1}{2}\right)}}{x_{\left(i+\frac{1}{2}, j\pm\frac{1}{2}\right)} - x_{\left(i-\frac{1}{2}, j\pm\frac{1}{2}\right)}} \tag{B.7}$$

2. Interpolate spatial derivatives in x–direction of the stress components σ_{xx} and σ_{xy} from positions $\left(i, j \pm \frac{1}{2}\right)$ (crosses in Figure B.1) to position (i, j) (dot in Figure B.1):

$$\left(\frac{\partial \sigma_{xx}}{\partial x}\right)_{(i,j)} \approx \frac{\left(\begin{array}{c} \left(y_{(i,j)} - y_{\left(i,j-\frac{1}{2}\right)}\right) \left(\frac{\partial \sigma_{xx}}{\partial x}\right)_{\left(i,j+\frac{1}{2}\right)} \\ + \left(y_{\left(i,j+\frac{1}{2}\right)} - y_{(i,j)}\right) \left(\frac{\partial \sigma_{xx}}{\partial x}\right)_{\left(i,j-\frac{1}{2}\right)} \end{array} \right)}{y_{\left(i,j+\frac{1}{2}\right)} - y_{\left(i,j-\frac{1}{2}\right)}} \tag{B.8}$$

$$\left(\frac{\partial \sigma_{xy}}{\partial x}\right)_{(i,j)} \approx \frac{\left(\begin{array}{c} \left(y_{(i,j)} - y_{\left(i,j-\frac{1}{2}\right)}\right) \left(\frac{\partial \sigma_{xy}}{\partial x}\right)_{\left(i,j+\frac{1}{2}\right)} \\ + \left(y_{\left(i,j+\frac{1}{2}\right)} - y_{(i,j)}\right) \left(\frac{\partial \sigma_{xy}}{\partial x}\right)_{\left(i,j-\frac{1}{2}\right)} \end{array} \right)}{y_{\left(i,j+\frac{1}{2}\right)} - y_{\left(i,j-\frac{1}{2}\right)}} \tag{B.9}$$

3. Approximate the spatial derivatives in y–direction of the stress components σ_{yy} and σ_{xy} at positions $\left(i \pm \frac{1}{2}, j\right)$ (crosses in Figure B.1) using a finite difference quotient:

$$\left(\frac{\partial \sigma_{yy}}{\partial y}\right)_{\left(i\pm\frac{1}{2}, j\right)} \approx \frac{\sigma_{yy}^{\left(i\pm\frac{1}{2}, j+\frac{1}{2}\right)} - \sigma_{yy}^{\left(i\pm\frac{1}{2}, j-\frac{1}{2}\right)}}{y_{\left(i\pm\frac{1}{2}, j+\frac{1}{2}\right)} - y_{\left(i\pm\frac{1}{2}, j-\frac{1}{2}\right)}} \tag{B.10}$$

$$\left(\frac{\partial \sigma_{xy}}{\partial y}\right)_{\left(i\pm\frac{1}{2}, j\right)} \approx \frac{\sigma_{xy}^{\left(i\pm\frac{1}{2}, j+\frac{1}{2}\right)} - \sigma_{xy}^{\left(i\pm\frac{1}{2}, j-\frac{1}{2}\right)}}{y_{\left(i\pm\frac{1}{2}, j+\frac{1}{2}\right)} - y_{\left(i\pm\frac{1}{2}, j-\frac{1}{2}\right)}} \tag{B.11}$$

4. Interpolate spatial derivatives in y–direction of the stress components σ_{yy} and σ_{xy} from positions $\left(i \pm \frac{1}{2}, j\right)$ (crosses in Figure B.1) to position (i, j) (dot in Figure B.1):

$$\left(\frac{\partial \sigma_{yy}}{\partial y}\right)_{(i,j)} \approx \frac{\left(\begin{array}{l}\left(x_{(i,j)} - x_{\left(i-\frac{1}{2},j\right)}\right)\left(\frac{\partial \sigma_{yy}}{\partial y}\right)_{\left(i+\frac{1}{2},j\right)} \\ + \left(x_{\left(i+\frac{1}{2},j\right)} - x_{(i,j)}\right)\left(\frac{\partial \sigma_{yy}}{\partial y}\right)_{\left(i-\frac{1}{2},j\right)}\end{array}\right)}{x_{\left(i+\frac{1}{2},j\right)} - x_{\left(i-\frac{1}{2},j\right)}} \tag{B.12}$$

$$\left(\frac{\partial \sigma_{xy}}{\partial y}\right)_{(i,j)} \approx \frac{\left(\begin{array}{l}\left(x_{(i,j)} - x_{\left(i-\frac{1}{2},j\right)}\right)\left(\frac{\partial \sigma_{xy}}{\partial y}\right)_{\left(i+\frac{1}{2},j\right)} \\ + \left(x_{\left(i+\frac{1}{2},j\right)} - x_{(i,j)}\right)\left(\frac{\partial \sigma_{xy}}{\partial y}\right)_{\left(i-\frac{1}{2},j\right)}\end{array}\right)}{x_{\left(i+\frac{1}{2},j\right)} - x_{\left(i-\frac{1}{2},j\right)}} \tag{B.13}$$

5. Multiply the spatial derivatives of the stress components with $\frac{1}{\rho}$ that is defined at position (i, j):

$$\dot{v}_x^{(i,j)} = \frac{1}{\rho_{(i,j)}}\left(\frac{\partial \sigma_{xx}}{\partial x}\right)_{(i,j)} + \frac{1}{\rho_{(i,j)}}\left(\frac{\partial \sigma_{xy}}{\partial y}\right)_{(i,j)} \tag{B.14}$$

$$\dot{v}_y^{(i,j)} = \frac{1}{\rho_{(i,j)}}\left(\frac{\partial \sigma_{xy}}{\partial x}\right)_{(i,j)} + \frac{1}{\rho_{(i,j)}}\left(\frac{\partial \sigma_{yy}}{\partial y}\right)_{(i,j)} \tag{B.15}$$

For getting the three equations for stess (Equations B.3–B.5) at the center position $\left(i - \frac{1}{2}, j - \frac{1}{2}\right)$, a similar procedure has to be performed.

1. Approximate the spatial derivatives in x–direction of the velocity components v_x and v_y at positions $\left(i - \frac{1}{2}, j - \frac{1}{2} \pm \frac{1}{2}\right)$ (crosses in Figure B.1) using a finite difference quotient:

$$\left(\frac{\partial v_x}{\partial x}\right)_{\left(i-\frac{1}{2},j-\frac{1}{2}\pm\frac{1}{2}\right)} \approx \frac{v_x^{\left(i,j-\frac{1}{2}\pm\frac{1}{2}\right)} - v_x^{\left(i-1,j-\frac{1}{2}\pm\frac{1}{2}\right)}}{x_{\left(i,j-\frac{1}{2}\pm\frac{1}{2}\right)} - x_{\left(i-1,j-\frac{1}{2}\pm\frac{1}{2}\right)}} \tag{B.16}$$

$$\left(\frac{\partial v_y}{\partial x}\right)_{\left(i-\frac{1}{2},j-\frac{1}{2}\pm\frac{1}{2}\right)} \approx \frac{v_y^{\left(i,j-\frac{1}{2}\pm\frac{1}{2}\right)} - v_y^{\left(i-1,j-\frac{1}{2}\pm\frac{1}{2}\right)}}{x_{\left(i,j-\frac{1}{2}\pm\frac{1}{2}\right)} - x_{\left(i-1,j-\frac{1}{2}\pm\frac{1}{2}\right)}} \tag{B.17}$$

2. Interpolate spatial derivatives in x–direction of the velocity components v_x and v_y from positions $\left(i - \frac{1}{2}, j - \frac{1}{2} \pm \frac{1}{2}\right)$ (crosses in Figure B.1) to position $\left(i - \frac{1}{2}, j - \frac{1}{2}\right)$ (empty circle in Figure B.1):

$$\left(\frac{\partial v_x}{\partial x}\right)_{\left(i-\frac{1}{2},j-\frac{1}{2}\right)} \approx \frac{\left(\begin{array}{c}\left(y_{\left(i-\frac{1}{2},j-\frac{1}{2}\right)} - y_{\left(i-\frac{1}{2},j-1\right)}\right)\left(\frac{\partial v_x}{\partial x}\right)_{\left(i-\frac{1}{2},j\right)} \\ + \left(y_{\left(i-\frac{1}{2},j\right)} - y_{\left(i-\frac{1}{2},j-\frac{1}{2}\right)}\right)\left(\frac{\partial v_x}{\partial x}\right)_{\left(i-\frac{1}{2},j-1\right)}\end{array}\right)}{y_{\left(i-\frac{1}{2},j\right)} - y_{\left(i-\frac{1}{2},j-1\right)}} \quad \text{(B.18)}$$

$$\left(\frac{\partial v_y}{\partial x}\right)_{\left(i-\frac{1}{2},j-\frac{1}{2}\right)} \approx \frac{\left(\begin{array}{c}\left(y_{\left(i-\frac{1}{2},j-\frac{1}{2}\right)} - y_{\left(i-\frac{1}{2},j-1\right)}\right)\left(\frac{\partial v_y}{\partial x}\right)_{\left(i-\frac{1}{2},j\right)} \\ + \left(y_{\left(i-\frac{1}{2},j\right)} - y_{\left(i-\frac{1}{2},j-\frac{1}{2}\right)}\right)\left(\frac{\partial v_y}{\partial x}\right)_{\left(i-\frac{1}{2},j-1\right)}\end{array}\right)}{y_{\left(i-\frac{1}{2},j\right)} - y_{\left(i-\frac{1}{2},j-1\right)}} \quad \text{(B.19)}$$

3. Approximate the spatial derivatives in y–direction of the velocity components v_x and v_y at positions $\left(i - \frac{1}{2} \pm \frac{1}{2}, j - \frac{1}{2}\right)$ (crosses in Figure B.1) using a finite difference quotient:

$$\left(\frac{\partial v_x}{\partial y}\right)_{\left(i-\frac{1}{2}\pm\frac{1}{2},j-\frac{1}{2}\right)} \approx \frac{v_x^{\left(i-\frac{1}{2}\pm\frac{1}{2},j\right)} - v_x^{\left(i-\frac{1}{2}\pm\frac{1}{2},j-1\right)}}{y_{\left(i-\frac{1}{2}\pm\frac{1}{2},j\right)} - y_{\left(i-\frac{1}{2}\pm\frac{1}{2},j-1\right)}} \quad \text{(B.20)}$$

$$\left(\frac{\partial v_y}{\partial y}\right)_{\left(i-\frac{1}{2}\pm\frac{1}{2},j-\frac{1}{2}\right)} \approx \frac{v_y^{\left(i-\frac{1}{2}\pm\frac{1}{2},j\right)} - v_y^{\left(i-\frac{1}{2}\pm\frac{1}{2},j-1\right)}}{y_{\left(i-\frac{1}{2}\pm\frac{1}{2},j\right)} - y_{\left(i-\frac{1}{2}\pm\frac{1}{2},j-1\right)}} \quad \text{(B.21)}$$

4. Interpolate spatial derivatives in y–direction of the velocity components v_x and v_y from positions $\left(i - \frac{1}{2} \pm \frac{1}{2}, j - \frac{1}{2}\right)$ (crosses in Figure B.1) to position $\left(i - \frac{1}{2}, j - \frac{1}{2}\right)$ (empty circle in Figure B.1):

$$\left(\frac{\partial v_x}{\partial y}\right)_{\left(i-\frac{1}{2},j-\frac{1}{2}\right)} \approx \frac{\left(\begin{array}{c}\left(x_{\left(i-\frac{1}{2},j-\frac{1}{2}\right)} - x_{\left(i-1,j-\frac{1}{2}\right)}\right)\left(\frac{\partial v_x}{\partial y}\right)_{\left(i,j-\frac{1}{2}\right)} \\ + \left(x_{\left(i,j-\frac{1}{2}\right)} - x_{\left(i-\frac{1}{2},j-\frac{1}{2}\right)}\right)\left(\frac{\partial v_x}{\partial y}\right)_{\left(i-1,j-\frac{1}{2}\right)}\end{array}\right)}{x_{\left(i,j-\frac{1}{2}\right)} - x_{\left(i-1,j-\frac{1}{2}\right)}} \tag{B.22}$$

$$\left(\frac{\partial v_y}{\partial y}\right)_{\left(i-\frac{1}{2},j-\frac{1}{2}\right)} \approx \frac{\left(\begin{array}{c}\left(x_{\left(i-\frac{1}{2},j-\frac{1}{2}\right)} - x_{\left(i-1,j-\frac{1}{2}\right)}\right)\left(\frac{\partial v_y}{\partial y}\right)_{\left(i,j-\frac{1}{2}\right)} \\ + \left(x_{\left(i,j-\frac{1}{2}\right)} - x_{\left(i-\frac{1}{2},j-\frac{1}{2}\right)}\right)\left(\frac{\partial v_y}{\partial y}\right)_{\left(i-1,j-\frac{1}{2}\right)}\end{array}\right)}{x_{\left(i,j-\frac{1}{2}\right)} - x_{\left(i-1,j-\frac{1}{2}\right)}} \tag{B.23}$$

5. Multiply the spatial derivatives of the velocity components with the elastic moduli K and μ that are defined at position $\left(i - \frac{1}{2}, j - \frac{1}{2}\right)$:

$$\dot{\sigma}_{xx}^{\left(i-\frac{1}{2},j-\frac{1}{2}\right)} = \left(\begin{array}{c}\left(K_{\left(i-\frac{1}{2},j-\frac{1}{2}\right)} + \frac{4}{3}\mu_{\left(i-\frac{1}{2},j-\frac{1}{2}\right)}\right)\left(\frac{\partial v_x}{\partial x}\right)_{\left(i-\frac{1}{2},j-\frac{1}{2}\right)} \\ + \left(K_{\left(i-\frac{1}{2},j-\frac{1}{2}\right)} - \frac{2}{3}\mu_{\left(i-\frac{1}{2},j-\frac{1}{2}\right)}\right)\left(\frac{\partial v_y}{\partial y}\right)_{\left(i-\frac{1}{2},j-\frac{1}{2}\right)}\end{array}\right) \tag{B.24}$$

$$\dot{\sigma}_{yy}^{\left(i-\frac{1}{2},j-\frac{1}{2}\right)} = \left(\begin{array}{c}\left(K_{\left(i-\frac{1}{2},j-\frac{1}{2}\right)} - \frac{2}{3}\mu_{\left(i-\frac{1}{2},j-\frac{1}{2}\right)}\right)\left(\frac{\partial v_x}{\partial x}\right)_{\left(i-\frac{1}{2},j-\frac{1}{2}\right)} \\ + \left(K_{\left(i-\frac{1}{2},j-\frac{1}{2}\right)} + \frac{4}{3}\mu_{\left(i-\frac{1}{2},j-\frac{1}{2}\right)}\right)\left(\frac{\partial v_y}{\partial y}\right)_{\left(i-\frac{1}{2},j-\frac{1}{2}\right)}\end{array}\right) \tag{B.25}$$

$$\dot{\sigma}_{xy}^{\left(i-\frac{1}{2},j-\frac{1}{2}\right)} = \mu_{\left(i-\frac{1}{2},j-\frac{1}{2}\right)}\left(\left(\frac{\partial v_x}{\partial y}\right)_{\left(i-\frac{1}{2},j-\frac{1}{2}\right)} + \left(\frac{\partial v_y}{\partial x}\right)_{\left(i-\frac{1}{2},j-\frac{1}{2}\right)}\right) \tag{B.26}$$
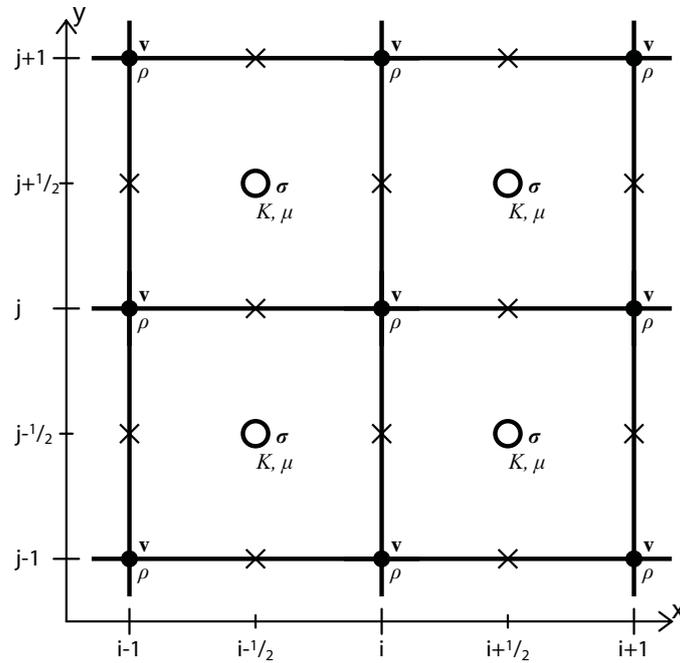
Figure B.1: Four elementary cells for the applied staggered grid FDM. All components of one physical property are defined at the same position in the elementary cell. Spatial derivatives of all unknowns are defined at positions marked with a cross and have to be arithmetically averaged to nodal or center points.

From Equations B.24–B.26 it can be seen that the elastic moduli K and μ only need to be defined at the center position of of one elementary finite difference cell. Elastic moduli do not occur at any other position in the grid. This is different to the widely–used fully staggered grid method (Virieux, 1986), where elastic moduli occur at different positions within one elementary cell. If material boundaries occur in the numerical domain, the numerical grid is built up in such a way that the approximated material boundaries run along boundaries between elementary cells (see Figure 2.3 of Chapter 2). This way, the center positions of elementary cells always lie on either side of a material boundary and never on top of it. However, from Equations B.14 and B.15 it can be seen that the density ρ needs to be defined at nodal points of the numerical grid. Nodal points can lie on top of material boundaries (see Figure 2.3 of Chapter 2). For such nodal points the density has to be arithmetically averaged from the materials of the four surrounding elementary cells.

B.1. Time discretization

The time derivatives in Equations B.14, B.15, B.24, B.25 and B.26 are approximated with an explicit finite difference approach:

$$v_x^{(t_{i+1})} = v_x^{(t_i)} + \Delta t \left(\frac{1}{\rho} \left(\frac{\partial \sigma_{xx}}{\partial x} \right)_{\left(t_{i+\frac{1}{2}}\right)} + \frac{1}{\rho} \left(\frac{\partial \sigma_{xy}}{\partial y} \right)_{\left(t_{i+\frac{1}{2}}\right)} \right), \qquad \text{(B.27)}$$

$$v_y^{(t_{i+1})} = v_y^{(t_i)} + \Delta t \left(\frac{1}{\rho} \left(\frac{\partial \sigma_{xy}}{\partial x} \right)_{\left(t_{i+\frac{1}{2}}\right)} + \frac{1}{\rho} \left(\frac{\partial \sigma_{yy}}{\partial y} \right)_{\left(t_{i+\frac{1}{2}}\right)} \right), \qquad \text{(B.28)}$$

$$\sigma_{xx}^{\left(t_{i+\frac{1}{2}}\right)} = \sigma_{xx}^{\left(t_{i-\frac{1}{2}}\right)} + \Delta t \left(\begin{array}{c} \left(K + \frac{4}{3}\mu\right) \left(\frac{\partial v_x}{\partial x}\right)_{(t_i)} \\ + \left(K - \frac{2}{3}\mu\right) \left(\frac{\partial v_y}{\partial y}\right)_{(t_i)} \end{array} \right), \qquad \text{(B.29)}$$

$$\sigma_{yy}^{\left(t_{i+\frac{1}{2}}\right)} = \sigma_{yy}^{\left(t_{i-\frac{1}{2}}\right)} + \Delta t \left(\begin{array}{c} \left(K - \frac{2}{3}\mu\right) \left(\frac{\partial v_x}{\partial x}\right)_{(t_i)} \\ + \left(K + \frac{4}{3}\mu\right) \left(\frac{\partial v_y}{\partial y}\right)_{(t_i)} \end{array} \right), \qquad \text{(B.30)}$$

$$\sigma_{xy}^{\left(t_{i+\frac{1}{2}}\right)} = \sigma_{xy}^{\left(t_{i-\frac{1}{2}}\right)} + \Delta t \mu \left(\left(\frac{\partial v_x}{\partial y}\right)_{(t_i)} + \left(\frac{\partial v_y}{\partial x}\right)_{(t_i)} \right). \qquad \text{(B.31)}$$

In Equations B.27 – B.31 the spatial indeces i and j are removed compared to Equations B.14, B.15, B.24, B.25 and B.26. The time index t_i denotes any discrete time interval that is calculated in the numerical algorithm. Solutions for the stress components are calculated at half time increments. This procedure is the so–called staggered time integration method (Virieux, 1986). Solutions of the velocity components (Equations B.27 and B.28) are already used for the solutions of the stress components. The time increment has to fulfill the von Neumann stability criterion that is calculated from the wave velocity and the grid spacing of the numerical grid (Higham, 1996; Saenger *et al.*, 2000).

B.2. Boundary conditions

The boundary conditions are explained with the help of Figure B.2 where four elementary cells located at the left boundary of of the finite difference grid are shown. Figure B.2 is comparable with Figure B.1, but the index i counting the nodal points in x–direction is now equal to 1, 2 and 3. Boundary conditions at the other boundaries (bottom, right and top boundary) can easily be reformulated from the ones at the left side of the numerical domain. For a rigid boundary condition all velocity degrees of freedom are simply set to 0 at the nodal points located at the boundary:

$$v_x\left(1, 1...\text{ny}\right) = 0, \tag{B.32}$$

$$v_y\left(1, 1...\text{ny}\right) = 0, \tag{B.33}$$

where ny is the total number of nodal points located at the left boundary. A free slip boundary condition means that the material does not deform perpendicular to the boundary and that no shear stresses occur at the boundary. The first condition is implemented in the numerical algorithm by setting the velocity degrees of freedom perpendicular to the boundary to 0. Vanishing of the shear stresses at the boundary is achieved by setting the velocity degrees of freedom parallel to the boundary at the nodal points located at the boundary equal to the velocity degrees of freedom parallel to the boundary one nodal point away from the boundary:

$$v_x\left(1, 1...\text{ny}\right) = 0, \tag{B.34}$$

$$v_y\left(1, 1...\text{ny}\right) = v_y\left(2, 1...\text{ny}\right). \tag{B.35}$$

For the free surface boundary condition virtual center points outside the numerical domain are introduced (Figure B.2). All stress components on these virtual center points are set to 0. The velocity components on the nodal points located on the boundary are

then calculated in the same way as they are calculated within the numerical domain (Equations B.27 – B.31).
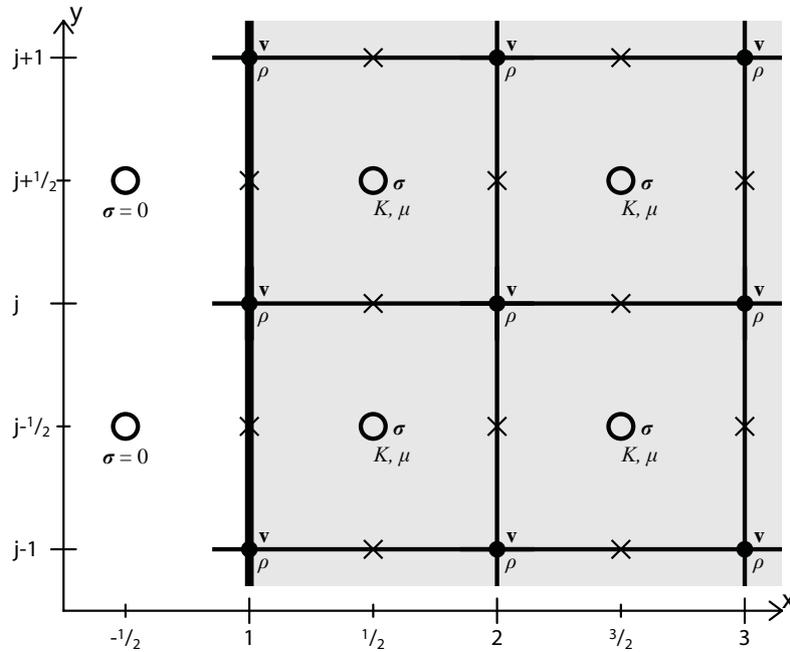
Figure B.2: Four elementary cells for the applied staggered grid FDM located at the left boundary of the numerical domain. Gray shaded area is the numerical domain. Stresses at the virtual center points outside the numerical domain are set to 0 for a free boundary condition.

B.3. Numerical code

The numerical finite difference code for two–dimensional elastic and acoustic wave propagation is written in MATLAB. It is not possible to show the entire code here. However, the core part of the code is within the time loop and is shown below.

```
1    for it = start:nt % TIME LOOP
2        % STRESS DERIVATIVES
3        helpvar             =   (Sxx(2:end,:)        - Sxx(1:end-1,:))          ./ ...
4                                 (x2d_center(2:end,:) - x2d_center(1:end-1,:));
5        dSxx_dx(2:nx-1,2:nz-1) =  interp1(z2d_center(1,:),helpvar',z2d_node(1,2:nz-1))';
6        helpvar             =   (Szz(:,2:end)        - Szz(:,1:end-1))          ./ ...
7                                 (z2d_center(:,2:end) - z2d_center(:,1:end-1));
8        dSzz_dz(2:nx-1,2:nz-1) =  interp1(x2d_center(:,1),helpvar ,x2d_node(2:nx-1,1)) ;
9        helpvar             =   (Sxz(2:end,:)        - Sxz(1:end-1,:))          ./ ...
10                               (x2d_center(2:end,:) - x2d_center(1:end-1,:));
11       dSxz_dx(2:nx-1,2:nz-1) =  interp1(z2d_center(1,:),helpvar',z2d_node(1,2:nz-1))';
12       helpvar             =   (Sxz(:,2:end)        - Sxz(:,1:end-1))          ./ ...
13                               (z2d_center(:,2:end) - z2d_center(:,1:end-1));
14       dSxz_dz(2:nx-1,2:nz-1) =  interp1(x2d_center(:,1),helpvar ,x2d_node(2:nx-1,1)) ;
15
16       % CALCULATE VELOCITIES
17       vx(2:nx-1,2:nz-1)      =   vx(2:nx-1,2:nz-1) + dt .* ...
18                                 (dSxx_dx(2:nx-1,2:nz-1) + dSxz_dz(2:nx-1,2:nz-1)) ./ ...
19                                 (     node_type(2:nx-1,2:nz-1,1).*rho(1) ...
20                                   +   node_type(2:nx-1,2:nz-1,2).*rho(2) );
21       vz(2:nx-1,2:nz-1)      =   vz(2:nx-1,2:nz-1) + dt .* ...
22                                 (dSxz_dx(2:nx-1,2:nz-1) + dSzz_dz(2:nx-1,2:nz-1)) ./ ...
23                                 (     node_type(2:nx-1,2:nz-1,1).*rho(1) ...
24                                   +   node_type(2:nx-1,2:nz-1,2).*rho(2) );
25
26       % APPLY BOUNDARY CONDITIONS (NOT SHOWN HERE)
27
28       % VELOCITY DERIVATIVES
29       helpvar     =   (vx(2:end,:)        - vx(1:end-1,:))        ./ ...
30                       (x2d_node(2:end,:) - x2d_node(1:end-1,:));
31       dvx_dx      =   interp1(z2d_node(1,:),helpvar',z2d_center(1,:))';
32       helpvar     =   (vz(:,2:end)        - vz(:,1:end-1))        ./ ...
33                       (z2d_node(:,2:end) - z2d_node(:,1:end-1));
34       dvz_dz      =   interp1(x2d_node(:,1),helpvar ,x2d_center(:,1)) ;
35       helpvar     =   (vz(2:end,:)        - vz(1:end-1,:))        ./ ...
36                       (x2d_node(2:end,:) - x2d_node(1:end-1,:));
37       dvz_dx      =   interp1(z2d_node(1,:),helpvar',z2d_center(1,:))';
38       helpvar     =   (vx(:,2:end)        - vx(:,1:end-1))        ./ ...
39                       (z2d_node(:,2:end) - z2d_node(:,1:end-1));
40       dvx_dz      =   interp1(x2d_node(:,1),helpvar ,x2d_center(:,1)) ;
41
42       % CALCULATE STRESSES
43       Sxx         =   Sxx +   dt*(   (2*mu(center_type)+lambda(center_type)) .*dvx_dx ...
44                                    + lambda(center_type)                      .*dvz_dz );
45       Szz         =   Szz +   dt*(   lambda(center_type)                      .*dvx_dx ...
46                                    + (2*mu(center_type)+lambda(center_type)) .*dvz_dz );
47       Sxz         =   Sxz +   dt*(   mu(center_type)                 .*(dvx_dz + dvz_dx));
48   end
```

In the numerical code above, most of the variables and unknowns are self–explaining. In all variables and unknowns the first spatial index is in x–direction, the second in y–direction, e.g. in line `3 Sxx(2:end,:)` means second entry to last entry in x–direction and all entries in y–direction of the stress component σ_{xx}. The variables `x2d_center` and `z2d_center` contain the coordinate values of the center positions of all elementary cells of the numerical grid (here, x– and z–coordinates, not x– and y–coordinates). The variables `x2d_node` and `z2d_node` contain the coordinate values of all nodal points. The value `dt` is the time increment (Δt in Equations B.27 – B.31). The matrix `node_type` contains two entries for each nodal point. The first entry is the number of elementary cells around each nodal point belonging to material type 1 divided by four (possible values: 0, $\frac{1}{4}$, $\frac{1}{2}$, $\frac{3}{4}$ and 1). The second entry is the number of elementary cells around each nodal point belonging to material type 2 divided by four (i.e. 1 minus first entry). This formulation allows an easy implementation of the arithmetic averaging of density values. The matrix `center_type` contains one value for each center position. It is either 1 or 2, depending which material type the elementary cell belongs to. The material property vectors `rho`, `mu` and `lambda` each contains two values, the first for material type 1 and the second for material type 2.

The different lines of the numerical code correspond to the equations described above in the following relation:

- Lines 3, 4, 9 and 10 correspond to Equations B.6 and B.7.
- Lines 5 and 11 correspond to Equations B.8 and B.9.
- Lines 6, 7, 12 and 13 correspond to Equations B.10 and B.11.
- Lines 8 and 14 correspond to Equations B.12 and B.13.
- Lines 17 – 24 correspond to Equations B.27 and B.28.
- Lines 29, 30, 35 and 36 correspond to Equations B.16 and B.17.
- Lines 31 and 37 correspond to Equations B.18 and B.19.
- Lines 32, 33, 38 and 39 correspond to Equations B.20 and B.21.
- Lines 34 and 40 correspond to Equations B.22 and B.23.
- Lines 43 – 47 correspond to Equations B.29 – B.31.

Implementation of the different types of boundary conditions at the left boundary of the numerical domain is shown below. Boundary conditions at the other boundaries (bottom,

right and top boundary) can easily be reformulated from the ones at the left side of the numerical domain.

```matlab
1   switch bc_left
2       case 'rigid_boundary'
3           vx(1,2:nz-1)        =   zeros(1,nz-2);
4           vz(1,2:nz-1)        =   zeros(1,nz-2);
5       case 'free_slip'
6           vx(1,2:nz-1)        =   zeros(1,nz-2);
7           vz(1,2:nz-1)        =   vz(2,2:nz-1);
8       case 'free_surface' % virtual stress-values outside domain = 0
9           helpvar             =   Sxx(1,:) ./ (2*(x2d_center(1,1)-x2d_node(1,1)));
10          dSxx_dx(1,2:nz-1)   =   interp1(z2d_center(1,:),helpvar,z2d_node(1,2:nz-1));
11
12          dSzz_dz(1,2:nz-1)   =   .5*(Szz(1,2:end)-Szz(1,1:end-1)) ./ ...
13                                  (z2d_center(1,2:end)-z2d_center(1,1:end-1));
14
15          helpvar             =   Sxz(1,:) ./ (2*(x2d_center(1,1)-x2d_node(1,1)));
16          dSxz_dx(1,2:nz-1)   =   interp1(z2d_center(1,:),helpvar,z2d_node(1,2:nz-1));
17
18          dSxz_dz(1,2:nz-1)   =   .5*(Sxz(1,2:end)-Sxz(1,1:end-1)) ./ ...
19                                  (z2d_center(1,2:end)-z2d_center(1,1:end-1));
20
21          vx(1,2:nz-1)        =   vx(1,2:nz-1) + dt .* ...
22                                  (dSxx_dx(1,2:nz-1) + dSxz_dz(1,2:nz-1)) ./ ...
23                                  (     node_type(1,2:nz-1,1).*rho(1)
24                                      + node_type(1,2:nz-1,2).*rho(2) );
25          vz(1,2:nz-1)        =   vz(1,2:nz-1) + dt .* ...
26                                  (dSxz_dx(1,2:nz-1) + dSzz_dz(1,2:nz-1)) ./ ...
27                                  (     node_type(1,2:nz-1,1).*rho(1)
28                                      + node_type(1,2:nz-1,2).*rho(2) );
29   end
```

In the code above Lines 3 and 4 correspond to Equations B.32 and B.33. Lines 6 and 7 correspond to Equations B.34 and B.35. For the free surface boundary condition Lines 9 – 28 are very similar to Lines 3 – 24 of the previously shown code for the nodal points within the numerical domain, only that on the virtual center points outside the numerical domain stress values equal to 0 are assumed.

References

Bohlen T. and Saenger E. H., 2006: **Accuracy of heterogeneous staggered-grid finite-difference modeling of Rayleigh waves**, Geophysics 71, T109–T115, doi: 10.1190/1.2213051

Higham N. J., 1996: **Accuracy and stability of numerical algorithms**, Society for Industrial and Applied Mathematics, Philadelphia, ISBN 0-8987-1355-2

Krüger O. S., Saenger E. H. and Shapiro S. A., 2005: **Scattering and diffraction by a single crack: An accuracy analysis of the rotated staggered grid**, Geophysical Journal International 162, 25–31, doi:10.1111/j.1365-246X.2005.02647.x

Saenger E. H. and Bohlen T., 2004: **Finite-difference modeling of viscoelastic and anisotropic wave propagation using the rotated staggered grid**, Geophysics 69, 583–591, doi:10.1190/1.1707078

Saenger E. H., Gold N. and Shapiro S. A., 2000: **Modeling the propagation of elastic waves using a modified finite-difference grid**, Wave Motion 31, 77–92

Virieux J., 1986: **P-Sv-wave propagation in heterogeneous media: Velocity-stress finite-difference method**, Geophysics 51, 889–901

Appendix C
Finite element method

The finite element method used for spatial discretization of the governing equations in Chapters 2 and 3 is here explained in more details. The finite element method is explained in many textbooks, e.g. Hughes (1987); Bathe (1996); Zienkiewicz and Taylor (2000); Cohen (2002). In the following not many more references will be given. Purely elastic media, inviscid fluids (acoustic) and viscous fluids (visco–acoustic) are modeled with the finite element method. Therefore, the general Equation A.18 is condidered in the following. It is written out once more:

$$\rho \ddot{\tilde{\mathbf{u}}} = \tilde{\mathbf{B}}^T \mathbf{D}_{el} \tilde{\mathbf{B}} \tilde{\mathbf{u}} + \tilde{\mathbf{B}}^T \mathbf{D}_{visc} \tilde{\mathbf{B}} \dot{\tilde{\mathbf{u}}}, \tag{C.1}$$

where

$$\tilde{\mathbf{u}} = \begin{Bmatrix} u_x \\ u_y \end{Bmatrix}, \tag{C.2}$$

$$\tilde{\mathbf{B}} = \begin{bmatrix} \frac{\partial}{\partial x} & 0 \\ 0 & \frac{\partial}{\partial y} \\ \frac{\partial}{\partial y} & \frac{\partial}{\partial x} \end{bmatrix}, \tag{C.3}$$

and $\mathbf{D}_{el}$ is the elastic constitutive matrix and $\mathbf{D}_{visc}$ is the viscous constitutive matrix. The symbol ˜ on top of certain terms denotes the continuous nature of these terms. Equation C.1 represents two linear second order partial differential equations for the two continuous unknown functions u_x and u_y. The discretization of Equation C.1 with the finite element approach happens at the level of one single so–called finite element. Equation C.1 is therefore reformulated for one single element:

$$\check{\rho}\ddot{\tilde{\mathbf{u}}} = \tilde{\mathbf{B}}^T\check{\mathbf{D}}_{el}\tilde{\mathbf{B}}\tilde{\mathbf{u}} + \tilde{\mathbf{B}}^T\check{\mathbf{D}}_{visc}\tilde{\mathbf{B}}\dot{\tilde{\mathbf{u}}}. \tag{C.4}$$

The symbol ˘ on top of certain terms denotes the fact that these terms are defined only for one specific element and can be different for different elements. Later, the formulation for one single finite element will be included into a global formulation. The functions $\tilde{u}_x$ and $\tilde{u}_y$ are assumed to be continuous within the finite element under consideration. A finite element is a small control area (in two dimensions, a control volume in three dimensions) with a certain number of vertices. The first step in the discretization algorithm of Equation C.4 consists of multiplying the equation with the test functions $\check{\mathbf{N}}$. At the same time integration over the area of the whole finite element (denoted Ω) is carried out to get the weighted residual formulation:

$$\int_{\Omega} \check{\mathbf{N}}^T\check{\rho}\ddot{\tilde{\mathbf{u}}}d\Omega = \int_{\Omega} \check{\mathbf{N}}^T\tilde{\mathbf{B}}^T\check{\mathbf{D}}_{el}\tilde{\mathbf{B}}\tilde{\mathbf{u}}d\Omega + \int_{\Omega} \check{\mathbf{N}}^T\tilde{\mathbf{B}}^T\check{\mathbf{D}}_{visc}\tilde{\mathbf{B}}\dot{\tilde{\mathbf{u}}}d\Omega. \tag{C.5}$$

The test functions are a set of functions that will be defined later. The fundamental properties of the test functions is that one function has a value 1 at one vertex of the element while all other functions have the value 0 at this vertex, and the sum of all test functions is always 1 within the whole element. The general form of the matrix $\check{\mathbf{N}}$ is

$$\check{\mathbf{N}} = \begin{bmatrix} \check{N}_1 & 0 & \check{N}_2 & 0 & \cdots & \check{N}_n & 0 \\ 0 & \check{N}_1 & 0 & \check{N}_2 & \cdots & 0 & \check{N}_n \end{bmatrix}, \tag{C.6}$$

where n is the number of nodes in one finite element that is used. In Equation C.5 second order spatial derivatives of the unknowns $\tilde{\mathbf{u}}$ and $\dot{\tilde{\mathbf{u}}}$ occur ($\tilde{\mathbf{B}}^T\tilde{\mathbf{B}}$). Integration by parts moves one spatial derivative from the unknowns to the test functions. It also introduces a minus sign to all terms that are integrated by parts:

$$\int_{\Omega} \check{\mathbf{N}}^T\check{\rho}\ddot{\tilde{\mathbf{u}}}d\Omega = -\int_{\Omega} \left(\tilde{\mathbf{B}}\check{\mathbf{N}}\right)^T\check{\mathbf{D}}_{el}\tilde{\mathbf{B}}\tilde{\mathbf{u}}d\Omega - \int_{\Omega} \left(\tilde{\mathbf{B}}\check{\mathbf{N}}\right)^T\check{\mathbf{D}}_{visc}\tilde{\mathbf{B}}\dot{\tilde{\mathbf{u}}}d\Omega. \tag{C.7}$$

Integration by parts gives rise to boundary terms. In the finite element discretization these terms are simply ignored. This is allowed since the boundary terms of one finite element are the same but with opposite sign as the boundary terms of the neighboring finite elements. When the formulations of the individual elements are put together into the global formulation, these terms would anyway cancel each other out. Care has only to be taken at the boundary of the numerical domain where the elements have no neighbors. There, ingnoring the boundary terms of the integration by parts simply leads to a free surface boundary condition, which is also called natural boundary condition. This is a big advantage of the finite element formulation since it is straightforward to implement a free surface. A free surface basically means not defining anything at this boundary.

The contiuous function $\tilde{\mathbf{u}}$ is now approximated with the so–called shape functions:

$$
\tilde{\mathbf{u}} = \begin{Bmatrix} u_x \\ u_y \end{Bmatrix} \approx \begin{bmatrix} \check{N}_1 & 0 & \check{N}_2 & 0 & \cdots & \check{N}_n & 0 \\ 0 & \check{N}_1 & 0 & \check{N}_2 & \cdots & 0 & \check{N}_n \end{bmatrix} \begin{Bmatrix} \check{u}_{x1} \\ \check{u}_{y1} \\ \check{u}_{x2} \\ \check{u}_{y2} \\ \vdots \\ \check{u}_{xn} \\ \check{u}_{yn} \end{Bmatrix} = \check{\mathbf{N}}\check{\mathbf{u}}. \tag{C.8}
$$

Here, the so–called Galerkin method is applied, which means that the shape functions to approximate the unknown function is the same as the test functions used in Equation C.5. Components $\check{u}_{xi}$ and $\check{u}_{yi}$ are the displacements in x– and y–direction, respectively, at the i–th vertex of the finite element under consideration. This approximation (Equation C.8) reduces the continuous function $\tilde{\mathbf{u}}$ to discrete values $\check{\mathbf{u}}$ at the vertices of the finite element grid. Equation C.8 is now substituted into Equation C.7:

$$
\int_\Omega \check{\mathbf{N}}^T \check{\rho} \check{\mathbf{N}} \ddot{\check{\mathbf{u}}} d\Omega = -\int_\Omega \left(\tilde{\mathbf{B}}\check{\mathbf{N}}\right)^T \check{\mathbf{D}}_{el} \tilde{\mathbf{B}}\check{\mathbf{N}}\check{\mathbf{u}} d\Omega - \int_\Omega \left(\tilde{\mathbf{B}}\check{\mathbf{N}}\right)^T \check{\mathbf{D}}_{visc} \tilde{\mathbf{B}}\check{\mathbf{N}}\dot{\check{\mathbf{u}}} d\Omega. \tag{C.9}
$$

The vector $\check{\mathbf{u}}$ only contains values of the displacement field defined at the vertices of the finite element and is indipendent of the x– and y–position. Therefore, the vector $\check{\mathbf{u}}$ can

be excluded from the integrals. At the same time a new $\check{\mathbf{B}}$–matrix is defined and the equation is slightly rearranged:

$$\int_\Omega \check{\mathbf{N}}^T \check{\rho} \check{\mathbf{N}} d\Omega \ddot{\check{\mathbf{u}}} + \int_\Omega \check{\mathbf{B}}^T \check{\mathbf{D}}_{visc} \check{\mathbf{B}} d\Omega \dot{\check{\mathbf{u}}} + \int_\Omega \check{\mathbf{B}}^T \check{\mathbf{D}}_{el} \check{\mathbf{B}} d\Omega \check{\mathbf{u}} = 0, \tag{C.10}$$

where

$$\check{\mathbf{B}} = \begin{bmatrix} \frac{\partial \check{N}_1}{\partial x} & 0 & \frac{\partial \check{N}_2}{\partial x} & 0 & \cdots & \frac{\partial \check{N}_n}{\partial x} & 0 \\ 0 & \frac{\partial \check{N}_1}{\partial y} & 0 & \frac{\partial \check{N}_2}{\partial y} & \cdots & 0 & \frac{\partial \check{N}_n}{\partial y} \\ \frac{\partial \check{N}_1}{\partial y} & \frac{\partial \check{N}_1}{\partial x} & \frac{\partial \check{N}_2}{\partial y} & \frac{\partial \check{N}_2}{\partial x} & \cdots & \frac{\partial \check{N}_n}{\partial y} & \frac{\partial \check{N}_n}{\partial x} \end{bmatrix}. \tag{C.11}$$

Equation C.10 can be written in a more compact form:

$$\check{\mathbf{M}} \ddot{\check{\mathbf{u}}} + \check{\mathbf{C}} \dot{\check{\mathbf{u}}} + \check{\mathbf{K}} \check{\mathbf{u}} = 0, \tag{C.12}$$

where

$$\check{\mathbf{M}} = \int_\Omega \check{\mathbf{N}}^T \check{\rho} \check{\mathbf{N}} d\Omega, \tag{C.13}$$

$$\check{\mathbf{C}} = \int_\Omega \check{\mathbf{B}}^T \check{\mathbf{D}}_{visc} \check{\mathbf{B}} d\Omega, \tag{C.14}$$

$$\check{\mathbf{K}} = \int_\Omega \check{\mathbf{B}}^T \check{\mathbf{D}}_{el} \check{\mathbf{B}} d\Omega. \tag{C.15}$$

Matrix $\check{\mathbf{M}}$ is called the local mass matrix, matrix $\check{\mathbf{C}}$ is called the local damping matrix and matrix $\check{\mathbf{K}}$ is called the local stiffness matrix. Equation C.12 is valid for one single finite element of a larger finite element mesh. The assembly of a global system of equations is in principle straightforward, but requires a good indexing scheme that links the equation numbering of each individual element to the global indices. In general, at each nodal point that is a vertex of more than one finite element, Equations C.12 of the different

elements surrounding this nodal point are simply added. This leads to a global system of equations:

$$\mathbf{M\ddot{u}} + \mathbf{C\dot{u}} + \mathbf{Ku} = 0, \tag{C.16}$$

where matrix $\mathbf{M}$ is called the global mass matrix, matrix $\mathbf{C}$ is called the global damping matrix and $\mathbf{K}$ is called the global stiffness matrix. Vector $\mathbf{u}$ contains all the unknown displacements of the whole numerical domain.

C.1. Lumped mass matrix

The local mass matrix $\mathbf{\breve{M}}$ (Equation C.13) written out is:

$$\mathbf{\breve{M}} = \breve{\rho} \int_\Omega \begin{bmatrix} \breve{N}_1\breve{N}_1 & 0 & \breve{N}_1\breve{N}_2 & 0 & \cdots & \breve{N}_1\breve{N}_n & 0 \\ 0 & \breve{N}_1\breve{N}_1 & 0 & \breve{N}_1\breve{N}_2 & \cdots & 0 & \breve{N}_1\breve{N}_n \\ \breve{N}_2\breve{N}_1 & 0 & \breve{N}_2\breve{N}_2 & 0 & \cdots & \breve{N}_2\breve{N}_n & 0 \\ 0 & \breve{N}_2\breve{N}_1 & 0 & \breve{N}_2\breve{N}_2 & \cdots & 0 & \breve{N}_2\breve{N}_n \\ \vdots & \vdots & \vdots & \vdots & \ddots & \vdots & \vdots \\ \breve{N}_n\breve{N}_1 & 0 & \breve{N}_n\breve{N}_2 & 0 & \cdots & \breve{N}_n\breve{N}_n & 0 \\ 0 & \breve{N}_n\breve{N}_1 & 0 & \breve{N}_n\breve{N}_2 & \cdots & 0 & \breve{N}_n\breve{N}_n \end{bmatrix} d\Omega. \tag{C.17}$$

The matrix in Equation C.17 and therefore also the corresponding global mass matrix $\mathbf{M}$ is not diagonal. For the solution of Equation C.16 the global mass matrix has to be inverted. The inversion of a non–diagonal matrix is computationally expensive and leads to a full matrix. For computational convenience the local mass matrix (Equation C.17) is approximated with a diagonal matrix, the so–called local lumped mass matrix (Zienkiewicz and Taylor, 2000; Cohen, 2002). In this process conservation of the mass of one finite element, i.e.

$$\sum_i \sum_j \breve{M}_{ij} = \sum_i \breve{M}_{L,ii} = \int_\Omega \breve{\rho} d\Omega, \tag{C.18}$$

has to be preserved. In Equation C.18 $\check{M}_{ij}$ are the elements of the normal local mass matrix $\check{\mathbf{M}}$ and $\check{M}_{L,ii}$ are the diagonal elements of the local lumped mass matrix $\check{\mathbf{M}}_L$. Mass lumping is done with the row sum method:

$$\check{M}_{L,ii} = \sum_j \check{M}_{ij} = \check{\rho} \int_\Omega \check{N}_i \sum_j \check{N}_j d\Omega = \check{\rho} \int_\Omega \check{N}_i d\Omega. \qquad \text{(C.19)}$$

The sum of all shape functions $(\sum_j \check{N}_j)$ is always 1. This is one of the fundamental definitions of the set of shape functions. Therefore, the summation in Equation C.18 is eliminated and the local lumped mass matrix becomes:

$$\check{\mathbf{M}}_L = \check{\rho} \int_\Omega \begin{bmatrix} \check{N}_1 & 0 & 0 & 0 & \cdots & 0 & 0 \\ 0 & \check{N}_1 & 0 & 0 & \cdots & 0 & 0 \\ 0 & 0 & \check{N}_2 & 0 & \cdots & 0 & 0 \\ 0 & 0 & 0 & \check{N}_2 & \cdots & 0 & 0 \\ \vdots & \vdots & \vdots & \vdots & \ddots & \vdots & \vdots \\ 0 & 0 & 0 & 0 & \cdots & \check{N}_n & 0 \\ 0 & 0 & 0 & 0 & \cdots & 0 & \check{N}_n \end{bmatrix} d\Omega. \qquad \text{(C.20)}$$

The local lumped mass matrix is now used for building up the global system of equations (Equation C.16) that now becomes:

$$\mathbf{M}_L \ddot{\mathbf{u}} + \mathbf{C}\dot{\mathbf{u}} + \mathbf{K}\mathbf{u} = 0. \qquad \text{(C.21)}$$

C.2. Numerical integration

The different terms that build the equation for each finite element (Equations C.14, C.15 and C.20) contain spatial integrals over the area of the finite element Ω. The finite element mesh is not necessarily regular, i.e. each individual finite element has a different shape and a different size. Therefore, the spatial integrals will be different for each finite element and it would be computationally too expensive (though not impossible)

to evaluate each integral analytically. The integrals are evaluated numerically using the so–called Gauss–Legendre quadrature. A standardized coordinate system (ξ, ζ), also called local coordinate system, is used. All the functions will be mapped to this local coordinate sytem. A general function f, which is defined on the local coordinate system, is numerically integrated over the area Ξ as follows:

$$\int_\Xi f\left(\xi, \zeta\right) d\Xi \approx \sum_{i=1}^{\text{nip}} f\left(\xi_i, \zeta_i\right) w_i, \tag{C.22}$$

where the positions (ξ_i, ζ_i) inside the area Ξ are the Gauss–Legendre quadrature points. Only at these points the function f needs to be evaluated for calculating the total integral. At each quadrature point a weighting factor w_i is defined that has to be multiplied with the function value at this point. For illustration one can imagine that the volume under the two–dimensional continuous function f is split into nip columns. The height of each column is the value of the function at the center of the column and w_i is the area of the base of the column. The exact values of (ξ_i, ζ_i) and w_i will be defined later.

C.3. Isoparametric elements

Numerical integration (Equation C.22) is performed on the reference element Ξ (called local element) that is defined in the local coordinate system (ξ, ζ). It is defined once and stays the same for all finite elements of the numerical grid. However, the finite element grid and all integrations in Equations C.14, C.15 and C.20 are defined in the physical coordinate system (x, y) (also called global coordinate system). Therefore, a coordinate transformations has to be performed to change the integration boundaries from global to local coordinates.

Also, the spatial derivatives of the shape functions $\check{\mathbf{N}}$ in Equations C.14 and C.15 are taken with respect to global coordinates (x, y). This implies that these derivatives change from one element to the next depending on the actual shape and size of the element. It is much more convenient to define the shape functions and their spatial derivatives on the reference element Ξ. This way, they stay constant for all the elements and are now

called **N**. However, it requires a second coordinate transformation to change the spatial derivatives of the shape function with respect to local coordinates (ξ, ζ) to derivatives with respect to global coordinates (x, y).

C.3.1. Transform derivatives of shape functions from local to global coordinates

The specific shape functions **N** used in this thesis will be defined later. Generally, shape functions are a set of easily differentiable functions (e.g. linear, quadratic, cubic) that are defined on the local coordinate system (ξ, ζ). Their derivatives can be transformed from local to global coordinates using the Jacobian matrix $\check{\mathbf{J}}$, which is defined for each element in the numerical grid:

$$\left\{ \begin{matrix} \frac{\partial}{\partial \xi} \\ \frac{\partial}{\partial \zeta} \end{matrix} \right\} = \begin{bmatrix} \frac{\partial x}{\partial \xi} & \frac{\partial y}{\partial \xi} \\ \frac{\partial x}{\partial \zeta} & \frac{\partial y}{\partial \zeta} \end{bmatrix} \left\{ \begin{matrix} \frac{\partial}{\partial x} \\ \frac{\partial}{\partial y} \end{matrix} \right\} = \check{\mathbf{J}} \left\{ \begin{matrix} \frac{\partial}{\partial x} \\ \frac{\partial}{\partial y} \end{matrix} \right\}. \tag{C.23}$$

The Jacobian matrix $\check{\mathbf{J}}$ is the differentiation of the global coordinates with respect to the local coordinates and is only valid for one single finite element (note the symbol $\smile$ on top of $\check{\mathbf{J}}$). As done in Equation C.8 for the unknown vector $\tilde{\mathbf{u}}$, coordinates within one finite element can be approximated using the shape functions and the coordinates of the vertices of the element:

$$\begin{bmatrix} x & y \end{bmatrix} \approx \begin{bmatrix} \check{N}_1 & \check{N}_2 & \cdots & \check{N}_n \end{bmatrix} \begin{bmatrix} \check{x}_1 & \check{y}_1 \\ \check{x}_2 & \check{y}_2 \\ \vdots & \vdots \\ \check{x}_n & \check{y}_n \end{bmatrix}. \tag{C.24}$$

The values $\check{x}_i$ and $\check{y}_i$ are the global coordinates of the vertices of the finite element under study. The Jacobian matrix $\check{\mathbf{J}}$ is then defined for one finite element as

$$\check{\mathbf{J}} \approx \begin{bmatrix} \frac{\partial N_1}{\partial \xi} & \frac{\partial N_2}{\partial \xi} & \cdots & \frac{\partial N_n}{\partial \xi} \\ \frac{\partial N_1}{\partial \zeta} & \frac{\partial N_2}{\partial \zeta} & \cdots & \frac{\partial N_n}{\partial \zeta} \end{bmatrix} \begin{bmatrix} \check{x}_1 & \check{y}_1 \\ \check{x}_2 & \check{y}_2 \\ \vdots & \vdots \\ \check{x}_n & \check{y}_n \end{bmatrix}. \tag{C.25}$$

Note that in this formulation the locally defined spatial derivatives of the shape functions occur and the symbol ˘ on top of the shape functions N_i disappears compared to Equation C.24. As mentioned above, the shape functions and their derivatives are defined on the local coordinates (ξ, ζ). Therefore, Equation C.25 allows a direct calculation of the Jacobian matrix for each finite element. The desired coordinate transformation of the derivatives of the shape functions with respect to local coordinates to derivatives with respect to global coordinates is then

$$\left\{ \begin{matrix} \frac{\partial}{\partial x} \\ \frac{\partial}{\partial y} \end{matrix} \right\} = \check{\mathbf{J}}^{-1} \left\{ \begin{matrix} \frac{\partial}{\partial \xi} \\ \frac{\partial}{\partial \zeta} \end{matrix} \right\}. \tag{C.26}$$

The superscript -1 denotes the inverse of a matrix. Equation C.26 can now be used to calculate the spatial derivatives of the shape functions in Equations C.14 and C.15.

C.3.2. Transform integration boundaries from global to local coordinates

The numerical integration (Equation C.22) is performed on the local element Ξ. However, the integrals in Equations C.14, C.15 and C.20 are defined in terms of global coordinates. The necessary coordinate transformation is (here shown with an arbitrary function f):

$$\int_\Omega f(x, y) \, d\Omega = \int_\Xi f(\xi, \zeta) \det\left(\check{\mathbf{J}}\right) d\Xi. \tag{C.27}$$

The expression $\det\left(\check{\mathbf{J}}\right)$ denotes the determinant of the Jacobian matrix $\check{\mathbf{J}}$.

C.3.3. Application of numerical integration and coordinate transforms

Applying the numerical integration and the coordinate transformations described above to Equations C.14, C.15 and C.20 leads to the numerically calculated coefficients in Equation C.21. The shape functions $\mathbf{N}$ and their derivatives are defined on the local element Ξ (see below for the exact definition). The spatial derivatives are:

$$\nabla_{(\xi,\zeta)}\mathbf{N} = \begin{bmatrix} \frac{\partial N_1}{\partial \xi} & \frac{\partial N_2}{\partial \xi} & \cdots & \frac{\partial N_n}{\partial \xi} \\ \frac{\partial N_1}{\partial \zeta} & \frac{\partial N_2}{\partial \zeta} & \cdots & \frac{\partial N_n}{\partial \zeta} \end{bmatrix}. \tag{C.28}$$

Applying Equation C.26 to Equation C.28 leads to the spatial derivatives of the shape functions with respect to global coordinates:

$$\nabla_{(x,y)}\check{\mathbf{N}} = \check{\mathbf{J}}^{-1}\nabla_{(\xi,\zeta)}\mathbf{N} = \begin{bmatrix} \frac{\partial \check{N}_1}{\partial x} & \frac{\partial \check{N}_2}{\partial x} & \cdots & \frac{\partial \check{N}_n}{\partial x} \\ \frac{\partial \check{N}_1}{\partial y} & \frac{\partial \check{N}_2}{\partial y} & \cdots & \frac{\partial \check{N}_n}{\partial y} \end{bmatrix}. \tag{C.29}$$

This expression is now used to construct $\check{\mathbf{C}}$, $\check{\mathbf{K}}$ and $\check{\mathbf{M}}_L$ as in Equations C.14, C.15 and C.20. The general form of all three coefficients $\check{\mathbf{C}}$, $\check{\mathbf{K}}$ and $\check{\mathbf{M}}_L$ is, already including Equation C.29,

$$\int_{\Omega} f\left(\nabla_{(x,y)}\check{\mathbf{N}}\right) d\Omega = \int_{\Omega} \check{\mathbf{J}}^{-1} f\left(\nabla_{(\xi,\zeta)}\mathbf{N}\right) d\Omega, \tag{C.30}$$

where f is the function that creates $\check{\mathbf{C}}$, $\check{\mathbf{K}}$ or $\check{\mathbf{M}}_L$. Using Equation C.27 transforms the integration boundaries in Equation C.30 from global to local coordinates:

$$\int_{\Omega} \check{\mathbf{J}}^{-1} f\left(\nabla_{(\xi,\zeta)}\mathbf{N}\right) d\Omega = \int_{\Xi} \check{\mathbf{J}}^{-1} f\left(\nabla_{(\xi,\zeta)}\mathbf{N}\right) \det\left(\check{\mathbf{J}}\right) d\Xi. \tag{C.31}$$

Note that the shape functions themselves do not change during this coordinate transformation from global to local coordinates. Applying the Gauss–Legendre quadrature (Equation C.22) leads to the final summation formulation:

$$\int_{\Xi} \check{\mathbf{J}}^{-1} f \left(\nabla_{(\xi,\zeta)} \mathbf{N} \right) \det \left(\check{\mathbf{J}} \right) d\Xi = \sum_{i=1}^{\mathrm{nip}} \check{\mathbf{J}}^{-1} f \left(\nabla_{(\xi_i,\zeta_i)} \mathbf{N} \right) \det \left(\check{\mathbf{J}} \right) w_i. \tag{C.32}$$

This summation is carried out in the numerical finite element algorithm as a loop over the integration points of one element.

C.4. The seven node triangular element

The finite element used in this thesis is a seven node triangular element shown in Figure C.1. The local coordinates of the seven nodes of the element (green dots in Figure C.1) are:

Node number 1: $(\xi_{N1}, \zeta_{N1}) = (0,0)$ Node number 4: $(\xi_{N4}, \zeta_{N4}) = \left(\frac{1}{2}, 0 \right)$
Node number 2: $(\xi_{N2}, \zeta_{N2}) = (1,0)$ Node number 5: $(\xi_{N5}, \zeta_{N5}) = \left(\frac{1}{2}, \frac{1}{2} \right)$
Node number 3: $(\xi_{N3}, \zeta_{N3}) = (0,1)$ Node number 6: $(\xi_{N6}, \zeta_{N6}) = \left(0, \frac{1}{2} \right)$
                                                            Node number 7: $(\xi_{N7}, \zeta_{N7}) = \left(\frac{1}{3}, \frac{1}{3} \right)$
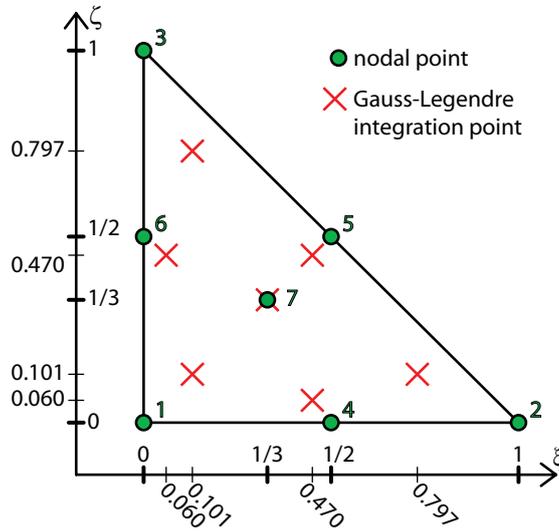

Figure C.1: Standardized local element defined on local coordinates (ξ, ζ). The triangular element consists of seven nodal points (green), which are locally numbered in the indicated order. The seven Gauss–Legendre quadrature points are used for the numerical integration.

For the seven node triangular element there are seven bi–quadratic shape functions. They are shown in Figure C.2. The sum of all shape functions is equal to 1 everywhere within the element. Each shape function is equal to 1 at its corresponding nodal point and equal to 0 at all other nodal points. Using $\chi = 1 - \xi - \zeta$ the seven shape functions are:

$$
\begin{aligned}
N_1 &= (2\chi - 1)\chi + 3\xi\zeta\chi, & \text{(C.33)} \\
N_2 &= (2\xi - 1)\xi + 3\xi\zeta\chi, & \text{(C.34)} \\
N_3 &= (2\zeta - 1)\zeta + 3\xi\zeta\chi, & \text{(C.35)} \\
N_4 &= 4\chi\xi + 12\xi\zeta\chi, & \text{(C.36)} \\
N_5 &= 4\xi\zeta + 12\xi\zeta\chi, & \text{(C.37)} \\
N_6 &= 4\zeta\chi + 12\xi\zeta\chi, & \text{(C.38)} \\
N_7 &= 27\xi\zeta\chi. & \text{(C.39)}
\end{aligned}
$$
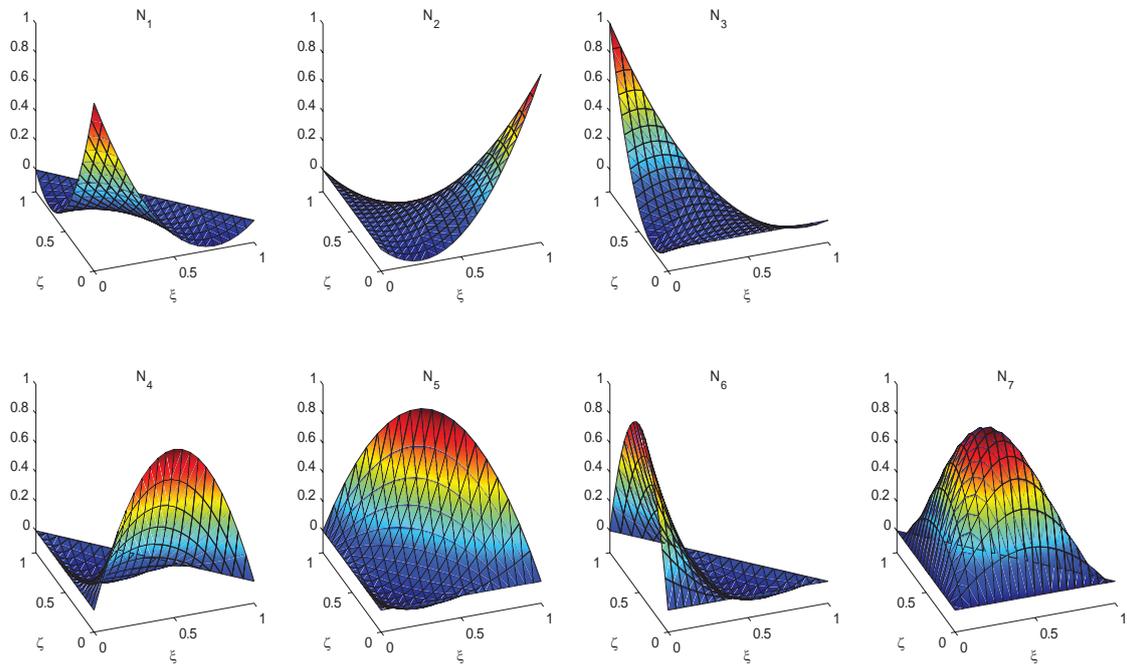
Figure C.2: The seven bi–quadratic shape functions defined for the seven node triangular element on the local coordinates (ξ, ζ).

The spatial derivatives of the shape functions with respect to the local coordinates (ξ, ζ) are:

$$\frac{\partial N_1}{\partial \xi} = -3 + 4\xi + 4\zeta + 3\zeta\chi - 3\xi\zeta, \tag{C.40}$$

$$\frac{\partial N_1}{\partial \zeta} = -3 + 4\xi + 4\zeta + 3\chi\xi - 3\xi\zeta, \tag{C.41}$$

$$\frac{\partial N_2}{\partial \xi} = -1 + 4\xi + 3\zeta\chi - 3\xi\zeta, \tag{C.42}$$

$$\frac{\partial N_2}{\partial \zeta} = 3\chi\xi - 3\xi\zeta, \tag{C.43}$$

$$\frac{\partial N_3}{\partial \xi} = 3\zeta\chi - 3\xi\zeta, \tag{C.44}$$

$$\frac{\partial N_3}{\partial \zeta} = -1 + 4\zeta + 3\chi\xi - 3\xi\zeta, \tag{C.45}$$

$$\frac{\partial N_4}{\partial \xi} = 4 - 8\xi - 4\zeta - 12\zeta\chi + 12\xi\zeta, \tag{C.46}$$

$$\frac{\partial N_4}{\partial \zeta} = -4\xi - 12\chi\xi + 12\xi\zeta, \tag{C.47}$$

$$\frac{\partial N_5}{\partial \xi} = 4\zeta - 12\zeta\chi + 12\xi\zeta, \tag{C.48}$$

$$\frac{\partial N_5}{\partial \zeta} = 4\xi - 12\chi\xi + 12\xi\zeta, \tag{C.49}$$

$$\frac{\partial N_6}{\partial \xi} = -4\zeta - 12\zeta\chi + 12\xi\zeta, \tag{C.50}$$

$$\frac{\partial N_6}{\partial \zeta} = 4 - 4\xi - 8\zeta - 12\chi\xi + 12\xi\zeta, \tag{C.51}$$

$$\frac{\partial N_7}{\partial \xi} = 27\zeta\chi - 27\xi\zeta, \tag{C.52}$$

$$\frac{\partial N_7}{\partial \zeta} = 27\chi\xi - 27\xi\zeta. \tag{C.53}$$

The local coordinates of the Gauss–Legendre quadrature points (red crosses in Figure C.1) are:

Quadrature point number 1: $(\xi_{Q1}, \zeta_{Q1}) = (0.101286507323456, 0.101286507323456)$
Quadrature point number 2: $(\xi_{Q2}, \zeta_{Q2}) = (0.797426985353087, 0.101286507323456)$
Quadrature point number 3: $(\xi_{Q3}, \zeta_{Q3}) = (0.101286507323456, 0.797426985353087)$
Quadrature point number 4: $(\xi_{Q4}, \zeta_{Q4}) = (0.470142064105115, 0.059715871789770)$
Quadrature point number 5: $(\xi_{Q5}, \zeta_{Q5}) = (0.470142064105115, 0.470142064105115)$
Quadrature point number 6: $(\xi_{Q6}, \zeta_{Q6}) = (0.059715871789770, 0.470142064105115)$
Quadrature point number 7: $(\xi_{Q7}, \zeta_{Q7}) = \left(\frac{1}{3}, \frac{1}{3}\right)$

The weighting factors defined at the seven Gauss–Legendre quadrature points are:

Quadrature point number 1: $w_1 = 0.0629695902724135$
Quadrature point number 2: $w_2 = 0.0629695902724135$
Quadrature point number 3: $w_3 = 0.0629695902724135$
Quadrature point number 4: $w_4 = 0.066197076394253$
Quadrature point number 5: $w_5 = 0.066197076394253$
Quadrature point number 6: $w_6 = 0.066197076394253$
Quadrature point number 7: $w_7 = 0.1125 = \frac{9}{80}$

The sum of all seven weighting factors is equal to $\frac{1}{2}$, which is equal to the area of the triangular finite element.

C.5. Time discretization

The time derivatives in Equation C.21 are approximated with a special finite difference approach, called Newmark–algorithm (Newmark, 1959; Hughes, 1987; Zienkiewicz and Taylor, 2000). An explicit and an implicit variation of the Newmark–algorithm is used. Both are predictor–corrector schemes. The time increment for the explicit Newmark algorithm has to fulfill the von Neumann stability criterion that is calculated from the wave velocity and the grid spacing of the numerical grid (Virieux, 1986; Higham, 1996; Saenger *et al.*, 2000). The implicit Newmark–algorithm calculates the displacement field **u** as the primary unknown.

- Predictor:

$$\ddot{\mathbf{u}}_{t_{i+1}}^{\text{prediction}} = -\frac{1}{\beta \Delta t^2}\mathbf{u}_{t_i} - \frac{1}{\beta \Delta t}\dot{\mathbf{u}}_{t_i} - \frac{1-2\beta}{2\beta}\ddot{\mathbf{u}}_{t_i}$$

$$\dot{\mathbf{u}}_{t_{i+1}}^{\text{prediction}} = -\frac{\gamma}{\beta \Delta t}\mathbf{u}_{t_i} + \left(1 - \frac{\gamma}{\beta}\right)\dot{\mathbf{u}}_{t_i} + \left(1 - \frac{\gamma}{2\beta}\right)\Delta t \ddot{\mathbf{u}}_{t_i}$$

(C.54)

- Solution:

$$\mathbf{u}_{t_{i+1}} = -\left(\frac{1}{\beta \Delta t^2}\mathbf{M}_L + \frac{\gamma}{\beta \Delta t}\mathbf{C} + \mathbf{K}\right)^{-1}\left(\mathbf{C}\dot{\mathbf{u}}_{t_{i+1}}^{\text{prediction}} + \mathbf{M}_L \ddot{\mathbf{u}}_{t_{i+1}}^{\text{prediction}}\right) \quad \text{(C.55)}$$

- Corrector:

$$\ddot{\mathbf{u}}_{t_{i+1}} = \ddot{\mathbf{u}}_{t_{i+1}}^{\text{prediction}} + \frac{1}{\beta \Delta t^2}\mathbf{u}_{t_{i+1}}$$

$$\dot{\mathbf{u}}_{t_{i+1}} = \dot{\mathbf{u}}_{t_{i+1}}^{\text{prediction}} + \frac{\gamma}{\beta \Delta t}\mathbf{u}_{t_{i+1}}$$

(C.56)

The explicit Newmark–algorithm calculates the acceleration field $\ddot{\mathbf{u}}$ as the primary unknown.

- Predictor:

$$\mathbf{u}_{t_{i+1}}^{\text{prediction}} = \mathbf{u}_{t_i} + \Delta t \dot{\mathbf{u}}_{t_i} + \frac{\Delta t^2}{2}\ddot{\mathbf{u}}_{t_i}$$

$$\dot{\mathbf{u}}_{t_{i+1}}^{\text{prediction}} = \dot{\mathbf{u}}_{t_i} + \Delta t \ddot{\mathbf{u}}_{t_i} + (1-\gamma)\Delta t \ddot{\mathbf{u}}_{t_i}$$

(C.57)

- Solution:

$$\ddot{\mathbf{u}}_{t_{i+1}} = -\left(\mathbf{M}_L + \gamma \Delta t \mathbf{C}\right)^{-1}\left(\mathbf{C}\dot{\mathbf{u}}_{t_{i+1}}^{\text{prediction}} + \mathbf{K}\mathbf{u}_{t_{i+1}}^{\text{prediction}}\right) \quad \text{(C.58)}$$

- Corrector:

$$\mathbf{u}_{t_{i+1}} = \mathbf{u}_{t_i} + \Delta t \dot{\mathbf{u}}_{t_i} + \frac{\Delta t^2}{2}\ddot{\mathbf{u}}_{t_i}$$

$$\dot{\mathbf{u}}_{t_{i+1}} = \dot{\mathbf{u}}_{t_i} + (1-\gamma)\Delta t \ddot{\mathbf{u}}_{t_i} + \gamma \Delta t \ddot{\mathbf{u}}_{t_{i+1}}$$

(C.59)

In Equations C.54 – C.59 t_i is the index of any time step and Δt is the time increment. The parameters β and γ are the two Newmark parameters. Their values are $\beta = \frac{1}{4}$ and $\gamma = \frac{1}{2}$ (Newmark, 1959; Hughes, 1987; Zienkiewicz and Taylor, 2000).

C.6. Boundary conditions

The implementation of boundary conditions in a finite element algorithm is straightforward because the natural boundary conditions are already included in the derivation of Equation C.21. In other words, not defining any boundary conditions leads to a true free surface with all stress components equal to 0. For a rigid boundary condition all degrees of freedom (displacement, velocity and acceleration) are set to 0 at the nodal points located at the boundary. For a free slip boundary condition the degrees of freedom perpendicular to the boundary are set to 0. For the degrees of freedom parallel to the boundary nothing is defined and the natural boundary conditions lead to a vanishing shear stress at the boundary.

C.7. Numerical code

The numerical finite element code for two–dimensional elastic and visco–acoustic wave propagation is written in MATLAB. It is not possible to show the entire code here. However, below, the assembly of the matrices $\mathbf{M}_L$, $\mathbf{C}$ and $\mathbf{K}$ is shown. In this piece of code the following parameters and matrices apply:

`dof_tot` :	Total number of degrees of freedom in the numerical domain
`dof_per_el` :	Number of degrees of freedom in one element
`el_tot` :	Total number of elements
`EL_N` :	Matrix storing the indices of the nodes for each element
`EL_DOF` :	Indices of the degrees of freedom for each element
`GCOORD` :	Coordinates of all nodal points in the numerical domain
`kb` :	Vector storing the bulk moduli of the different media
`mu` :	Vector storing the elastic shear moduli of the different media
`eta` :	Vector storing the shear viscosities of the different media
`Phase` :	Type of media for each element, different media are numbered
`pts_per_el` :	Number of Gauss–Legendre quadrature points in one element
`shapeder` :	Spatial derivatives of shape functions with respect to local coordinates
`shape_matrix` :	Shape functions
`rho` :	Vector storing the densities of the different media

```matlab
1   % MATRICES INITIALISATION
2   % ======================
3       MLG =   sparse(dof_tot,dof_tot);               % global lumped mass matrix
4       KG  =   sparse(dof_tot,dof_tot);               % global stiffness matrix
5       CG  =   sparse(dof_tot,dof_tot);               % global damping matrix
6       KI  =   sparse(dof_per_el*dof_per_el,el_tot);  % helping
7       KJ  =   sparse(dof_per_el*dof_per_el,el_tot);  % variables
8       KL  =   sparse(dof_per_el*dof_per_el,el_tot);  % for storing
9       CL  =   sparse(dof_per_el*dof_per_el,el_tot);  % of KG and CG
10
11  % MATRIX ASSEMBLY
12  % ===============
13  for iel = 1:el_tot % ELEMENT LOOP
14      % LOCAL MATRICES INITIALIZATION
15          num     =   EL_N(:,iel);                   % nodes           in this element
16          g       =   EL_DOF(:,iel);                 % dofs            in this element
17          coord   =   GCOORD(:,num)';                % node-coordinates in this element
18
19          Ds      =   zeros(3,3);                    % local elastic D-matrix
20          Dd      =   zeros(3,3);                    % local viscous D-matrix
21          B       =   zeros(3,dof_per_el);
22          K       =   zeros(dof_per_el,dof_per_el);  % local stiffness matrix
23          C       =   zeros(dof_per_el,dof_per_el);  % local damping matrix
24          ML      =   zeros(dof_per_el,dof_per_el);  % local lumped mass matrix
25
26      % MATRICES D
27          Ds = [kb(Phase(iel))+4/3*mu(Phase(iel)) kb(Phase(iel))-2/3*mu(Phase(iel)) 0    ;...
28              kb(Phase(iel))-2/3*mu(Phase(iel)) kb(Phase(iel))+4/3*mu(Phase(iel)) 0    ;...
29              0                                 0                               mu(Phase(iel))];
30
31          Dd  = [ 4/3*eta(Phase(iel)) -2/3*eta(Phase(iel)) 0               ;...
32                -2/3*eta(Phase(iel))  4/3*eta(Phase(iel)) 0               ;...
33                 0                    0                eta(Phase(iel)) ];
34
35      for k = 1:pts_per_el % LOOP OVER INTEGRATION POINTS
36          jac                 =   shapeder(:,:,k)*coord;
37          detjac              =   det(jac);
38          shapederg           =   inv(jac) * shapeder(:,:,k);
39
40          B(1,1:2:dof_per_el-1)   =   shapederg(1,:);
41          B(2,2:2:dof_per_el)     =   shapederg(2,:);
42          B(3,1:2:dof_per_el-1)   =   shapederg(2,:);
43          B(3,2:2:dof_per_el)     =   shapederg(1,:);
44
45          K  =   K + B' *Ds  *B                          *detjac*wts(k);
46          C  =   C + B' *Dd  *B                          *detjac*wts(k);
47          ML =   ML + (diag(sum(shape_matrix(:,:,k))'))*rho(Phase(iel))*detjac*wts(k);
48      end % END OF LOOP OVER INTEGRATION POINTS
```

```
49
50        % FILL THE LOCAL MATRICES INTO THE GLOBAL MATRICES
51            rows        =    g(1:dof_per_el)*ones(1,dof_per_el);
52            cols        =    ones(dof_per_el,1)*g(1:dof_per_el)';
53        KI(:,iel)    =    rows(:);
54        KJ(:,iel)    =    cols(:);
55        KL(:,iel)    =    K(:);
56        CL(:,iel)    =    C(:);
57
58        MLG(g,g)     =    MLG(g,g) + ML;
59  end % END OF ELEMENT LOOP
60
61  KG       =    sparse(KI(:),KJ(:),KL(:),dof_tot,dof_tot);
62  CG       =    sparse(KI(:),KJ(:),CL(:),dof_tot,dof_tot);
```

The summation necessary for the numerical integration (Equation C.22 and C.32) is done
with a loop over all integration points in the element (Lines 45 – 47). The local matrices
$\check{\mathbf{M}}_L$, $\check{\mathbf{C}}$ and $\check{\mathbf{K}}$ are added to the global matrices $\mathbf{M}_L$, $\mathbf{C}$ and $\mathbf{K}$ for each element (Lines
51 – 56, 58, 61 and 62). For matrix $\mathbf{M}_L$ this is done in an obvious way in Line 58 and in
a more sophisticated way for matrices $\mathbf{C}$ and $\mathbf{K}$. The numerical code above is written in
a general way for a viscoelastic medium including both a shear modulus μ and a shear
viscosity η. In practice, depending on the medium an element belongs to, one of the two
moduli or both are defined to be 0. Then the formulation is either purely elastic ($\eta = 0$),
acoustic ($\eta = 0$ and $\mu = 0$) or visco–acoustic ($\mu = 0$). The different lines of the numerical
code correspond to the equations described above in the following relation:

- Lines 27 – 29 correspond to Equations A.12.
- Lines 31 – 33 correspond to Equations A.13.
- Line 36 corresponds to Equations C.25.
- Line 38 corresponds to Equations C.26 and C.29.
- Lines 40 – 43 correspond to Equations C.11.
- Line 45 corresponds to Equations C.15, C.22, C.27 and C.32.
- Line 46 corresponds to Equations C.14, C.22, C.27 and C.32.
- Line 47 corresponds to Equations C.20, C.22, C.27 and C.32.

Below, the core part of the time loop of the finite element code is shown. In this code
no external force term is included. An external force can be included in a simmilar way
as the boundary conditions.

```
1   if strcmp(time_int,'explicit')
2       invA        =   inv(MLG + NM_gamma*dt*CG);
3       accel_pred  =   accel;
4   end
5
6   for it = start:nt % TIME LOOP
7       switch time_int
8           case 'implicit'
9               % predictions
10                  accel_pred          =   - 1/(NM_beta*dt^2)*displ - 1/(NM_beta*dt)*vel ...
11                                          - (1/2-NM_beta)/NM_beta*accel;
12                  vel_pred            =   - NM_gamma/(NM_beta*dt)*displ ...
13                                          + (1-NM_gamma/NM_beta)*vel ...
14                                          + (1-NM_gamma/(2*NM_beta))*dt*accel;
15              % boundary conditions
16                  displ(bcdof)        =   bcval;
17                  displ_bc(bcdof)     =   bcval;
18                  F_bc                =   KG*displ_bc;
19              % solver implicit (only free nodes are solved)
20                   displ(Free)        =   cholmod( ...
21                                          (    1/(NM_beta*dt^2)*MLG(Free,Free) ...
22                                              + NM_gamma/(NM_beta*dt)*CG(Free,Free) ...
23                                              + KG(Free,Free)) , ...
24                                              -(F_bc(Free) + CG(Free,Free)*vel_pred(Free) ...
25                                              + MLG(Free,Free)*accel_pred(Free)) );
26              % correctios
27                  accel               =   accel_pred + 1/(NM_beta*dt^2)     *displ;
28                  vel                 =   vel_pred   + NM_gamma/(NM_beta*dt)*displ;
29
30          case 'explicit'
31              % prediction
32                  displ_pred          =   displ + dt*vel + dt^2/2*accel;
33                  vel_pred            =           vel + dt    *accel + (1-NM_gamma)*dt*accel;
34              % solver
35                  accel_pred          =   -invA(CG*vel_pred + KG*displ_pred);
36              % boundary conditions
37                  accel_pred(bcdof)   =   bcval;
38              % corrections
39                  displ               =   displ + dt*vel +               dt^2/2*accel;
40                  vel                 =           vel + (1-NM_gamma)*dt    *accel ...
41                                              + NM_gamma*dt       *accel_pred;
42                  accel               =   accel_pred;
43      end
44  end % END OF TIME LOOP
```

Both the explicit and the implict Newmark algorithms are included in the code above. The variable `time_int` is defined earlier in the code and defines if the implicit or the explicit time integration method is used. For the implicit case only the degrees of freedom are solved that are not overwritten by boundary conditions (Lines `15` – `19`). These degrees of freedom are defined by the variable `Free`. In the piece of code shown above the following parameters and matrices apply:

`start` :	Index of the first time step to be calculated
`nt` :	Total number of time steps
`time_int` :	Defines if the explicit or the implicit Newmark algorithm is used
`NM_beta` :	Newmark parameter β
`NM_gamma` :	Newmark parameter γ
`displ` :	Displacement vector for the whole numerical domain
`vel` :	Velocity vector for the whole numerical domain
`accel` :	Acceleration vector for the whole numerical domain
`bcdof` :	Indices of the degrees of freedom affected by boundary conditions
`bcval` :	Boundary values
`Free` :	Indices of the degrees of freedom not affected by boundary conditions

The different lines of the numerical code correspond to the equations described above in the following relation:

- Lines `5` – `9` correspond to Equations C.54.
- Lines `15` – `20` correspond to Equation C.55.
- Lines `22` and `23` correspond to Equations C.56.
- Lines `27` and `28` correspond to Equations C.57.
- Line `30` corresponds to Equation C.58.
- Lines `34` – `37` correspond to Equations C.59.

Even though the whole numerical code can not be shown here, Figure C.3 shows a relatively detailed flow chart of the finite element code. It shows a number of details that are not further discussed here.
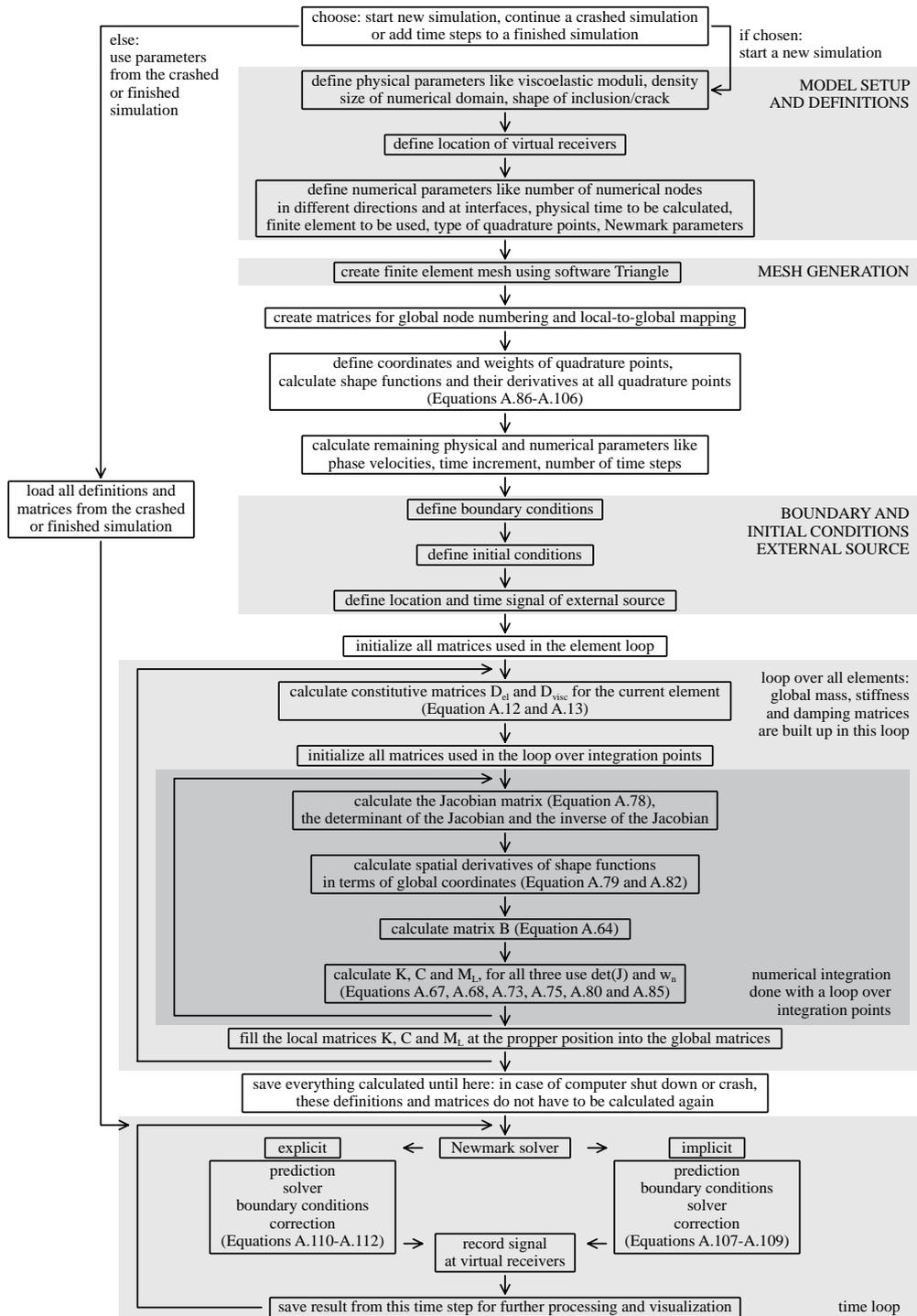
Figure C.3: Flow chart of the finite element code.

References

Bathe K.-J., 1996: **Finite element procedures**, 2nd Edition, Prentice Hall, Englewood Cliffs, ISBN 0-1330-1458-4

Cohen G. C., 2002: **Higher-order numerical methods for transient wave equations**, Series in scientific computation, Springer Verlag, Berlin, ISBN 3-5404-1598-X

Higham N. J., 1996: **Accuracy and stability of numerical algorithms**, Society for Industrial and Applied Mathematics, Philadelphia, ISBN 0-8987-1355-2

Hughes T. J. R., 1987: **The finite element method: Linear static and dynamic finite element analysis**, Dover Publications, Mineola, ISBN 0-4864-1181-8

Newmark N. M., 1959: **A method of computation for structural dynamics**, Journal of the Engeneering Mechanics Division 85, 67–94

Saenger E. H., Gold N. and Shapiro S. A., 2000: **Modeling the propagation of elastic waves using a modified finite-difference grid**, Wave Motion 31, 77–92

Virieux J., 1986: **P-Sv-wave propagation in heterogeneous media: Velocity-stress finite-difference method**, Geophysics 51, 889–901

Zienkiewicz O. C. and Taylor R. L., 2000: **The finite element method: The Basis**, Volume 1, 5th Edition, Butterworth-Heinemann, Oxford, ISBN 0-7506-5049-4

Appendix D
Resonant scattering

The focus of Chapter 2 is a comparison of the numerical accuracy of the different applied numerical methods. However, in the course of the work performed for Chapter 2 some physical observations could be made. One particularly interesting phenomena are the waves that are trapped inside the circular inclusion, also indicated in Figure 2.1. The velocity–time signal in y–direction at a receiver in the middle of the inclusion obtained from a numerical simulation is shown in Figure D.1. Figure 2.6a) shows the displacement–time signal in y–direction outside the inclusion. Because the displayed values are different in the two figures, a direct comparision is not possible. However, it is clear that the wavefield inside and outside the inclusion is very different. The internal reflections inside the inclusion lead to a continuous periodic signal compared to a signal with only a few distinct arrivals outside the inclusion (Figure 2.6a).
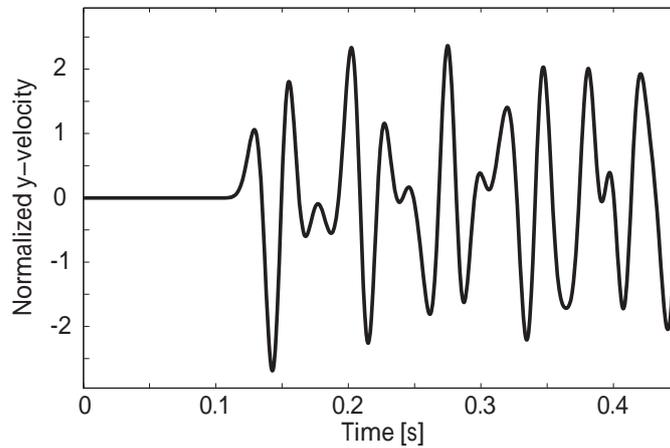

Figure D.1: Velocity–time signal in y–direction at a receiver in the middle of the inclusion. The velocity is normalized with the amplitude of the incident wave. The particular method used to generate this figure is the spatial FEM with the implicit FDM in time.

Three numerical simulations using the spatial FEM and the implicit FDM in time were performed with three different frequencies (i.e. 13.4 Hz, 26.8 Hz and 134 Hz) in the external source function. The Fourier spectra are caculated with the velocity–time signals in y–direction at the receiver in the middle of the inclusion. These spectra are shown in Figure D.2a) as thin lines. The thick lines in Figure D.2a) are the spectra of the velocity–time signals in y–direction at a receiver exaclty at the inclusion boundary where the incident wave first hits the inclusion. The signals at this receiver are used as a reference because they include neither the multiple reflections inside the inclusion nor the P– and S–waves that are radiated away from the inclusion due to the scattering process. Therefore, the spectra at this receiver are smooth and only show the dominant frequency of the external source (Figure D.2a). On the other hand, the spectra at the receiver in the middle of the inclusion show a number of peaks and troughs.
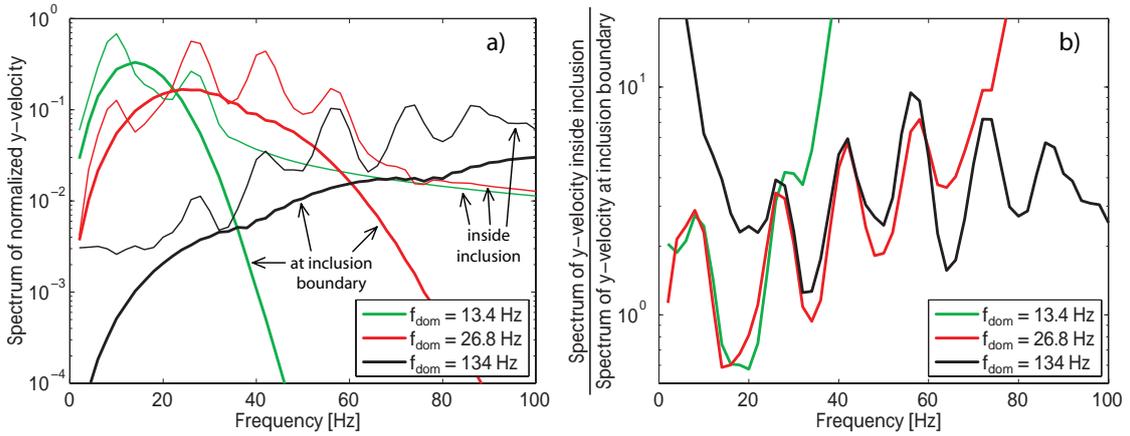

Figure D.2: a) Fourier spectra at two different receiver positions and from three different numerical simulations of a plane P–wave being scattered at a circular inclusion. Different colors represent simulations with different frequencies of the external source. Thin lines: Spectra of velocity–time signal in y–direction at a receiver inside the inclusion. Thick lines: Spectra of velocity–time signal in y–direction at a receiver exactly at the inclusion boundary where the P–wave hits the inclusion first. b) Division of the two spectra from the two receiver locations for each of the three simulations shown in a).

Figure D.2b) shows the ratio of the two spectra in Figure D.2a). The peaks and troughs of all of the resulting normalized spectra coincide in amplitude and frequency. This shows that the succession of peaks and troughs does not depend on the externally applied frequency but is a physical property of the heterogeneity, i.e. the resonance frequency. The resonant behavior of a heterogeneity when a wave is scattered is also referred to as resonant scattering (Werby and Gaunaurd, 1989, 1990; Hassan and Nagy, 1997). Every object exhibits a resonance frequency that depends on the size, the shape and the material properties of the object (Meyer *et al.*, 1958; Anderson and Hampton, 1980a,b).

References

Anderson A. L. and Hampton L. D., 1980a: **Acoustics of gas-bearing sediments, 1. Background**, Journal of the Acoustical Society of America 67, 1865–1889

Anderson A. L. and Hampton L. D., 1980b: **Acoustics of gas-bearing sediments, 2. Measurements and models**, Journal of the Acoustical Society of America 67, 1890–1903

Hassan W. and Nagy P. B., 1997: **Circumferential creeping waves around a fluid-filled cylindrical cavity in an elastic medium**, Journal of the Acoustical Society of America 101, 2496–2503

Meyer E., Brendel K. and Tamm K., 1958: **Pulsation oscillations of cavities in rubber**, Journal of the Acoustical Society of America 30, 1116–1124

Werby M. F. and Gaunaurd G. C., 1989: **Broadside resonance scattering from elastic spheroids**, IEEE Journal of Oceanic Engineering 14, 400–406

Werby M. F. and Gaunaurd G. C., 1990: **Resonance scattering from submerged elastic spheroids of high aspect ratios and its three-dimensional interpretation**, Journal of the Acoustical Society of America 88, 951–960

Acknowledgements

When I started being fascinated by numerical simulations of processes that are supposed to happen in nature, I needed someone patient enough to explain everything. At the beginning of my Ph.D time I already had a small backpack full of knowledge from my Master thesis, but I wanted a bigger one. I was very lucky to find Stefan who must be the world's best supervisor[1]. After being his first Master student I was also lucky to be his first Ph.D student, and Stefan did a wonderful job from the beginning. A very big THANK YOU[2] to you for all your teaching, explaining and helping and also for being a good friend. I am looking forward to future collaborations. I also wish to thank Jean-Pierre, my actual *Doktorvater*. Although not exactly in his field of expertise, he always fully supported my research. No matter if I had scientific or administrative questions, his office door was always open.

During lunch breaks or at the weekly Wednesday meeting[3] I could work and discuss with another six people involved in this research project. I want to thank my fellow Ph.D's Beatriz, Brian and Marc for sharing the ups and downs of a Ph.D student's life[4]. I wish all the best to Brian in his future life in the industry and to Beatriz and Marc a high degree of stamina for the final phase of their Ph.D[5]. I thank Erik and Tung for their reviews and expert comments on my work. This research project whould never have been possible without the support of Spectraseis. Working together with the industry opened many opportunities[6]. I want to say thank you to all the members and former members of Spectraseis for their support, especially the following people, who I have been collaborating with a lot: Brad[7], Reto, Rob, Martin, Ross, David, Arnaud, Reda, Mathieu, Sabrina[8], Rodolphe, Brice[9], Fernando, Patrik, Rene and Tian.

---

[1]Even though there is no proof for that, there is also no disproof
[2]MERCI VIELMOAL
[3]which was always veeeeery short
[4]and also for sharing our small packed office
[5]It's going to be tough, right Brian?
[6]such as going to Dubai and Texas or visiting major oil companies in California and Abu Dhabi
[7]Make that black steak ready when I visit you in San Francisco
[8]All the best for your Ph.D!
[9]Don't let yourself catch swimming in Abu Dhabi!

I am grateful that the two external reviewers, Holger and David, spent some time going through this thesis and made their way to Zurich for the Defense. The following people motivated me to go on with numerical modeling by introducing and explaining many details to me: Yuri, Guy[10], Taras, Boris, Dani and Thomas[11].

Sarah not only is the next generation of Stefan's Ph.D students but she also takes over many of my assistant duties at ETH. I want to thank her[12] for sharing her enthusiasm for numerical modeling, for motivating me to start working early in the morning and for letting me use her super–fast computer Forrest, whithout which I probably never would have finished this thesis in time. I whish her all the best for her time as a Ph.D student. I thank all current and former members of the Structural Geology and Tectonics Group at ETH who spent three years with me in the LEB building: Marion, Eli, Asghar[13], Negar, Rolf, Daniela[14], Bettina, Claudio, Liza, Pippo, Pierre, Claudio, Weronika, Marina, Sebastien, Luigi, Neil, Santa, Jeroen, Ingrid, Diane, Karsten, Benjamin, Mohammad, Marco[15], Jacqueline[16], Marina and Clemens. I also want to thank the following members of the Department of Earth Sciences at ETH for sharing their time with me at many Fridaybeers, coffee breaks, in bQm or in Safari Bar[17]: Maxim, Manuele, Gregor, Hein, Teodoro, Matthew[18], Pietro, Gaudenz, Andy, Marietta[19], Anja, Stefanie, Maarten, Paola, Jöggu, Andy[20], Carmen and Regula who is probably the best secretary ever.

I am very thankful to my father[21] who always gave good advice for my decisions, not only when it came to the Ph.D. Last but not least, I want to thank Yoli for tolerating a lot, especially during the final phase of the Ph.D when I had to work evenings and weekends. You supported me by loving me, and I am very thankful for that. I hope I can support you in the same way when you are about to finish your Ph.D.

---

[10]If anyone wants to learn the finite element method, go to Guy. He is a superb teacher.
[11]Thanks also for providing the template for this LaTex document
[12]grazia fitgun!
[13]Can you bring some more of these tasty dates?
[14]for the liquid intermezzos when I had to be cheered up
[15]for spending Christmas holidays in the office with me
[16]for joining me for early–morning tea breaks
[17]where we of course always had scientific discussions
[18]for convincing me to write this thesis in LaTex
[19]for not giving up inviting me until I manage to follow the invitation
[20]I think there were explosives in the WTC.
[21]Now he has to understand this in English, puh!

Curriculum Vitae of Marcel Frehner

Personal Details

Name	Marcel Frehner
Birth date	November 30$^{\text{th}}$ 1979
Birth place	St. Gallen, Switzerland
Nationality	Swiss

Education

2006 – 2009	Ph.D. at Geological Institute of ETH Zurich, Switzerland
	Committee: Prof. Dr. Jean–Pierre Burg
	PD Dr. Stefan M. Schmalholz
	Dr. ir. David M.J. Smeulders
	Prof. Dr. Holger Steeb
2000 – 2005	Studies of Earth Science at ETH Zurich, Switzerland, graduation with award
	Major subject: Structural Geology and Tectonics
	Minor subjects: Seismology, Sedimentology and Stratigraphy
	Geochemistry and Isotope Geology
	Diploma thesis: Strain distribution of buckled multilayer systems and its
	influence on the development of asymmetric parasitic folds
1995 – 1999	Swiss Matura Type C (Mathematics and Natural Science), graduation with award
	Kantonsschule am Burggraben, St. Gallen, Switzerland

Work experience

2006 – 2009	Involvement in Spectraseis AG, Zurich, Switzerland
	due to industry–related Ph.D. project
2006 – 2009	Research Assistant, Geological Institute, ETH Zurich, Switzerland

Teaching experience

2003 – 2009	Teaching Assistant, Geological Institute, ETH Zurich, Switzerland
	including courses on the finite element method, the finite difference method,
	geological mapping techniques, geological field courses, fundamentals of earth science
2004 & 2005	Leading exam preparation courses at ETH Zurich, Switzerland on
	structural geology, fundamentals of geophysics, applied linear algebra

Summary

Many seismic surveys are carried out in areas with porous or fractured rocks containing fluids, e.g. volcanic areas or hydrocarbon reservoirs. Therefore, the effects of fluids in porous or fractured rocks on the propagation of seismic waves are important to understand. In this thesis three such phenomena are investigated numerically, namely

- scattering at heterogeneities,
- Stoneley guided waves reflected and scattered at crack tips and
- oscillations on the pore–level due to surface tension effects.

The presented phenomena exhibit a multiscale character because seismic wavelengths can be orders of magnitude different from the objects that cause the phenomena, i.e. pores or cracks. Numerical modeling of such multiscale problems can be approached in different ways. On one hand, effective medium and mixture models can be used that approximate the small scale processes with effective material parameters and incorporate them into larger scale wave propagation models. On the other hand, direct numerical simulations can be used that fully resolve the small scale processes. Both approaches are followed in this thesis.

- Scattering of a plane P–wave at a circular object of a similar size as the P–wave's wavelength is modeled in two dimensions with different numerical techniques. The circular object is numerically fully resolved and the results are compared with an analytical solution. The goal is to compare numerical accuracies of the different methods for later use in direct numerical simulations. It is found that the finite element method is most suitable for spatial discretization of such problems due to the unstructured numerical mesh.

- The reflection of Stoneley guided waves at the tip of a crack is investigated with direct numerical simulations in two dimensions using the finite element method. The reflection coefficient lies between 43 % and almost 100 % and depends on the fluid filling the crack and on the crack geometry. The part of the Stoneley guided wave that is not reflected is scattered at the crack tip and P– and S–waves are emitted into the surrounding rock. The radiation pattern of these elastic body waves is described in detail for different model setups.

- Microscale oscillations within a rock can arise from non–wetting fluid blobs in partially saturated pores and cracks. When such fluid blobs are out of equilibrium, surface tension forces act as the restoring forces for the oscillations. Other explanations for internal oscillations in a rock can be given, e.g. Stoneley guided waves propagating back and forth along a finite crack. Such microscale oscillations are approximated and coupled to the macroscale wave equation. The resulting equations are solved in one dimension with the finite difference method. Results show that internal oscillations introduce a strong velocity dispersion around the resonance frequency and temporarily modify the frequency content of a propagating wave. Energy is transferred between the internal oscillations and the wave.

This thesis covers a few aspects of fluid–rock interaction relevant for seismic wave propagation. For this, no existing models, such as the Biot model, are applied but direct numerical simulations and a newly developed continuum model are used. The thesis ends by discussing the applicability of the results to natural situations. Tremor–signals are observed for example around volcanic conduits or above hydrocarbon reservoirs. The narrow frequency band of these signals may be explained, among other explanations, by oscillatory effects in the subsurface due to Stoneley guided waves that fall into resonance or due to surface tension–induced resonances of non–wetting fluids.